Microstructure and Properties of Simulated Weld Metals

Final Report 278-T-04

for Project

Development of Optimized Welding Solutions for X100 Line Pipe Steel

Prepared for the
Design, Materials, and Construction Technical Committee of
Pipeline Research Council International, Inc.
Project MATH-1 Catalog No. L5XXXX

and

U.S. Department of Transportation
Pipeline and Hazardous Materials Safety Administration
Office of Pipeline Safety
Agreement Number DTPH56-07-T-000005

Prepared by

J.A. Gianetto, G.R Goodall and W.R Tyson,
CANMET Materials Technology Laboratory

M.A. Quintana and V.B Rajan
The Lincoln Electric Company

Y. Chen
Center for Reliable Energy Systems

September 2011

This research was funded in part under the Department of Transportation, Pipeline and Hazardous Materials Safety Administration's Pipeline Safety Research and Development Program. The views and conclusions contained in this document are those of the authors and should not be interpreted as representing the official policies, either expressed or implied, of the Pipeline and Hazardous Materials Safety Administration, or the U.S. Government.

CANMET Materials Technology Laboratory

Microstructure and Properties of Simulated Weld Metals

J.A. Gianetto, G.R Goodall, and W.R Tyson,

CANMET Materials Technology Laboratory
Minerals and Metals Sector, Natural Resources Canada
183 Longwood Road South, Hamilton, ON, Canada, L8P 0A5

M.A Quintana and V.B Rajan
Lincoln Electric Company

Y. Chen
Center for Reliable Energy Systems

CANMET Report No. 2011-05(TR)

September 2011

DISCLAIMER

Natural Resources Canada makes no representations or warranties respecting the contents of this report, either expressed or implied, arising by law or otherwise, including but not limited to implied warranties or conditions of merchantability or fitness for a particular purpose.

Catalog No. L5XXXX

Microstructure and Properties of Simulated Weld Metals

Final Report 278-T-04

for Project

Development of Optimized Welding Solutions for X100 Line Pipe Steel

Prepared for the
Design, Materials, and Construction Technical Committee of
Pipeline Research Council International, Inc.
Project MATH-1 Catalog No. L5XXXX

and

U.S. Department of Transportation
Pipeline and Hazardous Materials Safety Administration
Office of Pipeline Safety
Agreement Number DTPH56-07-T-000005

Prepared by

J.A. Gianetto, G.R Goodall and W.R Tyson,
CANMET Materials Technology Laboratory

M.A. Quintana and V.B Rajan
The Lincoln Electric Company

Y. Chen
Center for Reliable Energy Systems

September 2011

Version	Date of Last Revision	Date of Uploading	Comments
2	2 April 2001	4 April 2001	References to be inserted after review.

This report is furnished to Pipeline Research Council International, Inc. (PRCI) under the terms of PRCI contract [278-PR- 348 - 074513], between PRCI and the MATH-1 contractors:

- Electricore (prime contractor),
- Center for Reliable Energy Systems, CANMET, NIST, and The Lincoln Electric Company (sub-contractors).

The contents of this report are published as received from the MATH-1 contractor and subcontractors. The opinions, findings, and conclusions expressed in the report are those of the authors and not necessarily those of PRCI, its member companies, or their representatives. Publication and dissemination of this report by PRCI should not be considered an endorsement by PRCI of the MATH-1 contractor and subcontractors, or the accuracy or validity of any opinions, findings, or conclusions expressed herein.
In publishing this report, PRCI and the MATH-1 contractors make no warranty or representation, expressed or implied, with respect to the accuracy, completeness, usefulness, or fitness for purpose of the information contained herein, or that the use of any information, method, process, or apparatus disclosed in this report may not infringe on privately owned rights. PRCI and the MATH-1 contractors assume no liability with respect to the use of, or for damages resulting from the use of, any information, method, process, or apparatus disclosed in this report. By accepting the report and utilizing it, you agree to waive any and all claims you may have, resulting from your voluntary use of the report, against PRCI and the MATH-1 contractors.

Pipeline Research Council International Catalog No. L5XXXX

PRCI Reports are Published by Technical Toolboxes, Inc.

3801 Kirby Drive, Suite 520
Houston, Texas 77098
Tel: 713-630-0505
Fax: 713-630-0560
Email: info@ttoolboxes.com

PROJECT PARTICIPANTS

PROJECT TEAM MEMBER	COMPANY AFFILIATION	PROJECT TEAM MEMBER	COMPANY AFFILIATION
Arti Bhatia	Alliance	Jim Costain	GE
Jennifer Klementis	Alliance	Gilmar Batista	Petrobras
Roger Haycraft	Boardwalk	Marcy Saturno de Menezez	Petrobras
David Horsley	BP	Dave Aguiar	PG&E
Mark Hudson	BP	Ken Lorang	PRCI
Ron Shockley	Chevron	Maslat Al-Waranbi	Saudi Aramco
Sam Mishael	Chevron	Paul Lee	SoCalGas
David Wilson	ConocoPhillips	Alan Lambeth	Spectra
Satish Kulkarni	El Paso	Robert Turner	Stupp
Art Meyer	Enbridge	Gilles Richard	TAMSA
Bill Forbes	Enbridge	Noe Mota Solis	TAMSA
Scott Ironside	Enbridge	Philippe Darcis	TAMSA
Sean Keane	Enbridge	Dave Taylor	TransCanada
Laurie Collins	Evraz	Joe Zhou	TransCanada
David de Miranda	Gassco	Jason Skow	TransGas
Adriaan den Herder	Gasunie	Ernesto Cisneros	Tuberia Laguna
Jeff Stetson	GE	Vivek Kashyap	Welpsun
		Chris Brown	Williams

CORE RESEARCH TEAM	
RESEARCHER	**COMPANY AFFILIATION**
Yaoshan Chen	Center for Reliable Energy Systems
Yong-Yi Wang	Center for Reliable Energy Systems
Ming Liu	Center for Reliable Energy Systems
Dave Fink	Lincoln Electric Company
Marie Quintana	Lincoln Electric Company
Vaidyanath Rajan	Lincoln Electric Company
Joe Daniel	Lincoln Electric Company
Radhika Panday	Lincoln Electric Company
James Gianetto	CANMET Materials Technology Laboratory
John Bowker	CANMET Materials Technology Laboratory
Bill Tyson	CANMET Materials Technology Laboratory
Guowu Shen	CANMET Materials Technology Laboratory
Dong Park	CANMET Materials Technology Laboratory
Timothy Weeks	National Institute of Standards and Technology
Mark Richards	National Institute of Standards and Technology
Dave McColskey	National Institute of Standards and Technology
Enrico Lucon	National Institute of Standards and Technology
John Hammond	Consultant Metallurgist & Welding Engineer

This Page Intentionally Left Blank

FINAL REPORT STRUCTURE

Focus Area 1 - Update of Weld Design, Testing, and Assessment Procedures for High Strength Pipelines		
Report #	**Description**	**Lead Authors**
277-T-01	Background of Linepipe Specifications	CRES/CANMET
277-T-02	Background of All-Weld Metal Tensile Test Protocol	CANMET/Lincoln
277-T-03	Development of Procedure for Low-Constraint Toughness Testing Using a Single-Specimen Technique	CANMET/CRES
277-T-04	Summary of Publications: Single-Edge Notched Tension SE(T) Tests	CANMET
277-T-05	Small Scale Tensile, Charpy V-Notch, and Fracture Toughness Tests	CANMET/NIST
277-T-06	Small Scale Low Constraint Fracture Toughness Test Results	CANMET/NIST
277-T-07	Small Scale Low Constraint Fracture Toughness Test Discussion and Analysis	CANMET/NIST
277-T-08	Summary of Mechanical Properties	CANMET
277-T-09	Curved Wide Plate Tests	NIST/CRES
277-T-10	Weld Strength Mismatch Requirements	CRES/CANMET
277-T-11	Curved Wide Plate Test Results and Transferability of Test Specimens	CRES/CANMET
277-S-01	Summary Report 277 Weld Design, Testing, and Assessment Procedures for High Strength Pipelines	CRES

Focus Area 2 - Development of Optimized Welding Solutions for X100 Linepipe Steel		
Report #	**Description**	**Lead Authors**
278-T-01	State of The Art Review	Lincoln
278-T-02	Material Selection, Welding and Weld Monitoring	Lincoln/CANMET
278-T-03	Microstructure and Hardness Characterization of Girth Welds	CANMET/Lincoln
278-T-04	Microstructure and Properties of Simulated Weld Metals	CANMET/Lincoln
278-T-05	Microstructure and Properties of Simulated Heat Affected Zones	CANMET/Lincoln
278-T-06	Essential Welding Variables	Lincoln/CANMET
278-T-07	Thermal Model for Welding Simulations	CRES/CANMET
278-T-08	Microstructure Model for Welding Simulations	CRES/CANMET
278-T-09	Application to Other Processes	Lincoln/CANMET
278-S-01	Summary Report 278 Development of Optimized Welding Solutions for X100 Line Pipe Steel	Lincoln

EXECUTIVE SUMMARY

This investigation is part of a major consolidated program of research that was launched to address key research gaps related to welding of high strength pipe which is an integral part of pipeline design and construction. The two research focus areas include (i) update of weld design, testing, and assessment procedures and (ii) development of optimized welding solutions for high strength steel X100 line pipe. In the second focus area, physical simulation techniques were used to study both weld metal (WM) and heat affected zone (HAZ) regions for a range of compositions and thermal cycles relevant to various welding options being considered for high strength steel (X80 and X100) pipes. The results of the WM and HAZ studies are reported separately. These complementary investigations were intended to provide improved understanding and information necessary to establish guidelines for development of welding procedures for demanding applications.

A major challenge is to ensure that weld strength exceeds that of the parent pipe (overmatching), which is a requirement for strain based design as strain localization in the weld can otherwise occur. Achieving the required level of weld metal overmatching, together with adequate ductility and good low temperature toughness, becomes a challenge as the strength of the pipe increases. This challenge becomes greater with the use of advanced high-productivity pulsed gas metal arc welding (GMAW-P) process variants (single versus tandem and dual torch) where there may be more complex thermal cycles and variation in cooling rates. The cooling rate (or cooling time) is one of the most important parameters influencing microstructural evolution in either WM or HAZ regions. In this investigation a range of WM compositions based on C-Mn-Si-Mo, C-Mn-Si-Ni-Mo-Ti and C-Mn-Si-Ni-Cr-Mo-Ti was selected for more detailed evaluation using both actual experimental plate welds and specimens simulated by Gleeble thermal cycling. For simulated welds, the influence of weld thermal cycles on continuous cooling transformation (CCT) behaviours of five experimental WM compositions was studied using dilatometry, optical microscopy, detailed microhardness testing, and selected Charpy-V-notch (CVN) impact toughness testing. The main objectives were:

- To characterize the WM microstructure and hardness for a series of experimental plate welds produced with two distinct welding procedures using single and multipass welding techniques,
- To apply thermal simulation techniques to develop WM CCT diagrams for a range of compositions applicable to welding of X100 pipe to serve as a tool for predicting their respective transformation behaviours, and
- To provide an assessment and comparison of notch toughness properties for a range of single thermal cycles.

The five specially-designed experimental plate welds were made using two distinctly different GMAW-P procedures with wire electrodes applicable for joining X100 pipe. The weld procedures consisted of three initial fill passes deposited at 0.5 kJ/mm and a final deep-fill pass at 1.5 kJ/mm to just fill the narrow-gap joint. An important part of the research focused on development of WM CCT diagrams using radial dilatometry and post-test metallography to establish the influence of composition and thermal cycle (cooling time) on formation of fine-scale, predominantly displacive M, B and AF transformations. The evaluation of the

experimental plate welds in conjunction with the thermal simulation results allowed the following conclusions to drawn.

1) The specially-designed experimental plate welds produced with carbon equivalent (CEN) values ranging from 0.31 to 0.44 allowed both real and thermal simulated WM regions to be characterized in terms of microstructure, hardness and notch toughness.

2) For the series of experimental plate welds the microstructure and hardness were found to follow a consistent trend with the 1.5 kJ/mm deep-fill pass exhibiting a generally coarser and overall softer microstructure than in the underlying 0.5 kJ/mm multipass weld region. The microstructures ranged from acicular ferrite (AF) dominated to bainitic/martensitic with increasing alloy and increasing cooling rates (shorter cooling times) of the 0.5 kJ/mm multipass welds.

3) The microstructure and microhardness correlated reasonably well with CEN for the 1.5 kJ/mm deep-fill pass and the 0.5 kJ/mm multipass weld. In the latter case, the observed alternating pattern of hardness corresponded well with the distribution of as deposited AD (high values) and reheated WM (low values).

4) RH WM microstructure generated by deposition of the 1.5 kJ/mm deep-fill pass over the underlying 0.5 kJ/mm weld pass was generally observed to resemble the microstructure formed within the columnar as-deposited regions of the 1.5 kJ/mm deep-fill pass, although the grains tended to be more equiaxed in the reheated region.

5) Dilatometric experiments on single pass weld metal specimens provided very useful information on the transformation behaviour of high strength WM, including the transformation temperatures and in some cases the relative proportions of respective phases to be quantified. The results, presented in the form of WM CCT diagrams, clearly show the microstructural evolution as a function of hardenability and cooling time. Over the range of cooling times investigated, the lowest-alloyed WM (LA90) exhibited microstructures dominated by bainite/martensite to AF, whereas the highest-alloyed WM (PT02) formed large fractions of martensite/bainite to AF.

6) For a given weld metal composition, there was a marked decrease in microhardness of the thermally simulated WM microstructures resulting from the relatively small range of cooling times $\Delta t_{800\text{-}500}$ = 2 to 10 s followed by a more gradual decline for further increases in cooling time.

7) For sub-size Charpy-V-notch (CVN) specimens there was a decrease in impact energy for the simulated WM using Tp=1300˚C with $\Delta t_{800\text{-}500}$ = 5 s compared with the 1.5 kJ/mm AW condition and a trend towards decreasing notch toughness with increasing WM hardenability.

8) For surface-notched full-size CVN simulated specimens (Tp=1300°C and cooling times $\Delta t_{800\text{-}500}$ = 5, 10 and 20 s) there was a similar decrease in toughness for the shortest cooling time ($\Delta t_{800\text{-}500}$ = 5 s) followed by an increase in toughness for longer cooling times.

TABLE OF CONTENTS

Executive Summary viii
Table of Contents x
List of Figures xi
List of Tables xii
1 Introduction 1
2 Objectives 2
3 Experimental Procedure 2
3.1 Preparation of Experimental Welds 2
3.2 Weld Metal Chemical Analysis 3
3.3 Preparation of Test Specimens 4
3.4 Weld Thermal Cycles 4
3.5 Thermal simulation Experiments 4
3.6 Metallography and Microhardness Testing 5
3.7 Toughness Testing 6
4 Results 6
4.1 Chemical Composition 6
4.2 Microstructure and Microhardness 6
4.3 Thermal Simulation 8
4.3.1 Dilatometric Analysis 8
4.3.2 WM CCT Diagrams, Microstructure and Microhardness 9
4.3.3 WM Charpy Toughness 11
5 Discussion 12
5.1 Hardness of Experimental Plate Welds Versus Simulated WM 12
5.2 CCT Diagrams and Microstructure 13
5.3 WM Toughness 14
6 Summary and Conclusions 15
7 Acknowledgments 16
8 References 16

LIST OF FIGURES

Figure 1. Schematic diagrams and macrograph for experimental welds. 24
Figure 2. Shematic diagram showing location of WM dilatometric 6 x 6 mm and full-sized 10 x 10 mm specimen blanks (top) along with detail of rounded dilatometric specimen used for CCT experiments (bottom). 25
Figure 3. Representative macrograph of a WM dilatometric specimen cut longitudinally (parallel to the specimen length along the mid-plane) to reveal the through-thickness weld metal after thermal cycling. 25
Figure 4. Location and orientation of specimens used for sub-sized and full-sized WM Charpy impact toughness testing. 26
Figure 5. Thermal cycles (temperature versus time) for CCT simulation experiments with cooling times, $\Delta t_{800\text{-}500}$ = ~2, 3.5, 5, 7.5, 10, 20 and 50 s. 27
Figure 6. Macrograph of experimental weld showing areas (rectangular boxes) used for characterization of as-deposited and reheated WM microstructures. 28
Figure 7. Micrographs of as-deposited weld metal of experimental weld LA90. 29
Figure 8. Micrographs of reheated WM of experimental weld LA90. 30
Figure 9. Microhardness results for LA90 weld. 31
Figure 10. Micrographs of as-deposited weld metal of experimental weld LA100. 32
Figure 11. Micrographs of reheated WM of experimental weld LA100. 33
Figure 12. Microhardness results for weld LA100. 34
Figure 13. Micrographs of as-deposited weld metal of experimental weld, NiMo80. 35
Figure 14. Micrographs of reheated WM of experimental weld NiMo80. 36
Figure 15. Microhardness results for weld NiMo80. 37
Figure 16. Micrographs of as-deposited weld metal of experimental weld PT-01. 38
Figure 17. Micrographs of reheated WM of experimental weld PT-01. 39
Figure 18. Microhardness results for weld PT-01. 40
Figure 19. Micrographs of as-deposited weld metal of experimental weld PT-02. 41
Figure 20. Micrographs of reheated WM of experimental weld PT-02. 42
Figure 21. Microhardness surveys of experimental weld PT-02. 43
Figure 22. Dialation curves for LA90 WM as a function of cooling times Δt800-500 = 2, 3.5, 5, 7.5, 10, 20 and 50 s. 44
Figure 23. Dilatation curves for LA100 WM as a function of cooling times $\Delta t_{800\text{-}500}$ = 2, 3.5, 5, 7.5, 10, 20 and 50 s. 45
Figure 24. Dilatation curves for NiMo80 WM as a function of cooling times $\Delta t_{800\text{-}500}$ = 2, 3.5, 5, 7.5, 10, 20 and 50 s. 46
Figure 25. Dilatation curves for PT-01 WM as a function of cooling times $\Delta t_{800\text{-}500}$ = 2, 3.5, 5, 7.5, 10, 20 and 50 s. 47
Figure 26. Dilatation curves for PT-02 WM as a function of cooling times $\Delta t_{800\text{-}500}$ = 2, 3.5, 5, 7.5, 10, 20 and 50 s. 48
Figure 27. CCT diagram for weld LA 90. 49
Figure 28. WM microstructures of thermally cycled specimens from weld LA 90 as a function of cooling time. 50
Figure 29. CCT diagram for weld LA 100. 51
Figure 30. WM microstructures of thermally cycled specimens from weld LA 100 as a function of cooling time. 52

Figure 31. CCT diagram for weld NiMo80. 53
Figure 32. WM microstructures of thermally cycled specimens from weld NiMo80 as a function of cooling time. 54
Figure 33. CCT diagram for weld PT-01. 55
Figure 34. WM microstructures of thermally cycled specimens from weld PT-01 as a function of cooling time. 56
Figure 35. CCT diagram for weld PT-02. 57
Figure 36. WM microstructures of thermally cycled specimens from weld PT-02, as a function of cooling time. 58
Figure 37. Microhardness of thermally cycled WM specimens as a function of cooling time. ... 59
Figure 38. Correlation between microhardness and carbon equivalent formula (CE_{IIW} and CEN) for WM regions within 1.5 kJ/mm deep-fill pass and underlying 0.5 kJ/mm fill passes. 60
Figure 39. Correlation between microhardness and carbon equivalent for WM regions within 1.5 kJ/mm deep-fill pass and underlying 0.5 kJ/mm fill passes. 61
Figure 40. Correlations between microhardness and carbon equivalent for experimental welds and range of thermally simulated WM with selected cooling times. 62
Figure 41. SEM images of thermally cycled LA100 WM for cooling times $\Delta t_{800\text{-}500}$= 5, 10 and 20s. 63
Figure 42. SEM images of thermally cycled NiMo80 for cooling times $\Delta t_{800\text{-}500}$= 5, 10 and 20s. 64
Figure 43. SEM images of thermally cycled PT- 01 for cooling times $\Delta t_{800\text{-}500}$= 5, 10 and 20s. 65

LIST OF TABLES

Table 1. Experimental weld metal and X100 pipe compositions 20
Table 2. Microhardness results for experimental welds deposited at energy inputs of 1.5 and 0.5 kJ/mm. 21
Table 3. Microhardness results for WM CCT samples.....21
Table 4. Sub-size Charpy impact toughness of 1.5 kJ/mm deep-fill pass and thermally cycled WM samples with through-thickness notch orientation. 22
Table 5. Full-size Charpy impact toughness of 1.5 kJ/mm deep-fill pass and thermally cycled WM samples with surface notch orientation from hot pass region. 23

1 INTRODUCTION

This investigation is part of a major consolidated program of research that was launched to address key research gaps related to welding of high strength pipe which is an integral part of pipeline design and construction. The two research focus areas included (i) update of weld design, testing, and assessment procedures and (ii) development of optimized welding solutions for high strength steel X100 line pipe [1, 2]. Further information on the topics covered in the consolidated program is available in several conference papers [3-8] and the series of reports prepared for this program [9-18].

Early in this investigation emphasis was placed on production and evaluation of baseline pipe welds [5, 9, 10] that were used for test protocol development and detailed characterization of microstructure and mechanical properties. Investigation of the key factors affecting strength and toughness of weld metal (WM) and heat affected zone (HAZ) regions for a range of pipeline girth welding process options was considered important to further the work on essential welding variables. Specification and control of arc welding variables to ensure both X100 WM and HAZ regions exhibit the necessary levels of strength, ductility, and toughness was a primary goal. Two parallel research activities were initiated with a focus on application of thermal simulation to study WM and HAZ microstructure and toughness properties. This was also considered to be beneficial and useful for further refinement and calibration of thermal-microstructure models [16, 17].

A major challenge was to produce welds with strengths that exceed that of the parent pipe (overmatching), which is a requirement for strain based design as strain localization in the weld can otherwise occur. Achieving the required level of weld metal overmatching, together with adequate ductility and good low temperature toughness, becomes a challenge as the strength of the pipe increases. This challenge becomes greater with the use of advanced high-productivity pulsed gas metal arc welding (GMAW-P) process variants (single versus tandem or dual torch) where there may be more complex thermal cycles and a wide range of cooling rates. The cooling rate (or cooling time) is one of the most important parameters influencing microstructural evolution in either WM or HAZ regions. Thermal simulation is well established for assessing the influence of weld thermal cycles on microstructure and properties of HAZ regions formed in a wide variety of steels used for many industrial applications, including pipelines [19-22]. Characterization of WM microstructure and properties using thermal simulation techniques is less common, although some very useful research results have been obtained in the past by many researchers [23-30]. Gleeble®[1] thermal simulation techniques were used in this work to study the influence of weld thermal cycles on continuous cooling transformation (CCT) behaviours of five experimental WM compositions using dilatometry, optical microscopy, detailed microhardness testing, and selected Charpy-V-notch (CVN) impact toughness testing. Results and analysis of simulated HAZ regions formed in high strength pipe steels is reported separately [11]. These complementary investigations are also intended to provide improved understanding and critical information necessary to establish guidelines for development of welding procedures for demanding applications.

[1] Gleeble® is a registered trademark of Dynamic Systems Inc. Corporation New York P.O. Box 123, Route 355 Poestenkill New York 12140

2 OBJECTIVES

The objectives of this work were:

1. to characterize the WM microstructure and hardness for a series of experimental plate welds produced with two distinct welding procedures using single and multipass welding techniques,
2. to apply thermal simulation techniques to develop WM CCT diagrams for a range of compositions applicable to welding of X100 pipe to serve as a tool for predicting their respective transformation behaviors, and
3. to provide an assessment and comparison of notch toughness properties for a range of single thermal cycle conditions.

3 EXPERIMENTAL PROCEDURE

Considerable research has been carried out on development and evaluation of welding procedures for production of mechanized girth welds in high strength steel pipes over the last decade or so [31-38]. During this time several researchers have focussed their work on assessment of commercially-available welding consumables for a range of pipeline welding process variants: single, tandem, or dual torch. Other studies have included systematic evaluation or optimization of welding consumable compositions [29, 30, 31, 37, 38], with the aim of achieving high weld metal strength in combination with adequate ductility and toughness. In many of these investigations, the assessment of WM in full-scale welds was difficult as well as time-consuming and expensive. As a result it was decided, early in this investigation, to supplement the evaluation of baseline pipe welds with a systematic assessment of selected weld metal compositions using thermal simulation techniques. This would allow a wider range of thermal cycles and compositions to be investigated via CCT experiments as well as provide a comparison between the experimental plate welds and simulated WMs. The following sections describe the approach used to prepare the experimental plate welds, conduct Gleeble simulation experiments, and characterize the microstructure, hardness, and notch toughness.

3.1 Preparation of Experimental Welds

The first task in designing the experimental matrix of welds focused on the selection of appropriate weld metal composition variants based on C-Mn-Si-Mo, C-Mn-Si-Ni-Mo-Ti, and C-Mn-Si-Ni-Cr-Mo-Ti alloy systems. Based on expertise of the project team and information available in the open literature, a range of compositions was selected to essentially bracket a commercially-available electrode wire chemistry that is currently being used in pipeline construction projects. Two other commercially-available electrode wires and two recent prototype more highly-alloyed wires that were made available for this work, were used for production of the five experimental welds in this program. The first wire principally contained Mo, which would produce a comparatively lower-strength weld deposit. The second wire had much higher Ni along with Mo, while the two prototype wires contained two levels of Ni with Cr and Mo in an attempt to ensure that high weld metal strengths using both single- and dual-torch process variants could be achieved. Ti levels were also expected to differ in the final weld deposits.

The series of five experimental welds were produced in flattened sections of X100 pipe remaining from the production of the first round of single-torch welds made for this research program. The plates were machined with a compound joint design preparation from the top surface without the root pass bevel (150 x 19.1 x 483 mm [6 x 0.75 x 19 in]), as shown in Figure 1(a). Note that this joint geometry is typical of that used in narrow-gap pipe welds. Each weld was prepared using a Fanuc RJ3 robot equipped with a Lincoln PowerWave 455M programmable power source that provided pulsed-waveform-controlled gas-metal arc welding (GMAW-P). The five electrode wires were each used in combination with an 85% Ar +15% CO_2 (C15) shielding gas to produce weld deposits suitable for detailed analysis and Gleeble simulation experiments. The welds were produced using a pass sequence that consisted of a hot pass at an energy input of 0.2 kJ/mm, followed by three standard fill passes, each at an energy input of 0.5 kJ/mm, to fill the first 50% of the joint. The final deep-fill pass was deposited at an energy input of 1.5 kJ/mm (Figure 1(b)). Each plate assembly was intentionally allowed to cool to ambient temperature (not preheated) prior to deposition of the final deep-fill pass in order to partially compensate for the higher energy input used by increasing the cooling rate as much as possible so that the starting microstructure would be uniform and not overly coarse. Initial welding trials were carried out to establish the welding parameters required to obtain a deep-fill pass depth of ~7 mm (Figure 1(c)). This depth was considered sufficient to extract the necessary Gleeble specimens for subsequent thermal simulation experiments.

3.2 Weld Metal Chemical Analysis

Sections from the five experimental welds were cut and surface-ground from the top of the deep-fill pass surface to accurately determine the weld metal chemical composition using a BAIRD One Spark Spectrometer. Additional samples were cut from each deep-fill weld pass using electrical discharge machining (EDM) to determine the O and N contents of the weld metals using a LECO TC600 analyzer. The carbon equivalents of the experimental weld metals were determined using the following formulae where the elements expressed are in weight percent:

$$CE_{IIW} = C + Mn/6 + (Cr+Mo+V)/5 + (Ni + Cu)/15 \quad (1)$$

$$P_{cm} = C + Si/30 + (Mn+Cu+Cr)/20 + Ni/60 + Mo/15 + V/10 + 5B \quad (2)$$

$$CEN=C+A(C)\ (Si/24+Mn/6+Cu/15+Ni/20+(Cr+Mo+Nb+V)/5+5B) \quad (3)$$

where $A(C)= 0.75 +0.25\tanh\{20\ (C-0.12)\}$

Transformation-start temperatures from formulae developed by Steven and Hayes [39] were also calculated and used to help with interpretation of radial dilatation data generated during thermal simulation experiments:

$$B_s = 830-270(C)-90(Mn)-37(Ni)-70(Cr)-83(Mo),\ ^\circ C \quad (4)$$

$$M_s= 561-474(C)-33(Mn)-17(Ni)-17(Cr)-21(Mo),\ ^\circ C \quad (5)$$

3.3 Preparation of Test Specimens

A large number of specimens were accurately cut from the experimental welds using numerically-controlled-wire EDM. For Gleeble thermal simulation, specimens were machined for both radial dilatometry and toughness testing. Transverse specimens were cut so as to ensure that the weld metal was centered along the length of each specimen. For CCT experiments employing radial dilatometry, specimens of square cross-section (6 x 6 x 75 mm) were machined to test the 1.5 kJ/mm deep-fill pass. The central weld metal region was etched and subsequently machined to a cylindrical profile with a 5 mm diameter over a 5 mm length.
Figure 2 provides a schematic diagram with the dimensions of the specimens, while Figure 3 shows a representative macrograph that reveals the centrally located weld metal after thermal cycling.

For toughness testing, full-size Gleeble blanks (10 x 10 x 75 mm) were also machined from the welds such that the specimens contained a large proportion of the deep-fill pass as well as some of the underlying fill passes. After thermal cycling, specimens were further machined to dimensions conforming to 2/3 sub-size Charpy bars (6.66 x 10 x 55 mm). In some selected cases full-sized (10 x 10 x 55 mm) Charpy specimens were also tested (Figure 4). All specimens were etched with Nital to reveal the WM centerline prior to notching. For sub-size specimens, a through-thickness notch orientation was used, whereas for the full-size specimens, a surface notch from the hot pass side was chosen as illustrated in Figure 4.

3.4 Weld Thermal Cycles

CANMET-MTL's Gleeble 3800 was used to establish the CCT behaviours of the experimental welds and for thermally cycling the WM specimens used for subsequent Charpy impact toughness testing. Six thermal cycle (temperature-time) programs were created with the Gleeble software package supplied for weld/HAZ simulation. A Rykalin 3D cooling profile was found to more closely match the measured thermal cycles that were obtained during the full-scale welding trails conducted for this program [9]. The software package allowed input parameters for the heating rate of 250°C/s, peak temperature (Tp) 1300°C, hold time of 1 s and a range of cooling times $\Delta t_{800\text{-}500}$ = 3.5, 5, 7.5, 10, 20 and 50 s to be used in conjunction with a preheat temperature of 100°C and the pipe (plate) thickness (19.1 mm (0.750 in)) to create a set of thermal cycle programs (Figure 5). The majority of cooling times were chosen to closely match the range of cooling times (high cooling rates) associated with narrow-gap GMAW-P pipe welding as well as other process options that are known to employ higher energy inputs (with longer cooling times) To achieve very short cooling times and establish the martensite start (M_s) temperature more accurately, a thermal cycle program was created with the same heating rate, peak temperature and hold time but employing a free cool to room temperature. This resulted in consistent and repeatable cooling times of $\Delta t_{800\text{-}500} \leq 2$ s that varied according to the actual specimen cross-sectional area (diameter) and chemistry.

3.5 Thermal simulation Experiments

To establish the dilatometric data required to construct a series of WM continuous cooling transformation (CCT) diagrams, specimens from each weld were prepared for thermal cycling

following the programs developed above. Both leads of a Type-K thermocouple were spot welded to the centre of the cylindrical WM region of individual specimens which were then secured in copper grips. Care was taken to ensure that the WM region was centered within the 15 mm grip spacing. The quartz rods of a linear variable differential transducer (LVDT) were carefully positioned to continuously record the expansions and contractions that occurred during thermal cycling. Post-test analysis of the individual dilatation curves was carried out using a best fit to the linear portions of the FCC and BCC contractions. The transformation start and finish temperatures were determined along with those for specific fractions of transformed austenite, including 2, 10, 50, and 90 and 98%. The transformation temperature data related to other major phase changes were also identified and subsequently used to calculate relative volume fractions of respective constituent phases using the lever rule. Final construction of the WM CCT diagrams was based on recorded transformation data, detailed post-test metallography and microhardness testing [40,41].

The full-sized specimens for subsequent Charpy-V-notch toughness testing were thermally cycled using a Type-K thermocouple spot welded to the middle of the WM surface in the location of the future notch. The same 15 mm grip spacing was employed to produce triplicate sets of specimens using the same simulation programs with a heating rate of 250°C/s, peak temperature (Tp) 1300°C, hold time of 1 s and a range of cooling times $\Delta t_{800\text{-}500}$ = 5, 10, or 20 s. These cooling times were selected to be relevant for a range of pipeline girth welding processes and procedures. The fastest reproducible cooling time achievable for the Charpy geometry was five seconds.

3.6 Metallography and Microhardness Testing

All metallographic specimens, including full cross sections from the series of experimental welds, were prepared using standard semi-automatic metallographic techniques. For this, the full cross sections (~10 mm thick by 32 mm wide) were cut from the mid-length of the experimental welds and surface ground. As seen in Figure 3 a short metallographic section (~25 mm long) was cut (using EDM) to reveal the through-thickness plane of the weld bead after thermal cycling. This orientation was the same as used for the actual plate welds. All specimens were mounted in epoxy resin and further ground and subsequently polished using a series of diamond suspensions and a final polish with a 0.05 µm colloidal silica suspension. The specimens were etched in 3% Nital solution for examination and evaluation using light optical microscopy. Representative macrographs of the experimental welds were created using the mosaic feature available on the Zeiss Axiovert microscope. Figure 6 shows a representative macrograph and the locations (white rectangular boxes) selected for examination of the microstructural features within the 1.5 kJ/mm deep-fill and underlying 0.5 kJ/mm fill passes. Both as-deposited and reheated regions were characterized and several images were recorded at a range of magnifications to help quantify the constituent phases formed within the respective weld metal regions. The nomenclature used to describe the constituent phases was based in part on the IIW classification scheme with grain boundary ferrite (GBF), ferrite with aligned second phase (FS(A)) and acicular ferrite (AF) being used in conjunction with the displacive transformations of bainite (B) and martensite (M) that are found in the high strength WM [42]. In selected cases, further details of the fine-scale microstructures were revealed using scanning electron microscopy. Microhardness traverses (dashed lines) were carried out as shown in Figure 6 using a diamond pyramid indenter with a

300 gram force. The spacing between indents was constant at approximately 0.5 mm for both the through-thickness and cross-weld surveys.
For the large number of thermal cycled WM CCT specimens, longitudinal samples spanning the reduced section were precision cut by CNC-Wire EDM to reveal a through-thickness weld metal cross-section orientation for detailed examination using LOM. The sections were prepared in the same manner as described above. Microhardness testing was confined to the central thermal cycled region to allow the range and average microhardnesses, as a function of thermal cycling condition, to be determined.

3.7 Toughness Testing

To assess the notch toughness, triplicate Charpy impact tests were conducted at -20°C. Specimens from the X100 pipe and the experimental welds in both as-welded and thermally-cycled conditions were converted to 2/3 sub-size samples with through-thickness notch orientation, as commonly used to assess weld metal notch toughness. Converting the specimens to 2/3 sub-size dimensions allowed a direct comparison between the as-deposited (as-welded) weld metal in the 1.5 kJ/mm weld and the thermally-simulated specimens produced with the fastest cooling rate ($\Delta t_{800\text{-}500}$ = 5 s) achievable to be made. For selected welds (LA100, NiMo80 and PT-01), standard full-size Charpy specimens subjected to imposed cooling times ($\Delta t_{800\text{-}500}$ = 5, 10, or 20 s) were subsequently surface-notched from the hot pass side and tested at -20°C. With a notch depth of 2 mm very little, if any, of the underlying low-energy-input weld metal would be tested using this notch orientation. Post-test examinations of all fractured specimens were used to confirm the mode of failure and record the percentage shear as outlined in ASTM Standard E23 [43].

4 RESULTS

4.1 Chemical Composition

The chemical compositions of the weld metals and the X100 pipe steel are listed in Table 1. In this table, the calculated carbon equivalents and transformation start temperatures (B_s and M_s) are also provided to give an indication of the relative hardenabilities. The major differences were in %C, %Ni, %Cr, and %Mo. These differences are reflected in the range of calculated carbon equivalents: CE_{IIW}= 0.46 to 0.65, P_{cm}= 0.21 to 0.28 and CEN= 0.31 to 0.44. The calculated transformation start temperatures (B_s = 623 to 533 °C and M_s = 457 to 418 °C) follow the expected trend of decreasing temperature with increasing alloy content.

4.2 Microstructure and Microhardness

For the series of experimental welds, a comparison between the microstructure and microhardness of the 1.5 kJ/mm deep-fill pass and underlying 0.5 kJ/mm fill passes was carried out to supplement the analysis of the WM thermal simulation experiments and provide a better understanding of their respective transformation behaviours. This allowed the influence of energy input (thermal cycle), single pass versus multipass welding, and effect of increasing alloy content (CEN ranging from 0.31 to 0.44) to be investigated. Representative micrographs of the as-deposited (AD) and reheated (RH) regions of the 1.5 kJ/mm deep-fill pass were compared to

the corresponding regions within the underlying 0.5 kJ/mm fill passes, as shown in Figure 7 and 8, 10 and 11, 13 and14, 16 and17 and 19 and 20. The microhardness results from both through-thickness and cross-weld traverses are presented in the charts immediately after the respective micrographs (Figure 9, 12, 15, 18 and 21). The average, range, and standard deviation of the respective microhardness data is also summarized in Table 2.

In all cases, it can be seen that the as-deposited weld metal microstructure of the 1.5 kJ/mm deep-fill pass is generally coarser and significantly softer than the structure formed in the underlying 0.5 kJ/mm weld passes. This primarily occurs as a result of differences in energy input which alters the thermal cycle, especially the cooling time ($\Delta t_{800\text{-}500}$) through the transformation range. It is also important to notice that reheated weld metal generated by deposition of the 1.5 kJ/mm deep-fill pass over the underlying third-fill pass generally resembles the microstructural constituents formed within respective AD regions, although they tend to differ in grain size and shape. This observation is very important in terms of constructing applicable WM CCT diagrams based on high-temperature reheating for the series of experimental welds investigated in this study. The hardness data (Table 2) also shows very consistent trends, with much less variation for the 1.5 kJ/mm weld than for the underlying 0.5 kJ/mm weld. An example of this trend is clearly illustrated in Figure 15 for the through-thickness hardness profile of the NiMo80 weld, where fairly uniform hardness exists for the 1.5 kJ/mm weld region while an alternating pattern of hardness is observed for the underlying 0.5 kJ/mm weld region. In the latter region, the hardness variation corresponds well with the distributions of AD and RH (and tempered) weld metal regions.

The specific differences in microstructure and microhardness for the series of experimental welds are further summarized in the section below. The main microstructures formed in these types of welds include acicular ferrite (AF), grain boundary ferrite (GF), ferrite-with second phase (aligned and non-aligned (FS(A) or FS (N)) or upper bainite (B), and lath martensite (M).

- LA90 weld: Figure 7 and Figure 8. For the 1.5 kJ/mm weld the microstructure consists predominately of AF with occasional discontinuous GF, whereas in the 0.5 kJ/mm region very little GF was formed and the as-deposited metal consists of much finer constituent phases. Notice that the prior austenite grains are considerably narrower in the low-energy-input weld and that a mainly AF microstructure formed in both the 1.5 kJ/mm AD and reheated weld metal regions. There is relatively uniform hardness in the 1.5 kJ/mm weld and much more cyclic hardness in the underlying 0.5 kJ/mm weld metal (Figure 9). This variation is also reflected in the ranges and standard deviations of microhardness, presented in Table 2.
- LA100 weld: (Figure 10 and Figure 11). For this weld, a mixed microstructure consisting of GF, FS(A) or (N) and AF is present in the 1.5kJ/mm weld, whereas much finer martensitic/bainitic constituent phases are seen in the 0.5 kJ/mm input weld. The difference in average hardness for the through-thickness traverses (267 to 297 HV), versus the cross-weld traverses (278 to 324 HV), is consistent with the observed microstructures. The cyclic pattern of hardness seen in both the (TT and CW) hardness traverses in Figure 12 is also indicative of a mixed microstructure.
- NiMo80 weld: (Figure 13 and Figure 14). In the 1.5 kJ/mm deep-fill pass the microstructure

consisted mainly of AF with some discontinuous GF or FS(A) or FS(N) (averages of 274 to 270). In contrast, the very narrow prior austenite grains within the lower energy input weld transformed to a much finer high hardness (averages of 332 to 341) martensitic/bainitic microstructure. Again there was a wider range of hardness and correspondingly higher standard deviation for the low-energy-input multipass weld region (Figure 15 and Table 2). The cyclic or saw-tooth hardness profile with higher and lower hardness values correspond to the AD and RH (and tempered) zones that are known to exist in multipass welds.

- PT-01 weld: (Figure 16 and Figure 17). The WM microstructures formed in this weld were similar to those for the NiMo80 weld. This was initially expected based on the small difference in CEN values even though there are larger differences in CE_{IIW} values and lower calculated Bs and Ms temperatures (Table 1). There is a noticeable refinement of the AD microstructures and remarkable similarity between the AD and reheated WM microstructures in this case. The increased microhardness relative to NiMo80 (especially for the 1.5 kJ/mm deep-fill pass) suggests formation of finer and/or different amounts of lower-temperature transformation products (Figure 18 and Table 2).
- PT-02 weld: (Figure 19 and Figure 20). With the highest alloy content (CEN value of 0.44), the 1.5 kJ/mm weld transforms at low temperatures to a predominantly high hardness lath martensite with some bainite (averages of 338 HV). Very spare discontinuous GF or FS(A) was occasionally observed. The increase in microhardness observed for the lower-energy-input weld (averages of 382 to 375 HV) supports transformation to a largely martensitic microstructure. In Figure 21, the through-thickness traverse varies more in the multipass region, while the cross-weld profile shows a dip (decrease) at the weld centerline.

4.3 Thermal Simulation

4.3.1 Dilatometric Analysis

The complete series of dilation curves obtained for the WM samples is shown in Figure 22 to Figure 26. The individual curves were analyzed using Origin software to establish the transformation data required to construct WM CCT diagrams and to ultimately determine the transformation behaviours of the respective weld metals. Details of the method used to establish the transformation temperature has been reported by Goodall et al [41]. Briefly, the contraction of the FCC phase from 1000°C to 20°C above the obvious expansion was linearly fit. Likewise, the BCC thermal contraction region post expansion was also linearly fit. The fraction of austenite transformed was then calculated using the algebraic projections of the linear best-fit lines. The transformation-start temperature was taken at the point of 2% deviation from the FCC contraction as it provided improved reproducibility, although in this work the 0% deviation is also provided. Other fractional transformational volumes (10, 50, 90 and 98%) were also calculated. All curves were re-examined in detail at an expanded scale to establish if there were any significant inflection points between the T_s and T_f temperatures. This was used to calculate the relative proportion of phases present using the lever rule; see, for example, the dilatation curves for LA90-2s, NiMo80-5s, and PT02-10s. In some selected cases, portions of dilatation curves with interesting features were analyzed using the first-derivative method. In all cases the finish temperatures were established using both 98 and 100% fraction transformed.

Figure 22 to Figure 26 reveal the expected tendency for the onset of major transformations to occur at higher temperatures as a function of increasing cooling times, especially for $\Delta t_{800\text{-}500} \leq$ 10s. It is clear that lower overall transformation temperatures are observed with the higher-alloyed WMs (increased hardenability). The range over which the major transformations occur is also evident in these figures; see, for example, LA90 where the major transformation occurs between ~525 and ~625°C, whereas the transformation temperatures of PT02 are between ~425 and 525°C.

4.3.2 WM CCT Diagrams, Microstructure and Microhardness

The five WM CCT diagrams constructed using dilatometric data along with information from post-test metallography and microhardness testing are presented in Figure 27 through Figure 37. The nomenclature used to describe the constituent phases uses both the conventional weld metal IIW classification in particular FS along with the predominantly displacive transformations of acicular ferrite (AF), bainite (B) and martensite (M) found in the high strength WM [42]. Limited amounts of grain boundary ferrite (GF) were expected at the cooling rates tested and this required confirmation using post-test metallography, before being added to the respective CCT diagrams. The initial start temperatures are based on 0% and 2% offset, while the finish temperature was determined for 100% transformation. Intermediate T_{50} and T_{90} temperatures are also included along with the corresponding microhardnesses. Representative micrographs for cooling times $\Delta t_{800\text{-}500}$ = 2, 5, 10, and 20 s are presented immediately after the WM CCT diagrams to show the change in microstructure that occurred for the respective WMs. Two general trends that were observed from the dilatometric experiments were an overall coarsening of microstructure and a dramatic reduction in microhardness (decreases of 23 to 31%) for cooling times between $\Delta t_{800\text{-}500}$ = 2 and 10 s (Figure 37) for all but the highest alloyed WM where a 10% decrease was observed. More gradual decreases in hardness are observed for the longer cooling times ($\Delta t_{800\text{-}500}$ = 20 and 50 s). The specific microstructural features and observations for each WM composition are described below.

The CCT diagram for the LA90 weld is shown in Figure 27. It was determined from the dilation curve for the shortest cooling time (free cool) that a mixed microstructure, consisting of approximately 75% (GF, B, and AF) and 25% M had formed (Figure 22). The very fine lath structure exhibited an average hardness of 342 HV (329-349). The presence of GF and FS(A) (upper bainite) was confirmed by post-test metallography (Figure 28). With increasing cooling time the proportion of M decreased and more GF and FS(A) phases were formed along with AF becoming the dominate structure. Figure 28(c) shows that a coarser AF lath structure for the $\Delta t_{800\text{-}500}$ = 10s (avg. 259 HV (250-264)) and a considerable fraction of secondary microphase, presumably martensite–austenite (M-A) interspersed between the laths. Limited GF and FS(A) is also present. At cooling times $\Delta t_{800\text{-}500}$ = 20 and 50 s, overall coarsening of the AF laths and GF occurred along with the formation of intragranular polygonal ferrite grains, which lead to a further reduction in microhardness.

The WM CCT diagram for the LA100 weld is presented in Figure 29. A much wider range of constituent phases was found within the well-defined equiaxed prior austenite grains. The mixed microstructure is consistent with the greater variation in microhardness, especially for the intermediate cooling times where the ranges and standard deviations are the highest. Figure 30(a)

shows the microstructure formed with $\Delta t_{800\text{-}500}$ = ~2 s. Although some GF and FS(A) (upper bainite) regions were evident, the majority of the grain interiors transformed to fine bainite/martensite (~85% from the dilatation curve). With increasing cooling time similar mixed microstructures formed; however, from the dilatation curve there is a marked reduction in the proportion of martensite (~20%) for the cooling time $\Delta t_{800\text{-}500}$ = 5 s. Optically (Figure 30 (b)) there appears to be a large proportion of bainite and martensite. In some grains it can be seen that the bainitic ferrite laths extend completely across the prior austenite grains, while in other grains fine lath M appears to dominate. At a cooling time of $\Delta t_{800\text{-}500}$ = 10 s, there is a marked increase the fraction of bainite with AF. In some areas the bainitic ferrite laths are separated by M-A microphases. These observations are consistent with the overall reduction in average hardness 267 HV (254-276). A further increase in the cooling time leads to the development of a predominantly AF structure with coarser laths and wider discontinuous GF veins with some occasional coarse FS(A) regions.
Figure 31 shows the CCT diagram for the NiMo80 weld. The optical micrograph of the free-cooled NiMo80 WM, shown in Figure 32, reveals predominantly high-hardness martensitic structure (average 410 HV (398-416)). FS(A) regions were occasionally observed. Light-etching boundaries that are apparent over the structure (ghosting effect) is believed to be related to the underlying dendritic structure formed within this weld metal. From the dilatation curve obtained for the free cool the martensite start temperature was suppressed by the earlier onset of transformation at a higher temperature (to bainite). That very fine structures formed at $\Delta t_{800\text{-}500}$ = 3.5 and 5 s with relatively high average hardnesses of 372 and 334, respectively, supports transformation to predominantly bainitic/martensitic phases. Much more well defined laths, along with GF and FS(A) were also observed. Light-etching boundaries continued to be superimposed over the structure. For the cooling time $\Delta t_{800\text{-}500}$ = 7.5 s AF dominates, although based on the range of microhardness (avg. 312 (303-320)) other transformation products may also be present. For the $\Delta t_{800\text{-}500}$ = 10 and 20 s, there was a slight coarsening of the predominantly AF structure and some discontinuous GF and FS(A) formed. It was also evident for these specimens and the $\Delta t_{800\text{-}500}$ = 50 s specimen that MA microphases were interspersed throughout the AF lath structure.

In Figure 33, the WM CCT diagram for PT01 indicates that relatively high hardness exists for cooling times $\Delta t_{800\text{-}500}$ = 2 to 10 s, despite the obvious change from predominantly-martensitic/ bainitic to AF-dominated microstructure. Based on the optical micrograph in Figure 34, the almost-fully-martensitic structure has some unusually coarse laths dispersed throughout the grain interiors. A significant reduction in the proportion of martensite was detected for $\Delta t_{800\text{-}500}$ = 3.5 and 5 s. It is interesting that nearly identical microhardness results were obtained: 369 Hv (360-377) and 364 Hv (349-384) respectively. At $\Delta t_{800\text{-}500}$ = 7.5 and 10 s, the presence of AF along with increased proportions of GF, FS(A) and M-A microphases was found. The formation of M-A phase is consistent with the delayed finish indicated in the respective dilatation curves. With longer cooling times a coarser AF structure with reduced hardness (averages of 275 and 253 Hv) was observed.

Figure 35 shows the WM CCT diagram for PT-02. It can be seen that higher hardness values were measured for all samples. The WM sample that was subjected to a free cool exhibited lower hardness than expected and it did not fit the trend observed for previous series of simulated WMs. However, the fully martensitic structure appeared to be unusually coarse with large laths

that may account for the lower-than-expected hardness (Figure 36). Interestingly the maximum hardness is within the range measured for both the $\Delta t_{800\text{-}500}$ = 3.5 and 5 s where the simulated structures appeared to be very fine lath martensite with very little difference in dilatation curves. Analysis of the dilatation curves for the $\Delta t_{800\text{-}500}$ = 7.5 s and 10 s samples show that the proportion of martensite was estimated to further decrease from ~30% to ~20%. Comparatively high hardnesses were maintained at longer cooling times, which is consistent with the relatively low transformation temperatures and formation of mainly AF.

4.3.3 WM Charpy Toughness

Some initial Charpy impact toughness testing was carried out to provide a comparison between the experimental welds and a selection of single-cycle thermal simulation conditions. It was decided based on limited available weld material to proceed using two different sets of Charpy specimens that would be tested at -20°C. The first set of tests used 2/3 sub-size specimens with a through-thickness weld centerline notch orientation to assess the toughness of the 1.5 kJ/mm deep-fill pass (denoted WMC-AW) against those that were thermal cycled using a Tp=1300°C and cooling time $\Delta t_{800\text{-}500}$= 5 s (denoted 1300-5s) for the complete range of weld compositions. Comparable impact toughness data for the X100 (Grade 690) pipe steel was also obtained and is listed, along with the proportionally adjusted full-size equivalent impact energies, in Table 4. Photographs of the fracture surfaces of selected Charpy specimens and the percentage shear are also provided in the table. Very consistent results were generally obtained for the triplicate tests. The results show that specimens from the welds and those that were thermally cycled had impact energies significantly lower (50% or less) than those recorded for the X100 pipe steel, which exhibited 157 J with 100% shear. In all cases the WMC-AW results from the 1.5 kJ/mm deep-fill passes exhibited impact energies and percent shear values higher than the corresponding thermally-cycled samples. Comparing the impact energies for each series of welds provides the following rankings: LA90 exhibits the highest WM toughness followed by the NiMo80, PT-01 and the nearly identical results obtained for both LA100 and PT-02 (lowest absorbed energies).

The results from the second set of Charpy notch toughness tests (Table 5), which were completed for three WM compositions (LA100, NiMo80 and PT-01) and a wider range of cooling times, revealed consistent trends with an initial decrease in toughness for the 1300-5 s specimens compared to the AW condition. Note in this case that the simulation results are very similar for all three welds with averages of 66, 67 and 63 J, respectively). With further increase in cooling time (1300-10s to 1300-20s), there is a significant increase in measured toughness and higher percent shear values.

Comparison of the two sets of Charpy results revealed the same general trend, although for the LA100 and NiMo80 welds the results for full-size CVN specimens are slightly higher than the equivalent values for the 2/3 sub-size samples, whereas the results for PT-01 are identical in both cases.

5 DISCUSSION

In this investigation, thermal simulation techniques were employed to study the influence of continuous cooling and composition (CEN values ranging from 0.31 to 0.44) on WM microstructure, hardness, and notch toughness. The continuous cooling transformation behaviour of the weld metals was studied via dilatometric experiments for cooling times relevant to a wide range of pipeline girth welding process options, especially those relevant to narrow-gap mechanized GMAW-P. The microstructures of the specially designed experimental plate welds, which contained a 1.5 kJ/mm final deep-fill pass and three 0.5 kJ/mm underlying fill passes, were also subjected to detailed characterization and compared to the corresponding simulated WM samples produced over a range of cooling conditions. The following sections provide further analysis and discussion of the results and observations made with respect to specific weld metal compositions chosen for this study.

5.1 Hardness of Experimental Plate Welds Versus Simulated WM

Correlations between WM hardness and chemical composition (carbon equivalent) have been established for the range of experimental plate welds investigated. Figure 38 shows the trend in hardness as a function of CE_{IIW} and CEN. It can be seen that reasonable correlations have been found for both weld regions (0.5 and 1.5 kJ/mm) and that the CEN generally provides improved overall fit to the data. Therefore, CEN was used for further analysis and comparison between these results and those for the simulated WM samples. Correlations using the range (minimum and maximum) microhardness values were also examined. This was considered important, especially for the 0.5 kJ/mm welds where the alternating pattern of high and low hardness, which followed the distribution of AD and RH weld metal regions, might lead to improved correlations as seen in Figure 39. These results are compared against the average data. Overall the correlations are not as good, which may be related to the very limited data used to describe the upper and lower range of hardnesses (essentially the maximum and minimum values).

The hardness results from the WM CCT samples, which used cooling times applicable to the actual plate welds, were superimposed onto the respective charts in Figure 40. In the first case (1.5kJ/mm), it is clear that lines for $\Delta t_{800\text{-}500}$ = 10 and 20s lie on top of the maximum and minimum trend lines, respectively. The difference in slope for the 1300-10s trend line means that the line is initially below the maximum trend line at low CEN values, crossing at the mid point and is slightly above at the highest CEN. In contrast, there is very close agreement between the trend lines for the 1300-20 s and the lower bound hardness of the 1.5 kJ/mm WM. This suggests that a cooling time closer to $\Delta t_{800\text{-}500}$ = 15 s should have a closer match to the average data (Figure 40(a)). The assumption that there should be close agreement between the original AD and high-temperature reheated WM in terms of microstructure and hardness is believed valid provided the thermal cycle conditions are similar.

For the low-energy-input case (Figure 40(b)), the data for the simulated WM with cooling times $\Delta t_{800\text{-}500}$ = 2 and 5 s were used for comparison against the maximum values. Clearly, there are different slopes for the trend lines and the fit for the 1300-2s is poor. A cooling time between $\Delta t_{800\text{-}500}$ = 2 and 5 s would be required to closely match the hardness for the complete range of

weld compositions, especially at lower CEN values, which is consistent with the dramatic change in hardness observed for all put the highest-alloyed WM (Figure 37). This is very encouraging given that cooling times of $\Delta t_{800\text{-}500}$ = of 3 to 5 s have been measured and predicted for the single-torch welding conditions similar to those used to produce the multipass portion of the experimental plate [9].

5.2 CCT Diagrams and Microstructure

The WM CCT diagrams constructed in this investigation are based on analysis of the dilatation data and evaluation of microstructures from optical microscopy as well as corresponding hardness data. The range of WM microstructures formed were strongly dependent on the chemical composition and imposed thermal cycles ($\Delta t_{800\text{-}500}$ = ~2 to 50 s). For all WM compositions there was a significant reduction in measured hardness for cooling times $\Delta t_{800\text{-}500} \leq 20$ s that was generally followed by a more gradual decrease for the longer cooling times (Figure 37). This finding is very important and relevant to the development and evaluation of single-and dual-torch welding procedures. That marked changes in microstructure and corresponding hardness occurs over the short range of cooling times applicable to narrow-gap single and dual torch mechanized welding is important to understand. For both process variants relatively small changes in preheat and/or interpass temperatures, torch separation (distance between the weld pools), or even pipe wall thickness can lead to changes in cooling times that must be considered when developing welding procedures for high strength steel pipe.

The CCT experiments have provided an improved characterization of microstructures formed in the range of WM alloy systems investigated and established a useful tool for welding engineers in the development of welding procedures applicable to joining high strength steel pipe [44]. Specific information obtained includes the change in transformation start temperatures and qualitative fractions of constituent phases formed as a function of increasing cooling times (known thermal cycles). In the leanest alloy (LA90), a mixed fine B with ~ 25% M structure was formed at short cooling time, which progressively changed to mainly AF with small amounts of FS(A) and GF with increasing cooling times. The increased alloy content of LA100 resulted in an initial formation of a high proportion of M with some B that progressively had increasing volume fractions of bainite and AF with longer cooling times. Both NiMo80 and PT01 WM exhibited mainly martensite to AF-dominated structures. Based on dilatation data for the free cooled sample, ~60% M with ~40% B initially formed in NiMo80 sample. This was followed by a progressive decrease in the portion of M until AF-dominated structures were formed at $\Delta t_{800\text{-}500}$= 10 s and beyond. For the PT01 weld, which had a slightly higher CEN value, a high hardness almost fully martensitic structure was formed with fast cooling. With only small increases in cooling time, $\Delta t_{800\text{-}500}$= 3.5 and 5 s, there was a significant decrease in the proportion of martensite (33% and 23%) and a corresponding increase in fine bainite, which resulted in a 10% decrease in hardness (from 404 to 369 and 364 Hv, respectively). With intermediate cooling times, increasing proportions of AF along with small amounts of GF and FS(A) were formed with a further reduction in hardness. The comparatively small increase in the transformation temperatures for the longest cooling times ($\Delta t_{800\text{-}500}$ = 20 and 50 s) lead to an overall coarsening of the microstructure and further decrease in hardness. In the PT-02 weld, significant amounts of M were formed over a wider range of cooling times: close to 100% for the fast cooling time, that decreased to ~20% for $\Delta t_{800\text{-}500}$ = 20 s. The decrease in M was accompanied by an increase in the

proportion of B with relatively high hardness even when AF was observed at longer cooling times, $\Delta t_{800\text{-}500}$= 20 and 50s.

Because of the very fine scale of the microstructures formed in the simulated WM samples and the difficulty in classifying the microstructures using only optical microscopy, selected samples from LA100, NiMo80 and PT-01 were examined using scanning electron microscopy. It is evident from the images in Figure 41(a) that considerable upper bainite (FS(A)) and finer bainite/lath martensite phases formed at a cooling time, $\Delta t_{800\text{-}500}$ = 5 s in the LA100 sample. The microstructure changes to a more AF-dominated structure at intermediate cooling times although some coarse bainitic regions and GF also exist, as evident in Figure 41(b) and (c). With increased alloy content, welds NiMo80 and PT-01, initially exhibit finer elongated lath martensitic/bainitic structures with some AF laths and occasional upper bainite (FS(A)) (Figure 42 and Figure 43). The morphologies of the WM structures clearly change within each sample and with increasing cooling time, where formation of shorter and wider lath-like constituents is observed. The change in microstructure for NiMo80 is quite dramatic as evident in the change from very fine laths to much coarser laths with occasional GF and polygonal ferrite more prevalent for longer cooling times. For PT-01, the lower-transformation-temperature phases, with elongated narrow laths, exist for all three cooling times and help to explain the consistently higher hardness values observed for the simulated WM with cooling times $\Delta t_{800\text{-}500} \geq 5$ s (Figure 37). These observations are in agreement with those reported by Fairchild et al [34] for the series of high strength weld metal investigated during the development of optimized weld metals for joining X120 pipe. They showed that AF could be engineered to co-exist within bainitic/martensitic-type WM microstructures and that the morphology of AF was influenced not only by WM chemistry, but also by the cooling rate for the welding conditions employed.

5.3 WM Toughness

Although only a limited amount of Charpy impact toughness testing of the experimental plate welds and thermally simulated WM was possible in this study, some consistent trends were found. There was a tendency towards lower toughness with increasing alloy content and for fast cooling conditions (short cooling time) where high-hardness microstructures were more likely to be formed (Table 4 and 5). For the series of tests conducted using surface-notched full-size CVN specimens, a clear trend towards increasing impact energy with increasing cooling time was observed for all three compositions evaluated. Using the as-welded condition as a baseline, there was an initial decrease in impact energy for samples thermally cycled using $\Delta t_{800\text{-}500}$ = 5 s. This was followed by a marked increase in impact toughness for a further doubling of the cooling times to $\Delta t_{800\text{-}500}$ = 10 and 20 s. The improved toughness is consistent with the formation of softer more AF-dominated structures in the simulated WM specimens. It is also important to mention that the simulated WM specimens consist of high-temperature reheated WM, which is expected to exhibit more equiaxed rather than columnar-type grain structures that are normally present in the as-deposited region and this in itself can favourably affect the resultant notch toughness.

6 SUMMARY AND CONCLUSIONS

Five specially-designed experimental plate welds were made using two distinctly different GMAW-P procedures with wire electrodes applicable for joining X100 pipe. The weld procedures consisted of three initial fill passes deposited at 0.5 kJ/mm and a final deep-fill pass at 1.5 kJ/mm to just fill the narrow-gap joint. Equal portions of the welds were used to make Gleeble specimens suitable for evaluation of the transformation behaviours as well as selected notch toughness properties of the respective WMs. An important part of the research focused on development of WM CCT diagrams using radial dilatometry and post-test metallography to establish the influence of composition and thermal cycle (cooling times) on formation of fine-scale, predominantly displacive M, B and AF transformations. This is particularly useful and relevant for implementation of pipeline welding options, including single- and dual-torch variants where relatively small changes in process/procedure essential variables have been shown to affect the mechanical properties of welds produced in X100 pipe [5,6,10,11,15,31,38]. The evaluation of the experimental plate welds in conjunction with the thermal simulation results allow the following conclusions to drawn.

1) The specially-designed experimental plate welds produced with carbon equivalent (CEN) values ranging from 0.31 to 0.44 allowed both real and thermal simulated WM regions to be characterized in terms of microstructure, hardness and notch toughness.

2) For the series of experimental plate welds the microstructure and hardness were found to follow a consistent trend with the 1.5 kJ/mm deep-fill pass exhibiting a generally coarser and overall softer microstructure than in the underlying 0.5 kJ/mm multipass weld region. The microstructures ranged from AF-dominated to bainitic/martensitic with increasing alloy and increasing cooling rates (shorter cooling times) of the 0.5 kJ/mm multipass welds.

3) The microstructure and microhardness correlated reasonably well with CEN for the 1.5 kJ/mm deep-fill pass and the 0.5 kJ/mm multipass weld. In the latter case, the observed alternating pattern of hardness corresponded well with the distribution of AD (high values) and RH (low values).

4) RH WM microstructure generated by deposition of the 1.5 kJ/mm deep-fill pass over the underlying 0.5 kJ/mm weld pass was generally observed to resemble the microstructure formed within the columnar as-deposited regions of the 1.5 kJ/mm deep-fill pass, although the grains tended to be more equiaxed in the reheated region.

5) Dilatometric experiments on single-pass weld metal specimens provided very useful information on the transformation behaviour of high strength WM, including the transformation temperatures and in some cases the relative proportions of respective phases to be quantified. The results, presented in the form of WM CCT diagrams, clearly show the microstructural evolution as a function of increasing hardenability and cooling time. Over the range of cooling times investigated the lowest-alloyed WM (LA90) exhibited microstructures dominated by bainite/martensite to AF, whereas the highest-alloyed WM (PT02) formed large fractions of martensite/bainite to AF.

6) For a given WM composition there was a marked change in microhardness of the thermally simulated WM microstructures resulting from the relatively small range of cooling times $\Delta t_{800\text{-}500}$ = 2 to 10 s followed by a more gradual decline for further increases in cooling time.

7) For sub-size CVN specimens there was a decrease in impact energy for the simulated WM using Tp=1300°C with $\Delta t_{800\text{-}500}$ = 5 s compared with 1.5 kJ/mm AW condition and a trend towards decreasing notch toughness with increasing WM hardenability.

8) For surface-notched full-size CVN simulated specimens (Tp=1300°C and $\Delta t_{800\text{-}500}$ = 5, 10 and 20 s) there was a similar decrease in toughness for the shortest cooling time ($\Delta t_{800\text{-}500}$ = 5 s) followed by an increase in toughness for longer cooling times.

7 ACKNOWLEDGMENTS

This research was funded, in part, by CANMET-MTL and the Federal Program for Energy Research and Development. The authors would like to thank CANMET-MTL staff, including Mr. M. Kerry for his machining expertise, Mr. R. Eagleson for performing mechanical testing, and Ms P. Liu and R. Zavadil for expert metallographic analysis and microhardness testing. The technical expertise of Mr. M. Carroscia, Lincoln Electric, is also appreciated. The author (GG) also wishes to acknowledge CANMET-MTL management for providing the opportunity to work and have access to laboratory facilities during the course of this research and to NSERC and McGill University for funding grants. This research is part of a consolidated program jointly funded by the Pipeline and Hazardous Materials Safety Administration of the U.S. Department of Transportation (DOT), and the Pipeline Research Council International, Inc. (PRCI).

8 REFERENCES

1. DOT-PRCI, "Update of Weld Design, Testing, and Assessment Procedures for High Strength Pipelines," http://primis.phmsa.dot.gov/matrix/PrjHome.rdm?prj=225, 2007-2011.
2. DOT-PRCI, 2007 "Development of Optimized Welding Solutions for X100 Linepipe Steel," http://primis.phmsa.dot.gov/matrix/PrjHome.rdm?prj=226, 2007-2011.
3. Quintana, M., and Hammond, J., "X100 Welding Technology – Past, Present and Future," International Pipeline Conference, ASME, IPC2010-31421, pp. 1-10, 2010.
4. Chen, Y., Wang, Y., Gianetto, J., Rajan, V., Quintana, M., "Simulation of Microstructure Evolution and its Experimental Verifications for Girth Welds in High-Strength Pipelines," International Pipeline Conference, ASME, IPC2010-31374, pp. 1-6, 2010.
5. Gianetto, J., Tyson, B., Wang, Y.-Y., Bowker, J., Park, D., and Shen, G., 2010 "Properties and Microstructure of Weld Metal and HAZ Regions in X100 Single and Dual Torch Girth Welds," International Pipeline Conference, ASME, IPC2010-31411, pp. 1-11, 2010.
6. Rajan, V., Chen, Y. and Quintana, M., 2010 "A New Approach to Essential Welding Variables in Girth Welding of High Strength Pipe Steels," International Pipeline Conference, ASME, IPC2010-31374, pp. 1-8, 2010.
7. Wang, Y-Y., Liu, M., Gianetto, J. and Tyson, B. 2010 "Considerations of Line Pipe and Girth Weld Tensile Properties for Strain-Based Design of Pipelines," International Pipeline Conference, ASME, IPC2010-31376, pp. 1-10, 2010.
8. Wang, Y-Y., Liu, M., Tyson, B., Gianetto, J. and Horsley, D., 2010 "Toughness Considerations for Strain-Based Design," International Pipeline Conference, ASME, IPC2010-31385, pp. 1-11, 2010.

9. Panday, R. and Daniel, J., "Materials Selection, Welding and Weld Monitoring", Final Report 278-T-02 to PHMSA per Agreement # DTPH56-07-T-000005, September 2011.
10. Gianetto, J.A., Goodall, G.R., Tyson, W.R., Quintana, M.A., Rajan, V.B and Chen, Y., "Microstructure And Hardness Characterization Of Girth Welds", Final Report 278-T-03 to PHMSA per Agreement # DTPH56-07-T-000005, September 2011.
11. Gianetto, J., Goodall, G.R., Tyson, W.R., Quintana, M.A., Rajan, V.B. and Chen, Y., "Microstructure and Properties of Simulated Heat Affected Zones", Final Report 278-T-05 to PHMSA per Agreement # DTPH56-07-T-000005, September 2011.
12. Gianetto, J.A., Tyson, W.R., Park, D.Y., Shen, G., Lucon, E., Weeks, T.S., Quintana, M.A., Rajan, V.B. and Y.-Y. Wang, "Small Scale Tensile, Charpy V-Notch, and Fracture Toughness Tests", Final Report 277-T-05 to PHMSA per Agreement # DTPH56-07-T-000005, September 2011.
13. Park, D.Y., Tyson, W.R., Gianetto, J.A., Shen, G., Eagelson, R., Lucon, E. and Weeks, T.S., "Development of Optimized Welding Solutions for X100 Line Pipe Steel-Small Scale Low Constraint Fracture Toughness Test Results", Final Report 277-T-06 to PHMSA per Agreement # DTPH56-07-T-000005, September 2011.
14. Park, D.Y., Tyson, W.R., Gianetto, J.A., Shen, G., Eagelson, R., , E. and Weeks, T.S., "Development of Optimized Welding Solutions for X100 Line Pipe Steel-Small Scale Low Constraint Fracture Toughness Test Discussion and Analysis", Final Report 277-T-07 to PHMSA per Agreement # DTPH56-07-T-000005, September 2011.
15. Rajan, V.B., 2011 "Essential Welding Variables", Final Report 278-T-09 to PHMSA per Agreement # DTPH56-07-T-000005, September 2011.
16. Chen, Y., Wang, Y-Y., Quintana, M.A., Rajan, V.B. and Gianetto, J.A., "Thermal Model for Welding Simulations", Final Report 278-T-07 to PHMSA per Agreement # DTPH56-07-T-000005, September 2011.
17. Chen, Y., Wang, Y-Y., Quintana, M.A., Rajan, V.B. and Gianetto, J.A., "Microstructure Model for Welding Simulations", Final Report 278-T-08 to PHMSA per Agreement # DTPH56-07-T-000005, September 2011.
18. Rajan, V.B. and Daniel, J., "Application to Other Welding Processes", Final Report 278-T-09 to PHMSA per Agreement # DTPH56-07-T-000005, September 2011.
19. Lambert-Perlande, A., Gourgues, A.F., Besson, J., Strurel, T. and Pineau, A., "Mechanisms and modeling of Cleavage Fracture in Simulated Heat-Affected Zone Microstructures of a High-Strength Low Alloy Steel", ASME, Metallurgical and Materials Transactions A, Vol. 35A, No. 3, pp. 1039- 1053, 2003.
20. Shome, M. Gupta, O. P. and Mohanty, O. N., "Effect of Simulated Thermal Cycles on the Microstructure of the Heat-Affected Zone in HSLA-80 and HSLA-100 Steel Plates," Metallurgical and Materials Transactions A, Vol. 35A, pp. 985-996, 2004.
21. Onsoien, M.I., M'Hamdi, M., and Mo, A., "A CCT Diagram for an Offshore Pipeline Steel of X70 Type," The Welding Journal, Vol. 88, No. 1, pp 1s-6s, 2009.
22. Penniston, C., Collins, L., and Hamad, F. "Effects of Ti, C and N on Weld HAZ Toughness of High Strength Line Pipe," 7th Int. Pipeline Conf., ASME, IPC2008-64134, pp.1-9, 2008.

23. Huppi, G., "Reheat Zone Microstructural Development and Toughness in Selected HSLA Steel Weld Metals," Ph.D., Metallurgical Engineering, Colorado School of Mines - Center for Welding Research, Golden, 1986.
24. Harrison, P.L., and Farrar, R.A., "Application of continuous cooling transformation diagrams for welding of steels," Int. Materials Reviews, Vol. 34 No.1 pp. 35-51, 1989.
25. Farrar, R.A. and Z.Y. Zhang, "Experimental-Verification of the Continuous-Cooling Transformation Diagram Produced by the Dilatometry Metallography Method" Journal of Materials Science Letters, Vol. 12, No. 20, pp. 1606-1611, 1993.
26. Johnson, M. Q., Edwards, G.R. and Evans, G.M., "The Influence of Thermal Cycles on High Strength Steel SMA Weld Metal Microstructures and Properties" Proc. Of 4th Conference on Trends in Welding Research, ASM International, pp. 547-552, Gatlinburg, Tennessee, USA, June 5-8, 1995.
27. Tezuka, N., Shiga, C., Yamaguchi, T., Bosansky, J., Yasuda, K. and Kataoka, Y., 1995 "Toughness Degradation Mechanism for Reheated Mo-Ti-B Bearing Weld Metal" ISIJ International, Vol. 35, No. 10, pp. 1232-1238, 1995.
28. Fonda, R. W. and Spanos, G., "Microstructural Evolution in Ultra-Low-Carbon Steel Weldments - Part I: Controlled Thermal Cycling and Continuous Cooling Transformation Diagram of the Weld Metal," Metallurgical and Materials Transactions A, Vol. 31, pp. 2145-2153, 2000.
29. Thewlis, G., "Weldability of X100 linepipe," Science and Technology of Welding and Joining, Vol. 5 No.6 pp. 365-377, 2000.
30. Gliha, V., and Rojko, D., "The Influence of Simulated Thermal Cycle on the Formation of Microstructures of Multi-Pass Weld Metal," Metalurgija, Vol. 44 No.1, pp. 19-24, 2005.
31. Hudson, M.G., "Welding of X100 Linepipe," Ph.D. Thesis, Welding Engineering Research Centre, Cranfield University, 2004.
32. Gianetto, J.A., Bowker, J.T., Dorling, D.V. and Horsley, D., "Structure and Properties of X80 and X100 Pipeline Girth Welds," 5th Int. Pipeline Conf., ASME, IPC04-0316, pp. 1-13, 2004.
33. Gianetto, J.A., Bowker, J.T. and Dorling, D.V., "Assessment of Properties and Microstructure of X100 Pipeline Girth Welds," Welding in the World, Vol. 49, (11/12), pp. 71-89, 2005.
34. Fairchild, D., Macia, M., Bangaru, N., Koo, J., Ozekcin, A., and Jin, H., "Welding Development for the World's Strongest Pipeline: X120," 7th Int. Conference on Trends in Welding Research, ASM International, pp. 749-754, Pine Mountain, Georgia, USA, May 16-20, 2005.
35. Gianetto, J.A., Bowker, J.T., Bouchard, R., Dorling, D.V. and Horsley, D., "Tensile and Toughness Properties of Pipeline Girth Welds," Welding in the World, Vol. 51, (5/6), pp. 64-75, 2007.
36. Gianetto, J.A., Bowker, J.T., Dorling, D.V., Taylor, D., Horsley, D. and Fiore, S.R., "Overview of Tensile and Toughness Testing Protocols for Assessment of X100 Pipeline Girth Welds", 7th Int. Pipeline Conf., ASME, IPC2008-64668, pp. 1-10, 2008.

37. Fiore, S. R., Gianetto, J.A., Hudson, M. G., Vase, S., Khurana, S., Bowker, J.T. and Dorling, D.V., “Development of Optimized Weld Metal Chemistries for Pipeline Girth Welding of High Strength Line Pipe,” 7th Int. Pipeline Conf., ASME, IPC2008-64593, pp. 1-12, 2008.
38. Hamada, M., Shitamoto, H. and Hirata, H., “Tensile Properties and Microstructure of Girth Welds for High Strength Linepipe,” Proc. of 19th Int. Offshore and Polar Eng. Conf., ISOPE, Osaka, Japan, pp. 50-55, 2009.
39. W. Steven and A. G. Haynes, "The Temperature of Formation of Martensite and Bainite in Low-Alloy Steels," Journal of Iron and Steel Research International, 1956.
40. Goodall, G.R., Gianetto, J.A., Bowker, J., and Brochu, M., “CCT Diagrams and Impact Toughness Applicable to the GC HAZ Region Generated in X100 Line Pipe” CANMET-MTL Report 2011- 11(TR-R), 2011.
41. Goodall, G.R., Gianetto, J.A., Bowker, J., and Brochu, M., “CCT Diagrams of Weld Metal Applicable for Girth Welding of X100 Line Pipe,” CANMET-MTL Report 2011-12(TR-R), 2011.
42. Thewlis, G., “Material perspective - Classification and quantification of microstructures in steels,” Materials Science and Technology, Vol. 20(2), pp. 143-160, 2004.
43. ASTM Standard E23: Test Methods for Notched Bar Impact Testing of Metallic Materials, ASTM International, 100 Barr Harbor Drive, PO Box C700, West Conshohocken, PA 19428-2959, United States.
44. Quintana, M.A., “Summary Report 278 Development of Optimized Welding Solutions for X100 Line Pipe Steel”, Final Report 278-S-01 to PHMSA per Agreement # DTPH56-07-T-000005, September 2011.

Table 1. Experimental weld metal and X100 pipe compositions

Element Wt%	Experimental Welds					X100 Pipe
	LA90	LA100	NiMo80	PT-1	PT-2	Base Metal
C	0.084	0.064	0.100	0.087	0.097	0.061
Mn	1.6	1.5	1.4	1.5	1.6	1.78
Si	0.41	0.31	0.49	0.40	0.59	0.55
S	0.005	0.003	0.009	0.005	0.008	<0.001
P	0.006	0.005	0.012	0.013	0.012	0.007
Ni	0.15	1.60	0.89	1.30	1.80	0.52
Cr	0.020	0.043	0.051	0.180	0.300	0.031
Mo	0.40	0.39	0.34	0.42	0.49	0.29
Cu	0.25	0.14	0.16	0.20	0.18	0.32
Al	0.008	0.005	0.007	0.005	0.005	0.031
Nb	0.009	0.007	0.008	0.008	0.008	0.030
V	0.004	0.004	0.005	0.005	0.006	0.004
Ti	0.008	0.015	0.029	0.028	0.022	0.008
O	0.044	0.042	0.045	0.040	0.032	-
N	0.0045	0.0047	0.0072	0.0051	0.0073	0.0025
CE_{IIW}	0.46	0.52	0.48	0.56	0.65	0.48
P_{CM}	0.22	0.21	0.24	0.25	0.28	0.20
CEN	0.32	0.31	0.36	0.37	0.44	0.29
B_s	623	583	612	576	533	608
M_s	457	445	444	436	418	458

Notes: B= <0.0005

$CE_{IIW} = C + Mn/6 + (Cr+Mo+V)/5 + (Ni + Cu)/15$

$P_{cm} = C + Si/30 + (Mn+Cu+Cr)/20 + Ni/60 + Mo/15 + V/10 + 5B$

$CEN=C+A(C)\ (Si/24+Mn/6+Cu/15+Ni/20+(Cr+Mo+Nb+V)/5+5B)$

$A(C)= 0.75 +0.25 \tanh\{(20\ (C-0.12)\}$

$B_s = 830-270(C)-90(Mn)-37(Ni)-70(Cr)-83(Mo)$

$M_s= 561-474(C)-33(Mn)-17(Ni)-17(Cr)-21(Mo)$

Table 2. Microhardness results for experimental welds deposited at energy inputs of 1.5 and 0.5 kJ/mm.

Weld ID	LA90			LA100			NiMo80			PT-01			PT-02		
	Mean HV	Range HV	STDEV HV	Mean HV	Range HV	STDEV HV	Mean HV	Range HV	STDEV HV	Mean HV	Range HV	STDEV HV	Mean HV	Range HV	STDEV HV
1.5kJ/mm-TT	251	240-267	6.7	267	251-289	9.8	274	259-282	5.8	291	281-305	7.0	338	328-356	7.1
1.5kJ/mm-CW	252	233-263	7.3	278	250-300	13.4	270	257-277	4.9	295	269-310	9.1	338	320-356	9.3
0.5kJ/mm-TT	289	263-357	21.8	297	255-328	21.2	332	305-352	17.2	335	309-370	16.8	382	322-416	24.7
0.5kJ/mm-CW	279	258-302	15.2	324	309-346	11.4	341	297-369	19.2	352	304-374	19.1	375	362-408	13.4

Notes: TT= Through-thickness at weld centerline, CW= Cross-weld using weld metal only

Table 3. Microhardness results for WM CCT samples.

Weld	LA90			LA100			NiMo80			PT-01			PT-02		
Cooling Time $\Delta t_{800\text{-}500}$, s	Mean HV	Range HV	STDEV HV	Mean HV	Range HV	STDEV HV	Mean HV	Range HV	STDEV HV	Mean HV	Range HV	STDEV HV	Mean HV	Range HV	STDEV HV
2	342	329-349	7.1	355	344-365	7.0	410	398-416	6.1	404	395-411	5.5	405	400-417	7.1
3.5	311	305-319	4.7	334	314-351	10.7	372	350-395	14.4	369	360-377	5.3	416	408-425	5.1
5	294	283-301	5.1	312	299-347	13.5	334	322-375	14.9	364	349-384	10.6	416	402-439	11.5
7.5	269	255-278	6.2	295	278-327	15.7	312	303-328	8.1	328	310-350	10.7	386	369-397	10.0
10	259	250-264	4.7	267	254-276	7.0	281	278-284	2.1	310	302-317	5.2	360	351-368	6.3
20	243	237-248	3.3	253	244-259	4.4	260	255-264	3.4	275	267-285	5.7	323	315-332	5.5
50	233	227-236	3.2	236	229-242	4.3	242	231-248	5.2	253	246-259	4.2	289	279-297	6.0

Table 4. Sub-size Charpy impact toughness of 1.5 kJ/mm deep-fill pass and thermally cycled WM samples with through-thickness notch orientation.

Specimen ID	2/3 Sub-size Charpy Impact Energy @ -20°C J	Fracture Appearance Shear Area %		Equivalent Full-Size Energy J
X100 Pipe Steel	157 (152, 160, 160)		100	235
LA90-WMC-AW	75 (76, 77, 71)		81	112
LA90-WMC-1300-5s	55, (57, 54, 55)		76	82
LA100-WMC-AW	42 (46, 42, 38)		68	63
LA100-WMC-1300-5s	32 (32, 32, 33)		71	48
NiMo80-WMC-AW	64 (67, 66, 58)		79	96
NiMo80-WMC-1300-5s	50 (49, 51, 50)		69	75
PT-01-WMC-AW	60 (59, 60, 60)		76	90
PT-01-WMC-1300-5s	42 (48, 38, 40)		74	63
PT-02-WMC-AW	41 (41, 41, 40)		74	62
PT-02-WMC-1300-5s	30 (28, 32,30)		61	45

Table 5. Full-size Charpy impact toughness of 1.5 kJ/mm deep-fill pass and thermally cycled WM samples with surface notch orientation from hot pass region.

Specimen ID	Full-size Charpy Impact Energy @ -20°C, J	Average Shear Area %
LA100-WMC-AW	72 (73, 80, 93)	57
LA100-WMC-1300-5s	65 (66, 66, 62)	60
LA100-WMC-1300-10s	103 (105, 101, 103)	81
LA100-WMC-1300-20s	141 (142, 140, 140)	90
NiMo80-WMC-AW	102 (100, 102, 104)	78
NiMo80-WMC-1300-5s	67 (72, 56, 73)	80
NiMo80-WMC-1300-10s	116 (116, 171*, 160*)	88
NiMo80-WMC-1300-20s	164 (161, 170, 160)	96
PT-01-WMC-AW	90 (88, 90, 93)	79
PT-01-WMC-1300-5s	63 (63, 64, 62)	72
PT-01-WMC-1300-10s	112 (110, 113, 112)	85
PT-01-WMC-1300-20s	156 (150, 160, 159)	90

Note: * The fracture path deviated toward the fusion line where a weld defect was found; therefore these are not considered valid tests.

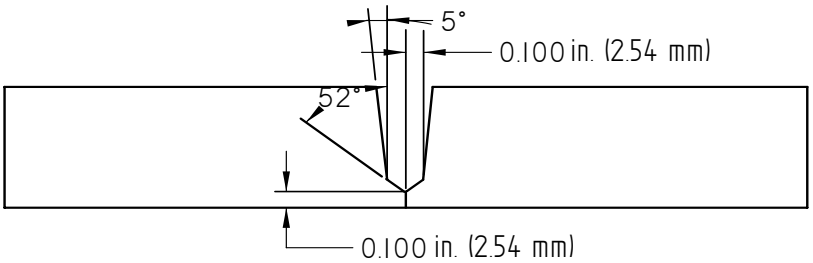

(a) Narrow-gap joint design preparation.

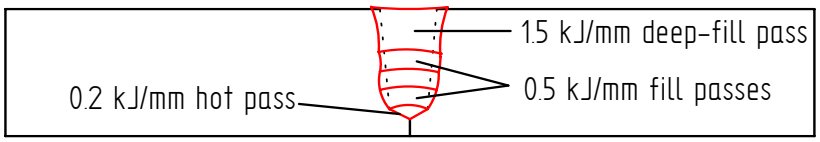

(b) Experimental weld pass sequence.

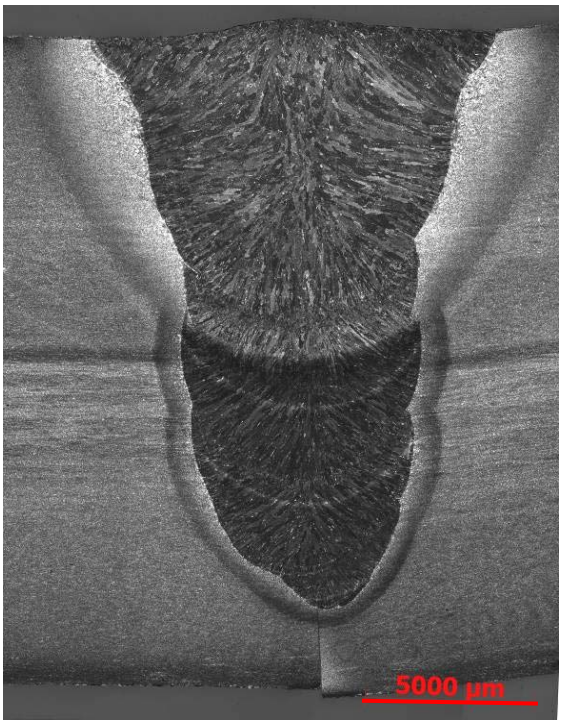

(c) Representative macrograph of experimental weld (LA90).

Figure 1. Schematic diagrams and macrograph for experimental welds.

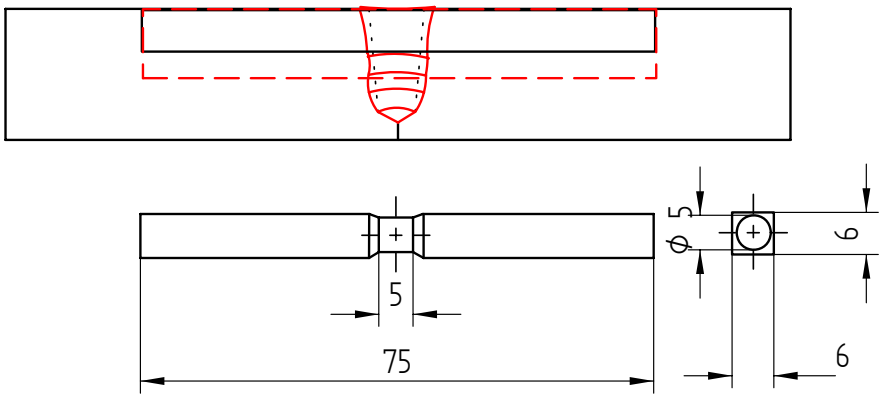

Figure 2. Shematic diagram showing location of WM dilatometric 6 x 6 mm and full-sized 10 x 10 mm specimen blanks (top) along with detail of rounded dilatometric specimen used for CCT experiments (bottom).

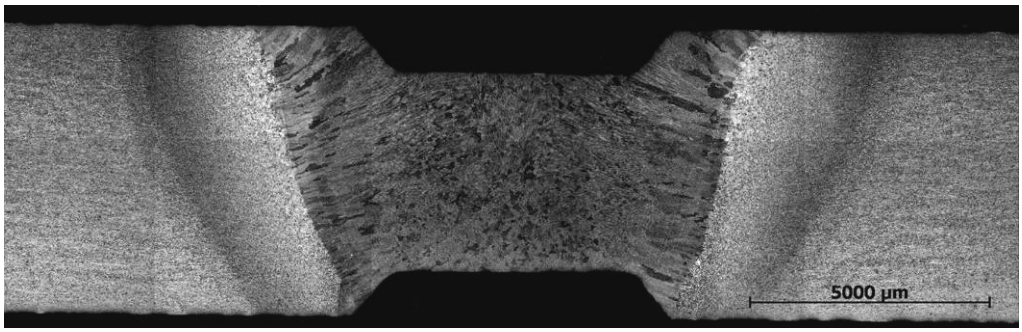

Figure 3. Representative macrograph of a WM dilatometric specimen cut longitudinally (parallel to the specimen length along the mid-plane) to reveal the through-thickness weld metal after thermal cycling.

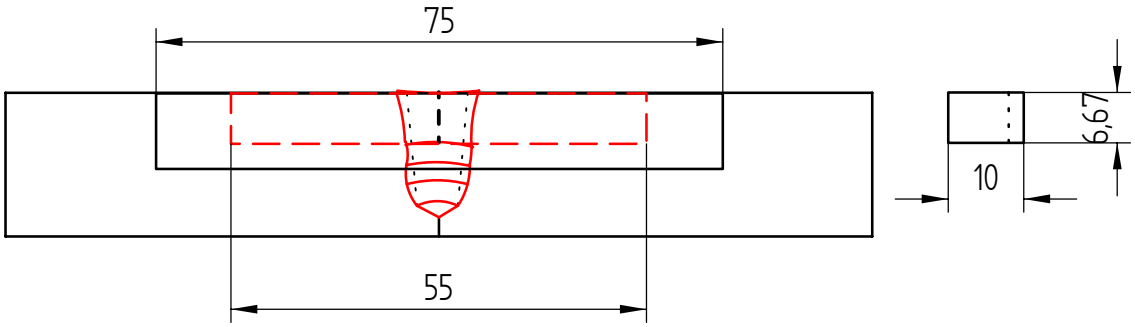

(a) 2/3 sub-sized Charpy impact specimen with through-thickness notch orientation.

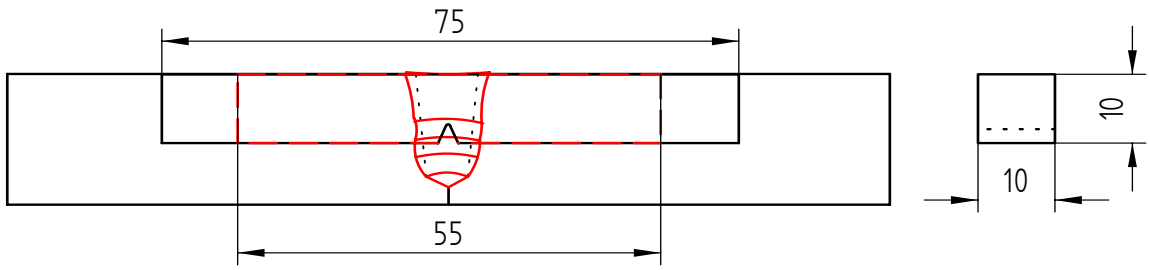

(b) Full-sized Charpy impact specimen showing surface notch from bottom fill passes.

Figure 4. Location and orientation of specimens used for sub-sized and full-sized WM Charpy impact toughness testing.

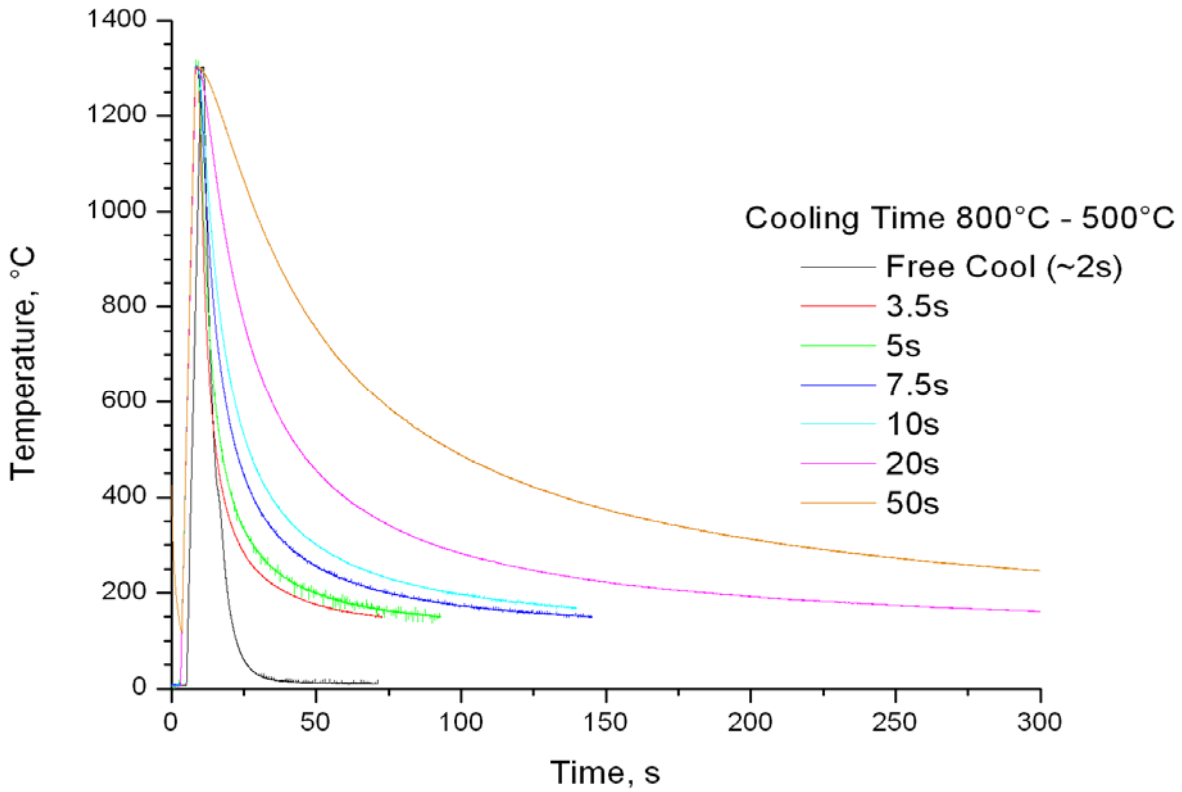

Figure 5. Thermal cycles (temperature versus time) for CCT simulation experiments with cooling times, $\Delta t_{800\text{-}500}$ = ~2, 3.5, 5, 7.5, 10, 20 and 50 s.

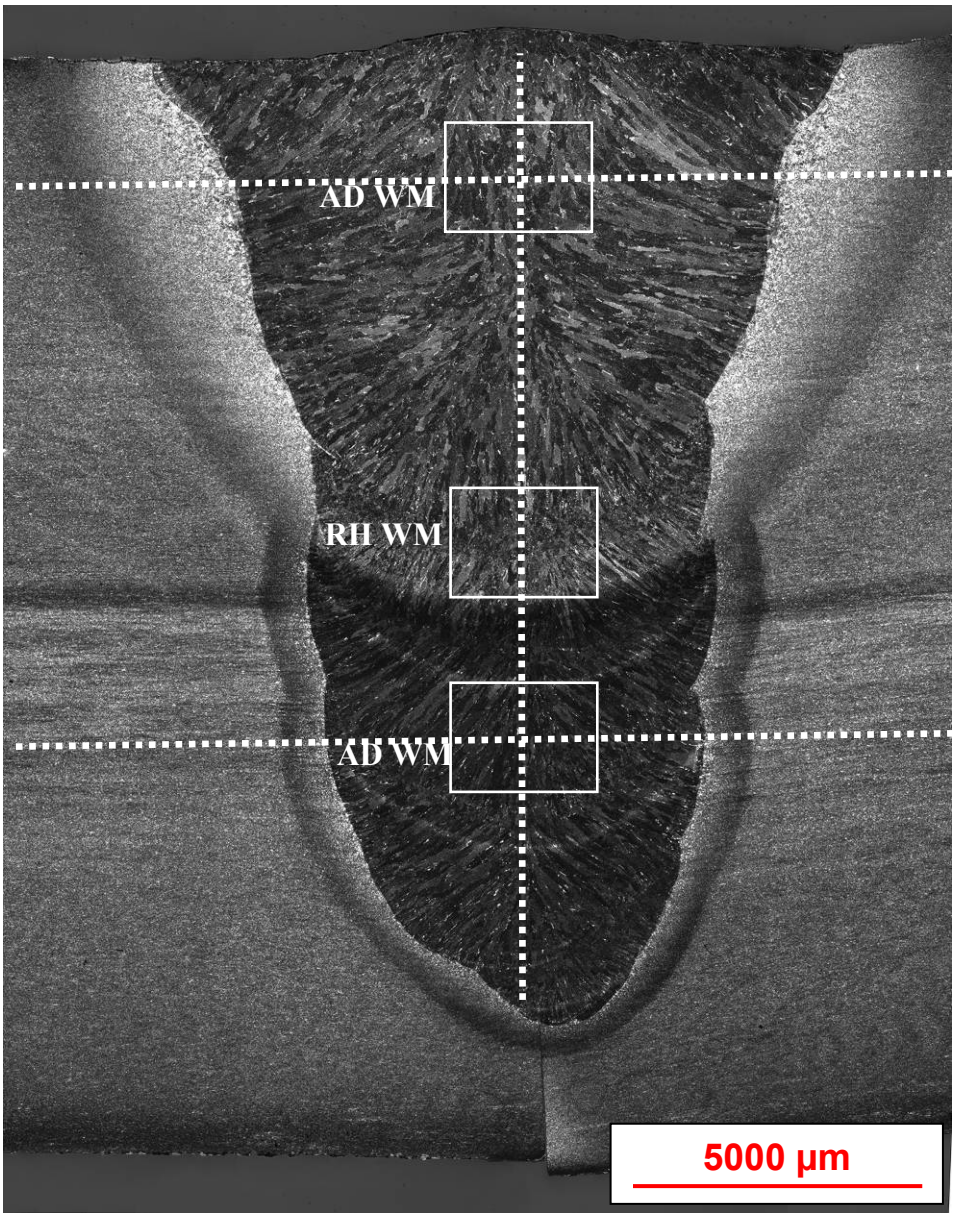

Figure 6. Macrograph of experimental weld showing areas (rectangular boxes) used for characterization of as-deposited and reheated WM microstructures. The vertical and horizontal dashed lines indicate the relative positions for the through-thickness and cross-weld microhardness surveys.

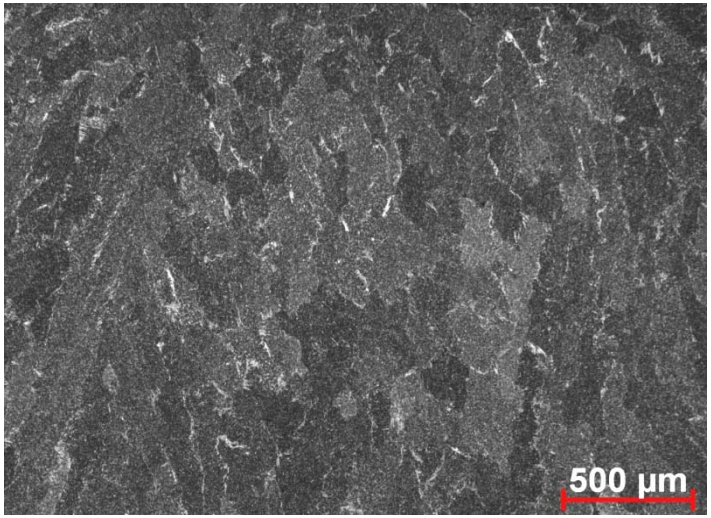

(a) LA 90–AD weld metal structure for 1.5 kJ/mm region.

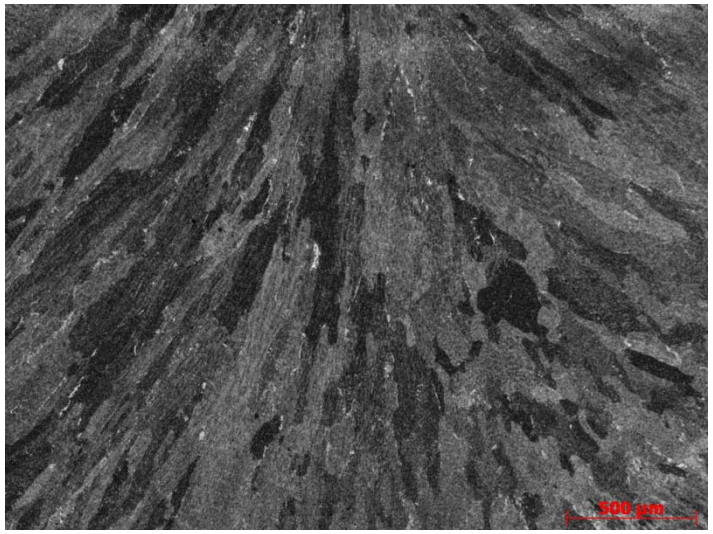

(c) LA 90 –AD weld metal structure for 0.5 kJ/mm region

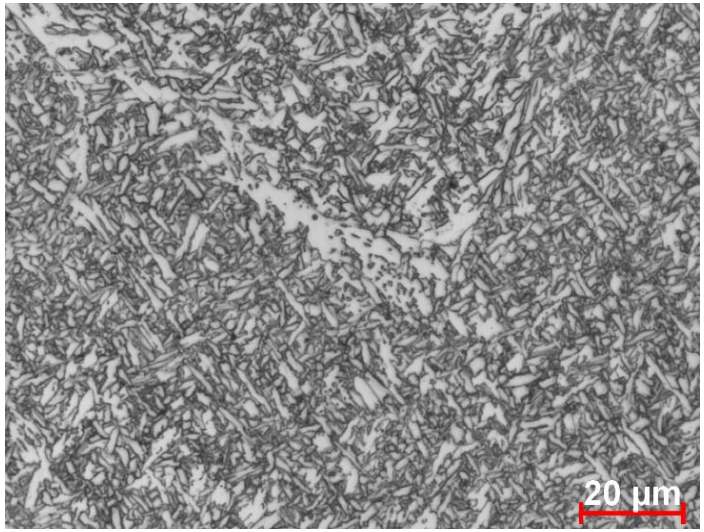

(b) Detail of AD weld metal microstructure in (a)

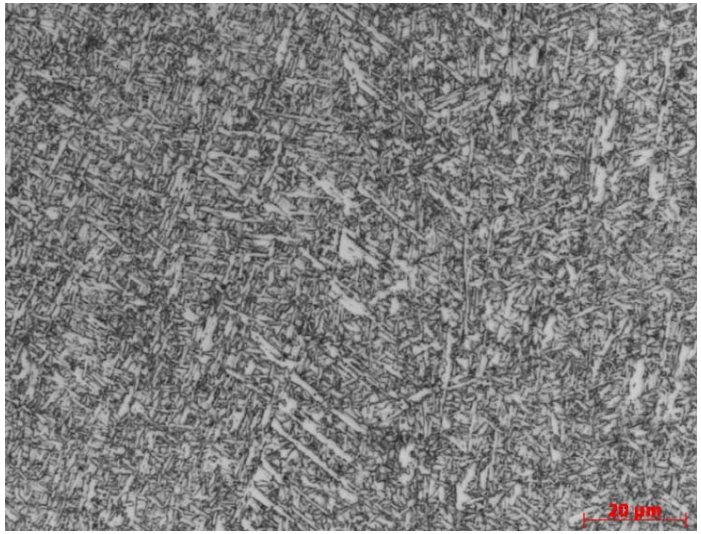

(d) LA 90 – Detail of AD weld metal microstructure in (c)

Figure 7. Micrographs of as-deposited weld metal of experimental weld LA90.

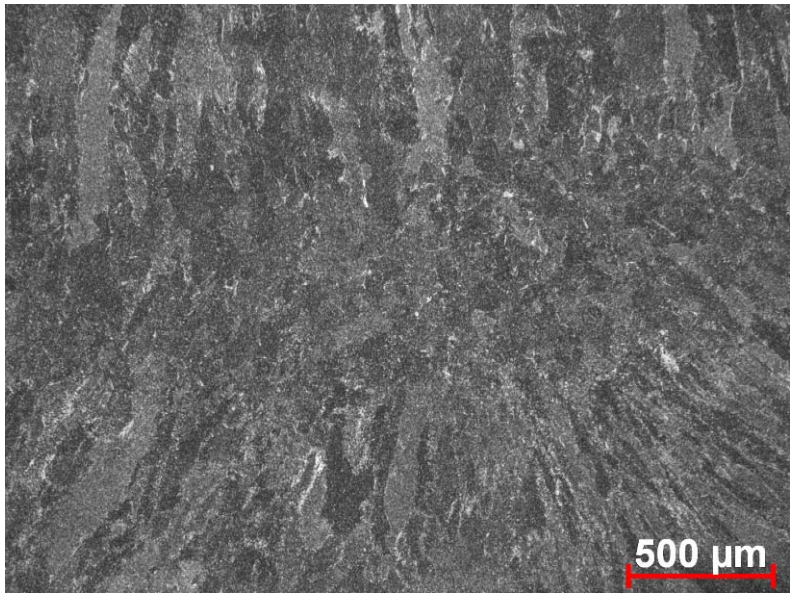

(a) Reheated structure formed under 1.5 kJ/mm weld pass

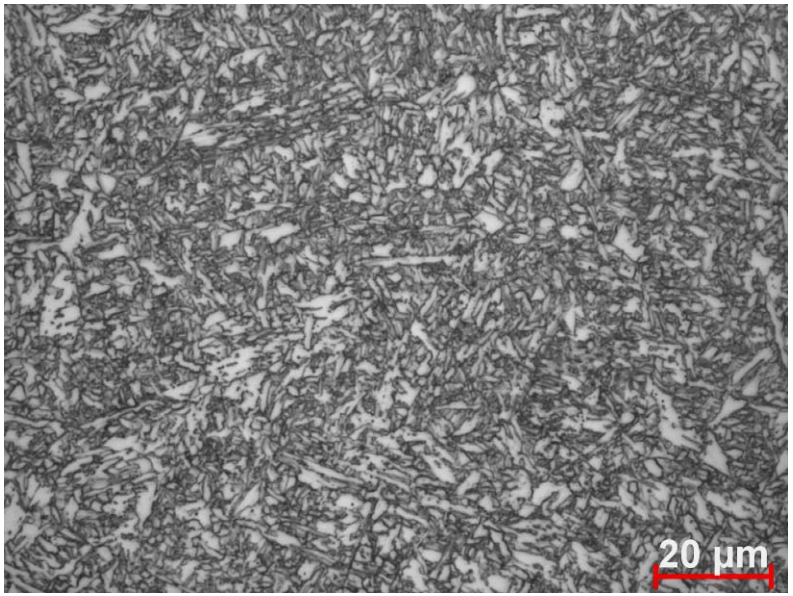

(b) Detail of reheated WM.

Figure 8. Micrographs of reheated WM of experimental weld LA90.

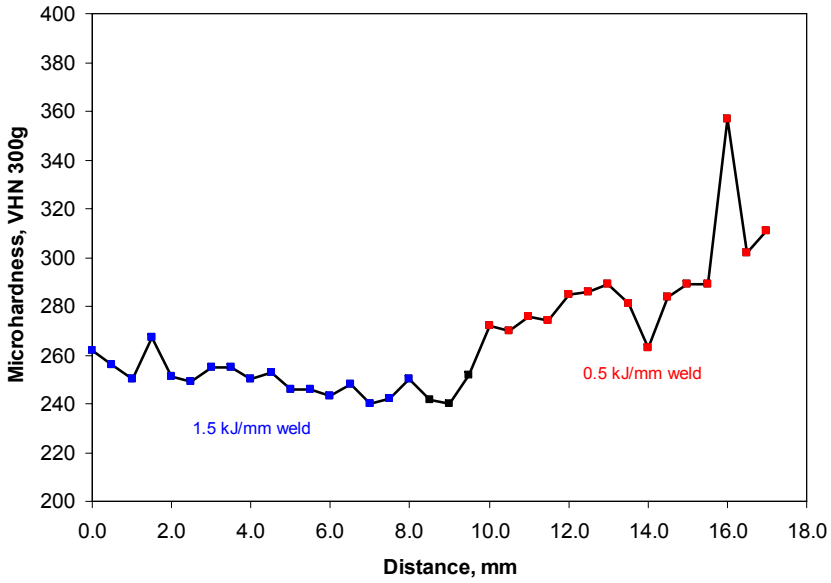

(a) Through-thickness weld centerline

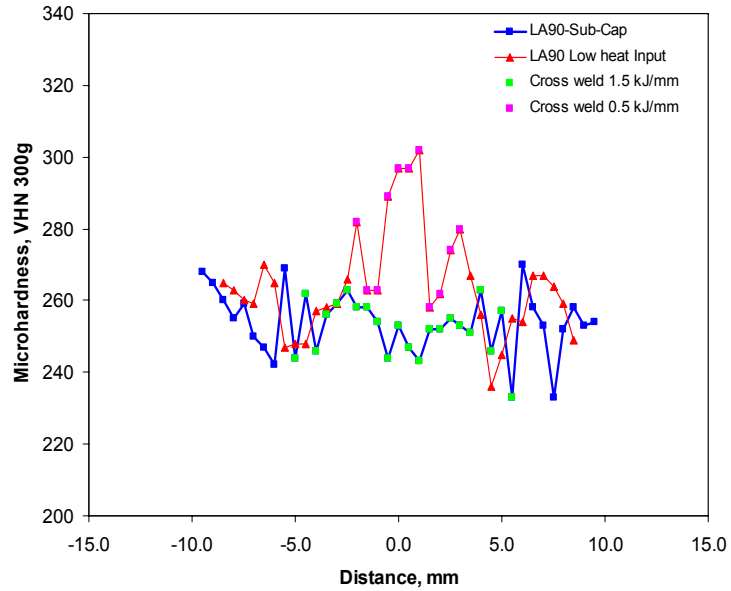

(b) Cross weld through 1.5 and 0.5 kJ/mm weld passes.

Figure 9. Microhardness results for LA90 weld.

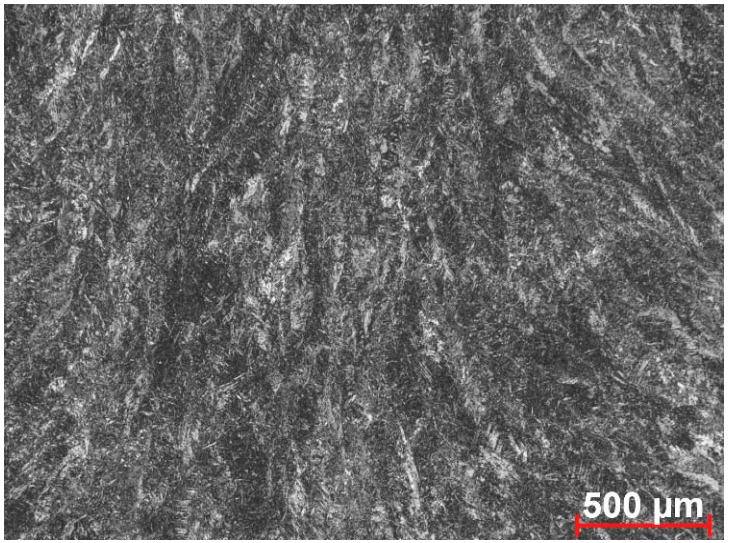

(a) LA 100–AD WM structure for 1.5 kJ/mm region.

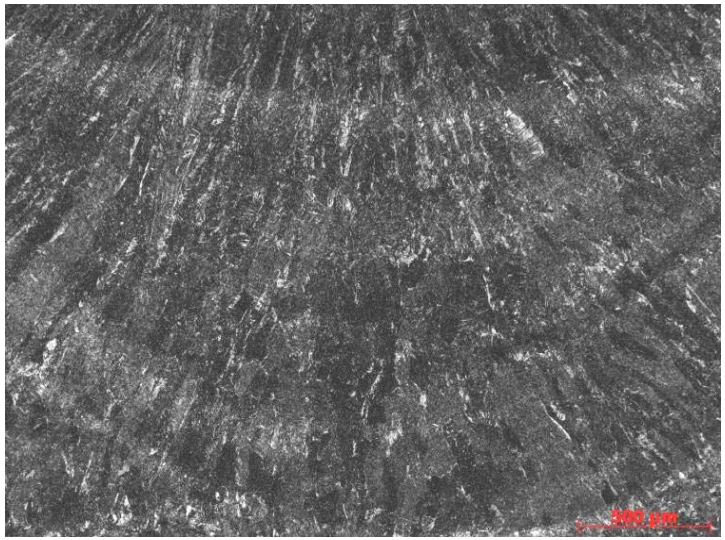

(c) LA100 –AD weld metal structure for 0.5 kJ/mm region

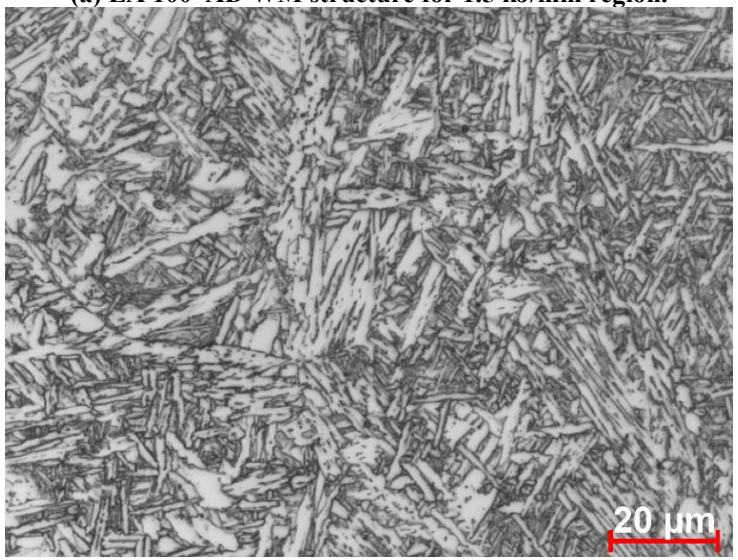

(b) LA 100 –AD weld metal microstructure; area 1

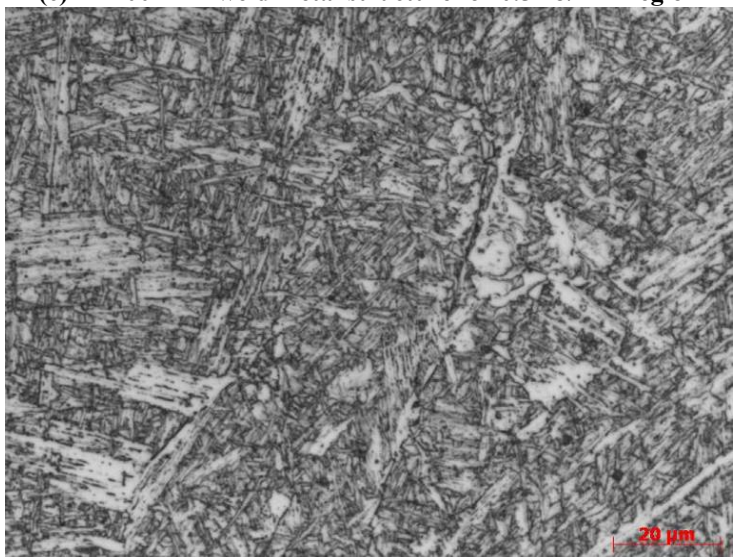

(d) LA 100 – Detail of AD weld metal microstructure in (c)

Figure 10. Micrographs of as-deposited weld metal of experimental weld LA100.

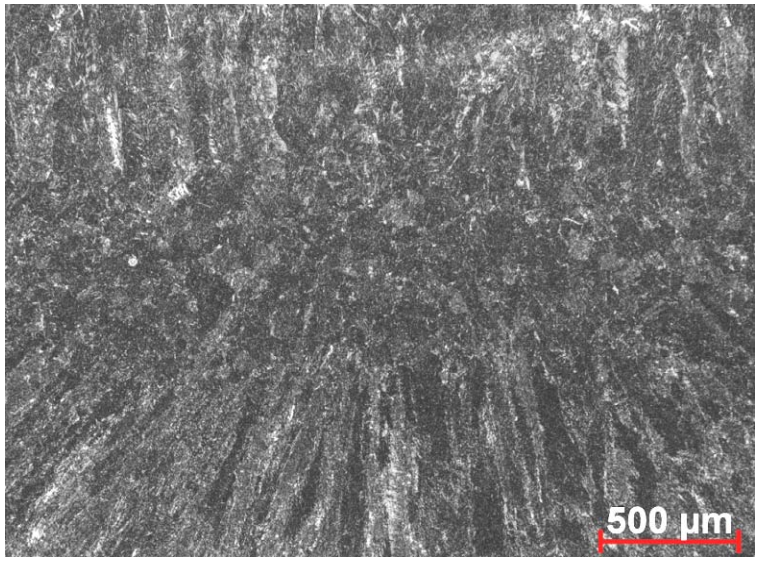

(a) Reheated structure formed under 1.5 kJ/mm weld pass

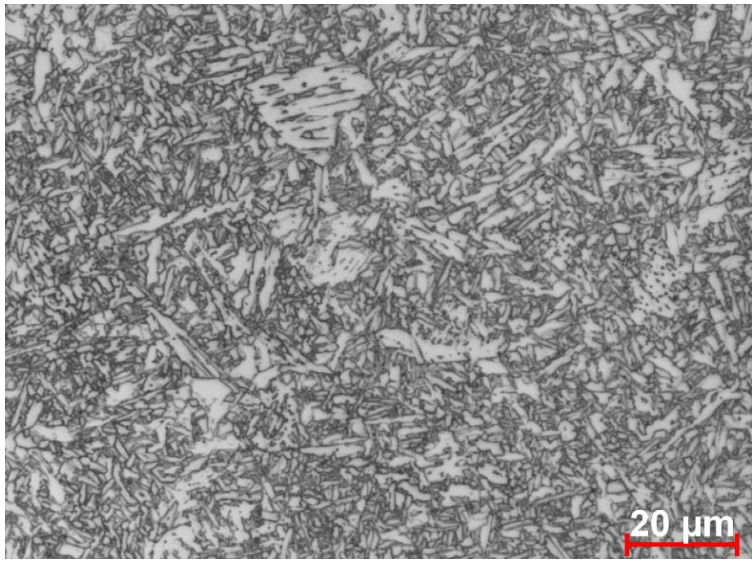

(b) Detail of reheated WM.

Figure 11. Micrographs of reheated WM of experimental weld LA100.

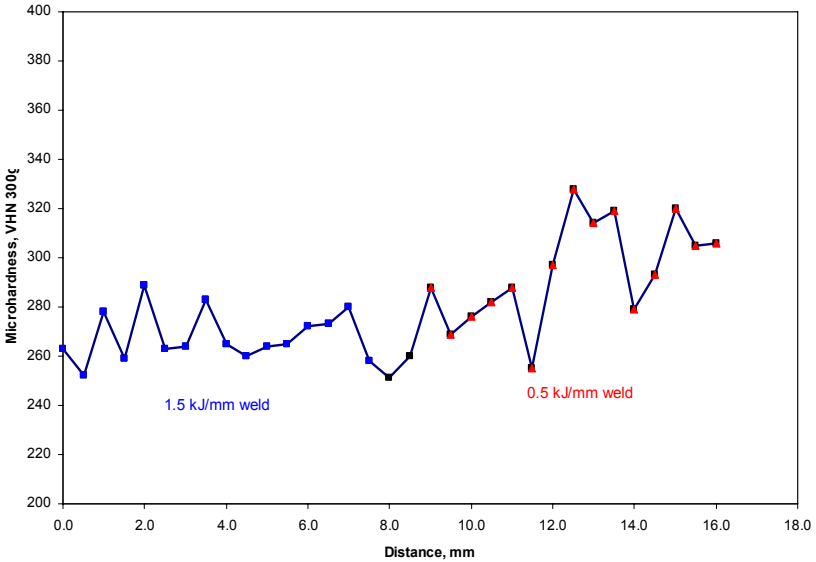

(a)

Through-thickness weld centerline

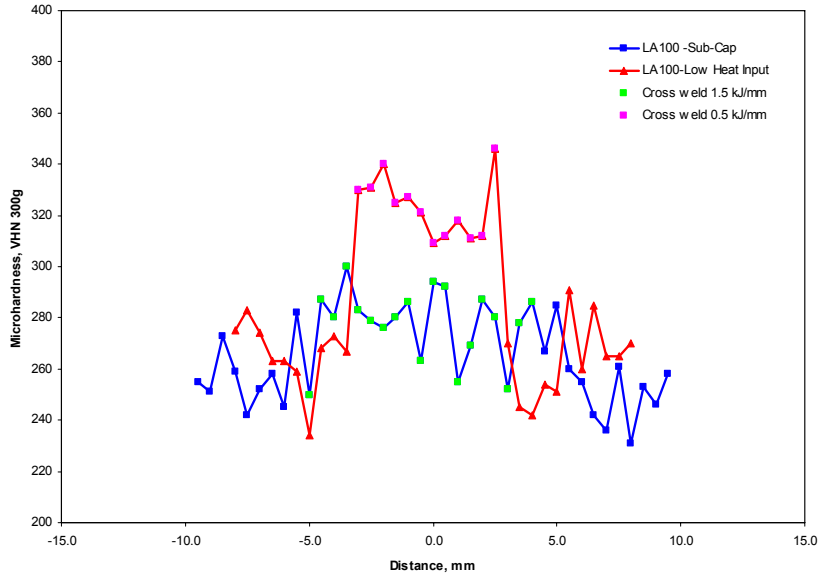

(b) Cross-weld through 1.5 and 0.5 kJ/mm weld passes.

Figure 12. Microhardness results for weld LA100.

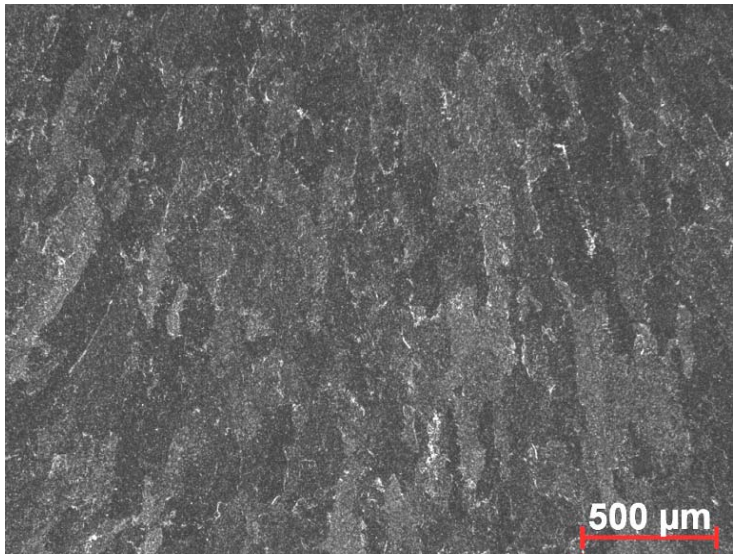

(a) NiMo80–AD WM structure for 1.5 kJ/mm region.

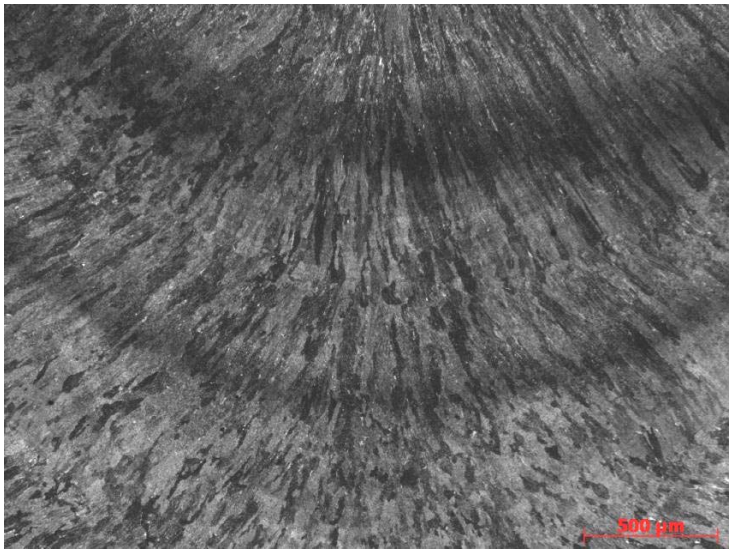

(c) NiMo80 –AD weld metal structure for 0.5 kJ/mm region

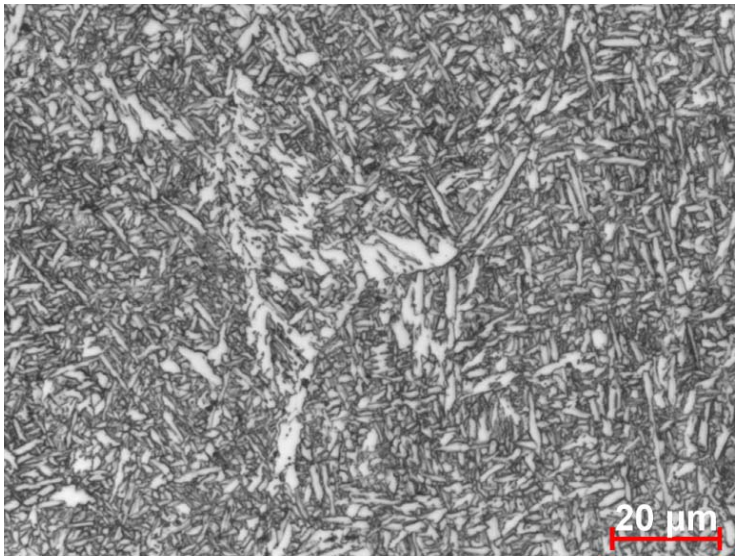

(b) NiMo80 –Detail of AD weld metal microstructure in (a)

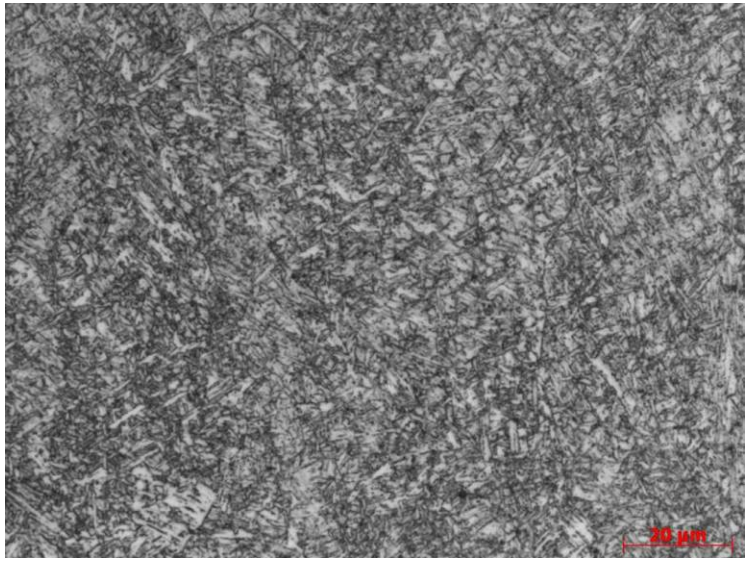

(d) NiMo80 – Detail of AD weld metal microstructure in (c)

Figure 13. Micrographs of as-deposited weld metal of experimental weld, NiMo80.

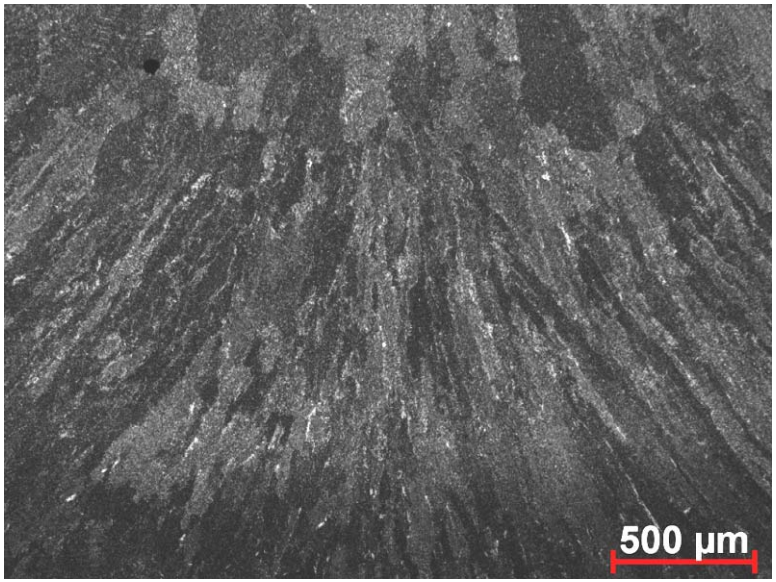

(a) Reheated structure formed under 1.5 kJ/mm weld pass

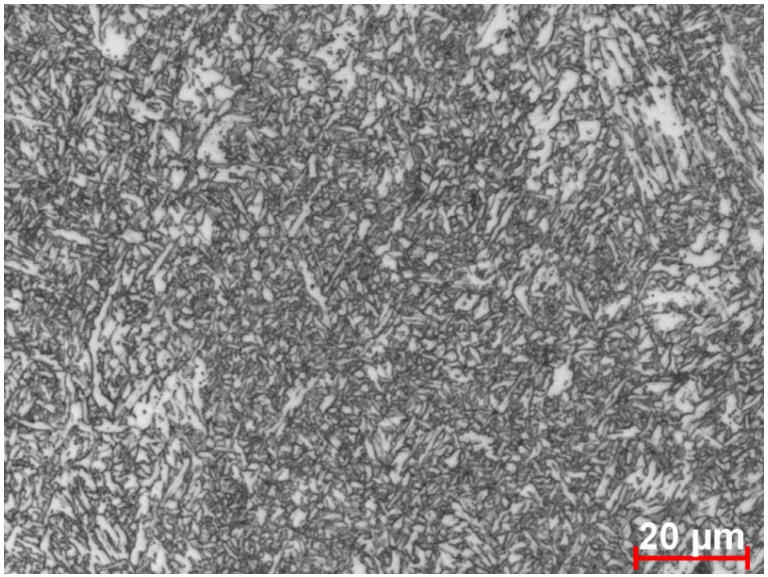

(b) Detail of reheated WM.

Figure 14. Micrographs of reheated WM of experimental weld NiMo80.

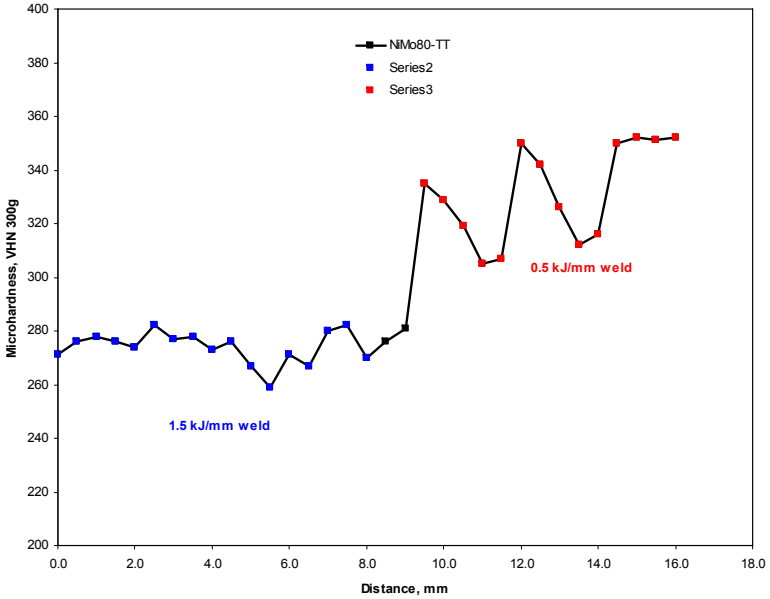

(a) Through-thickness weld centerline

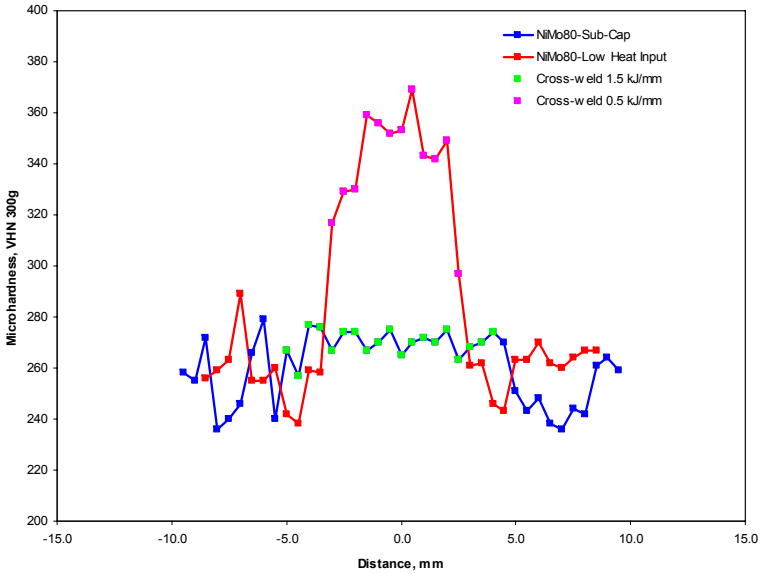

(b) Cross-weld through 1.5 and 0.5 kJ/mm weld passes.

Figure 15. Microhardness results for weld NiMo80.

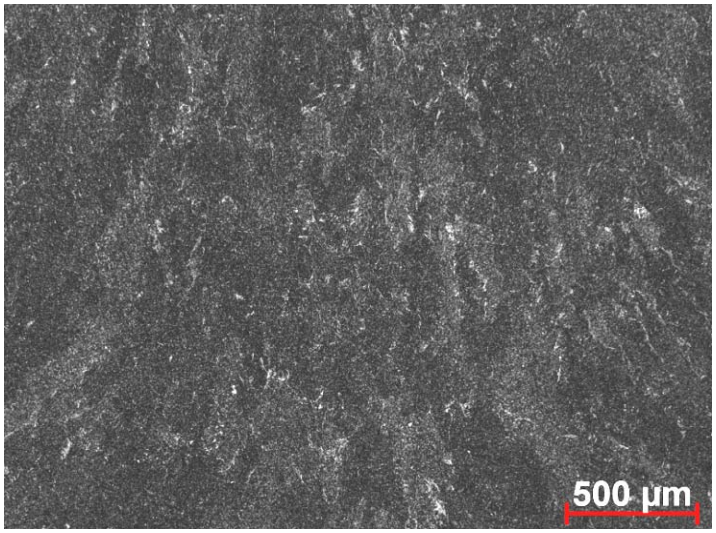

(a) PT-01–AD WM structure for 1.5 kJ/mm region.

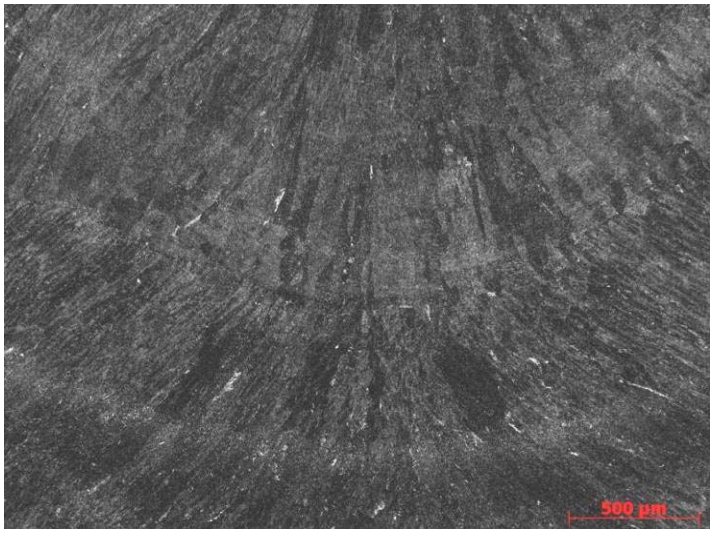

(c) PT-01 –AD weld metal structure for 0.5 kJ/mm region

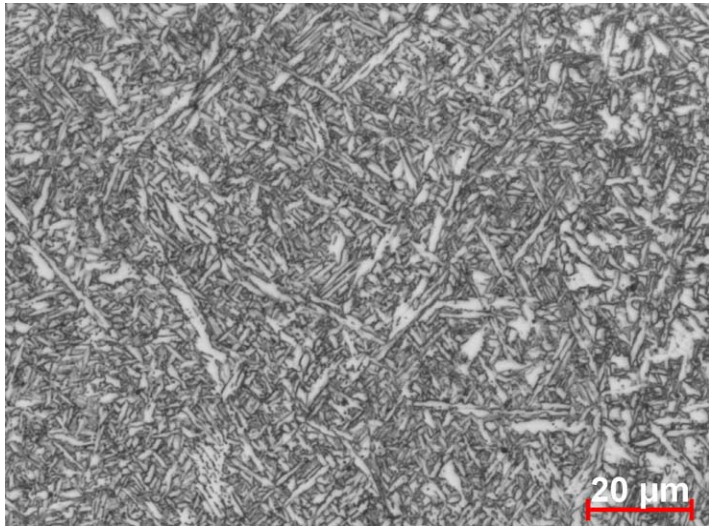

(b) PT-01 –Detail of AD weld metal microstructure in (a)

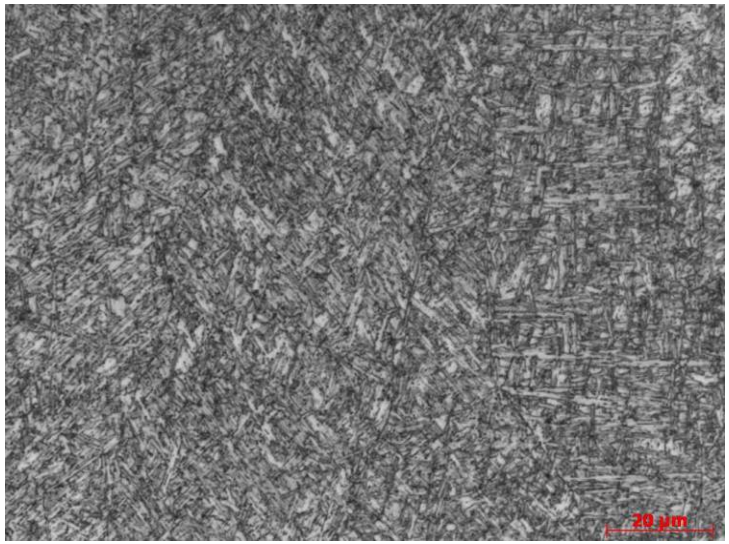

(d) PT-01 – Detail of AD weld metal microstructure in (c)

Figure 16. Micrographs of as-deposited weld metal of experimental weld PT-01.

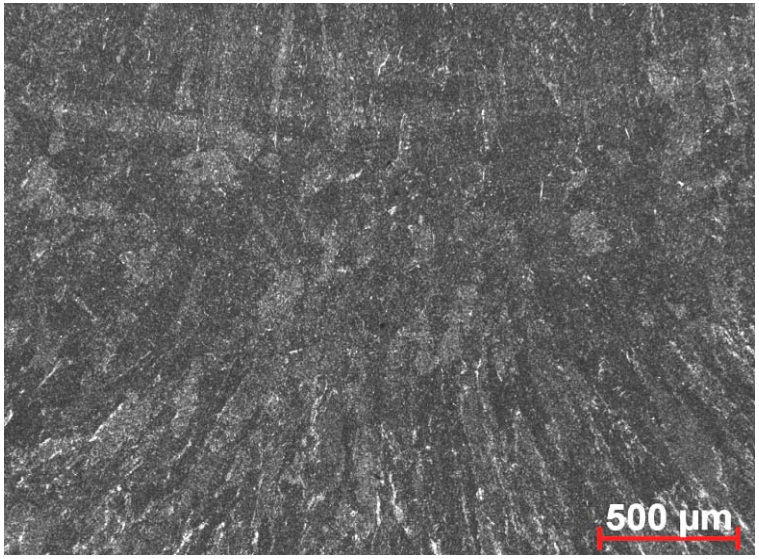

(a) Reheated structure formed under 1.5 kJ/mm weld pass

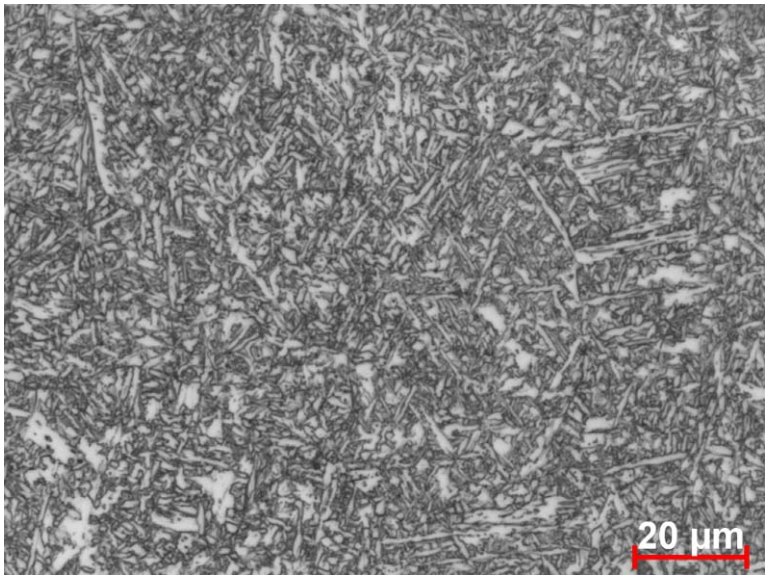

(b) Detail of reheated WM.

Figure 17. Micrographs of reheated WM of experimental weld PT-01.

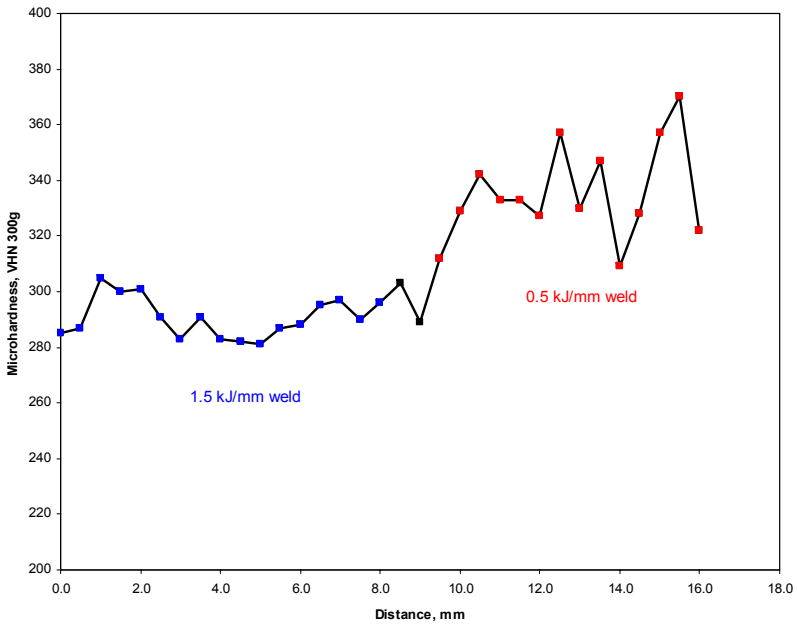

(a) Through-thickness weld centerline

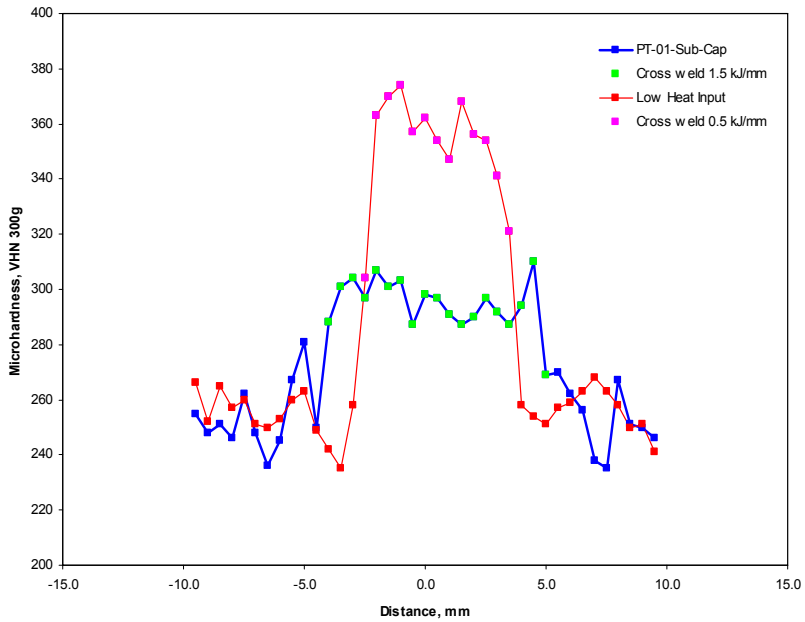

(b) Cross-weld through 1.5 and 0.5 kJ/mm weld passes.

Figure 18. Microhardness results for weld PT-01.

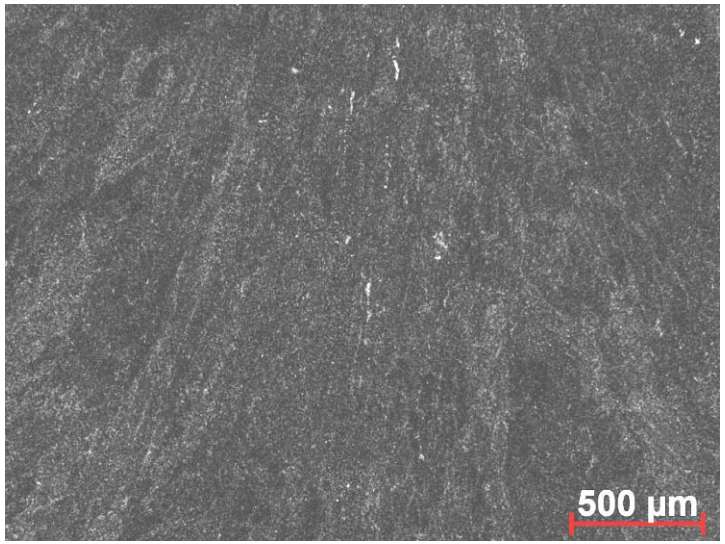

(a) PT-02–AD WM structure for 1.5 kJ/mm region.

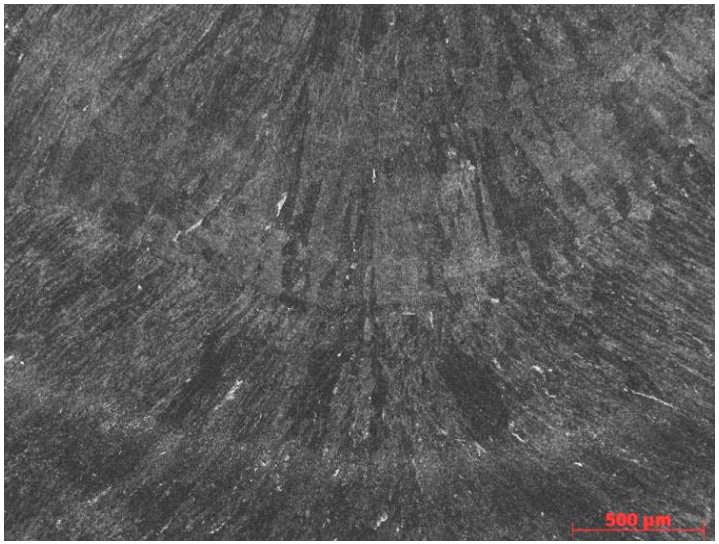

(c)PT-02 –AD weld metal structure for 0.5 kJ/mm region

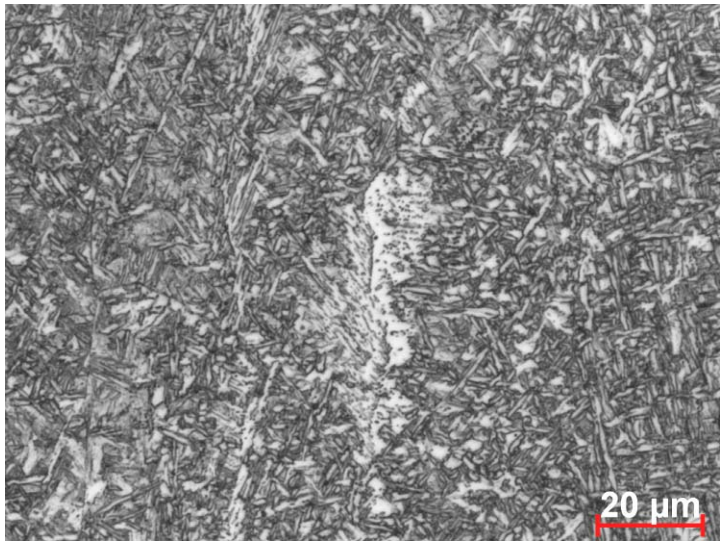

(b) PT-02 –Detail of AD weld metal microstructure in (a)

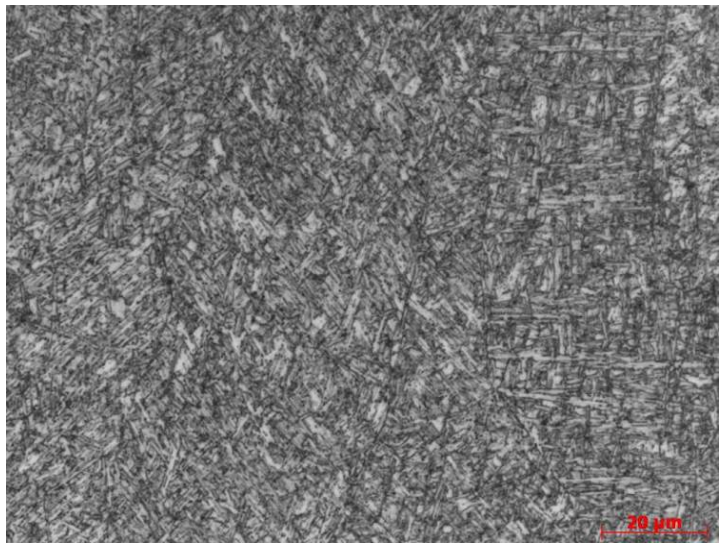

(d) PT-02 – Detail of AD weld metal microstructure in (c)

Figure 19. Micrographs of as-deposited weld metal of experimental weld PT-02.

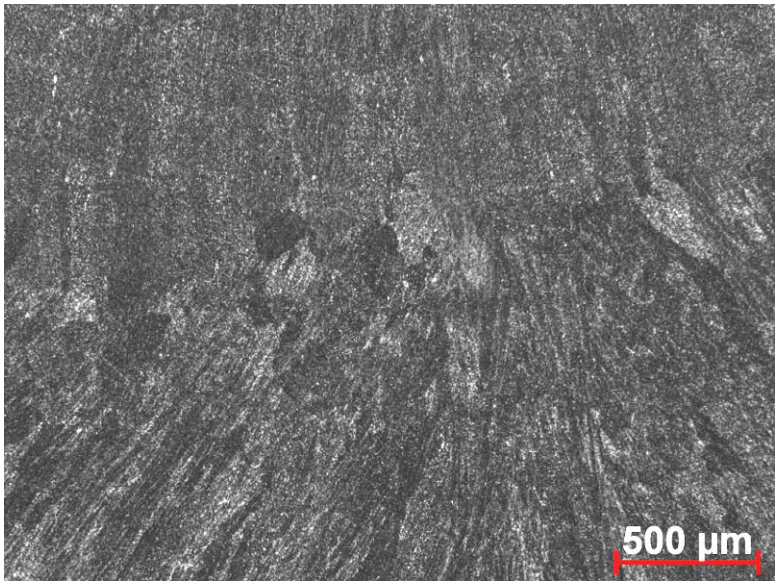

(a) Reheated structure formed under 1.5 kJ/mm weld pass

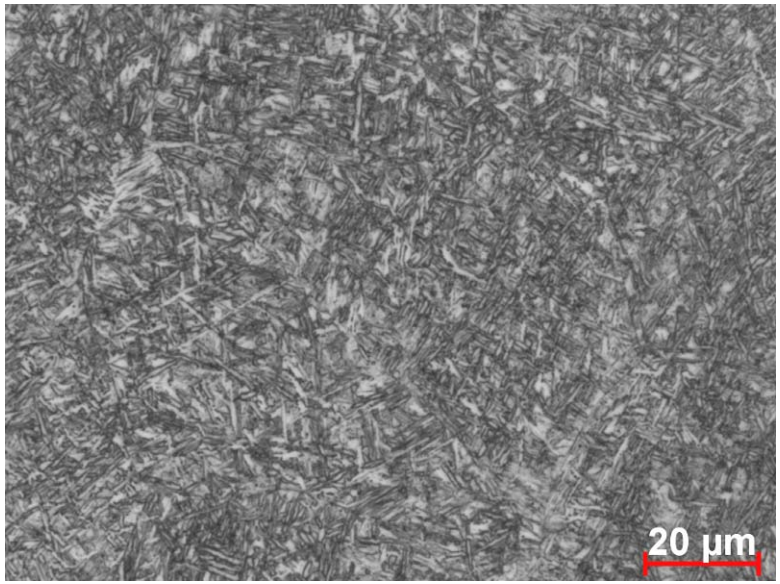

(b) Detail of reheated WM.

Figure 20. Micrographs of reheated WM of experimental weld PT-02.

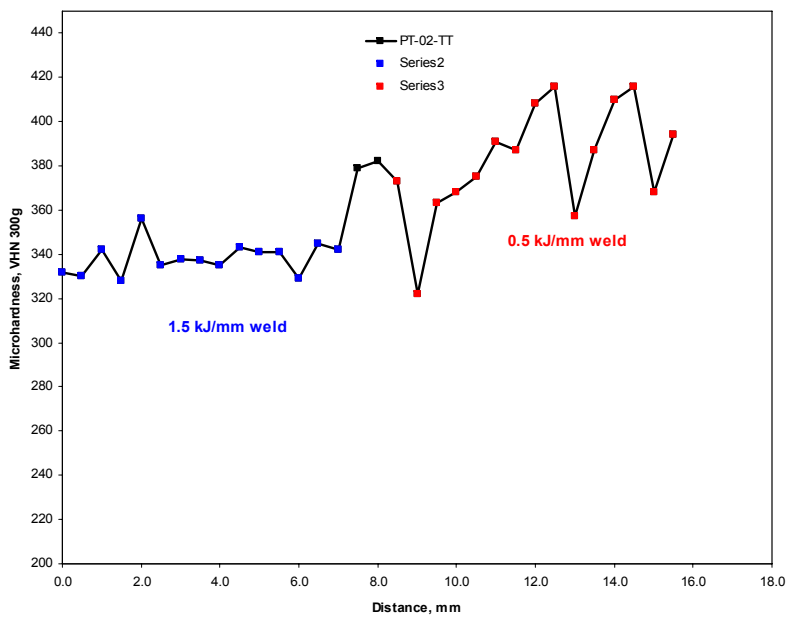

(a) Through-thickness weld centerline

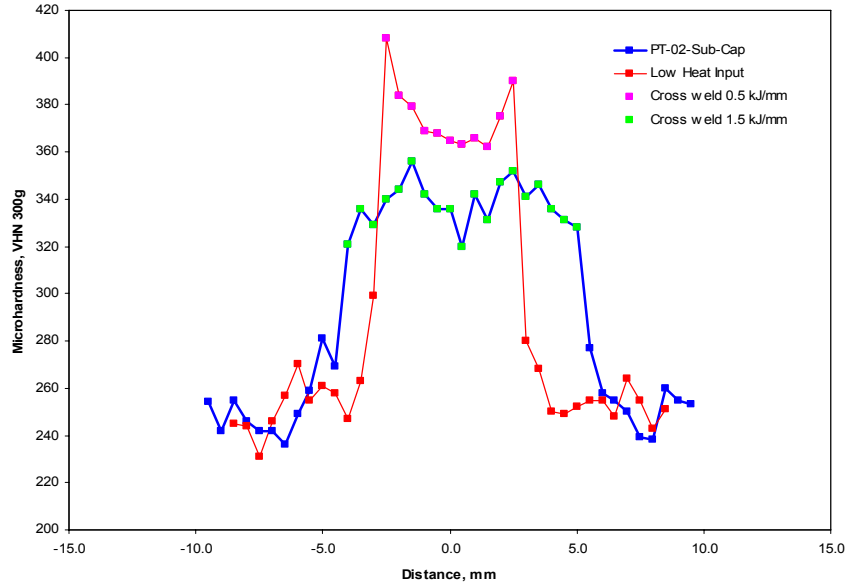

(b) Cross-weld through 1.5 and 0.5 kJ/mm weld passes.

Figure 21. Microhardness surveys of experimental weld PT-02.

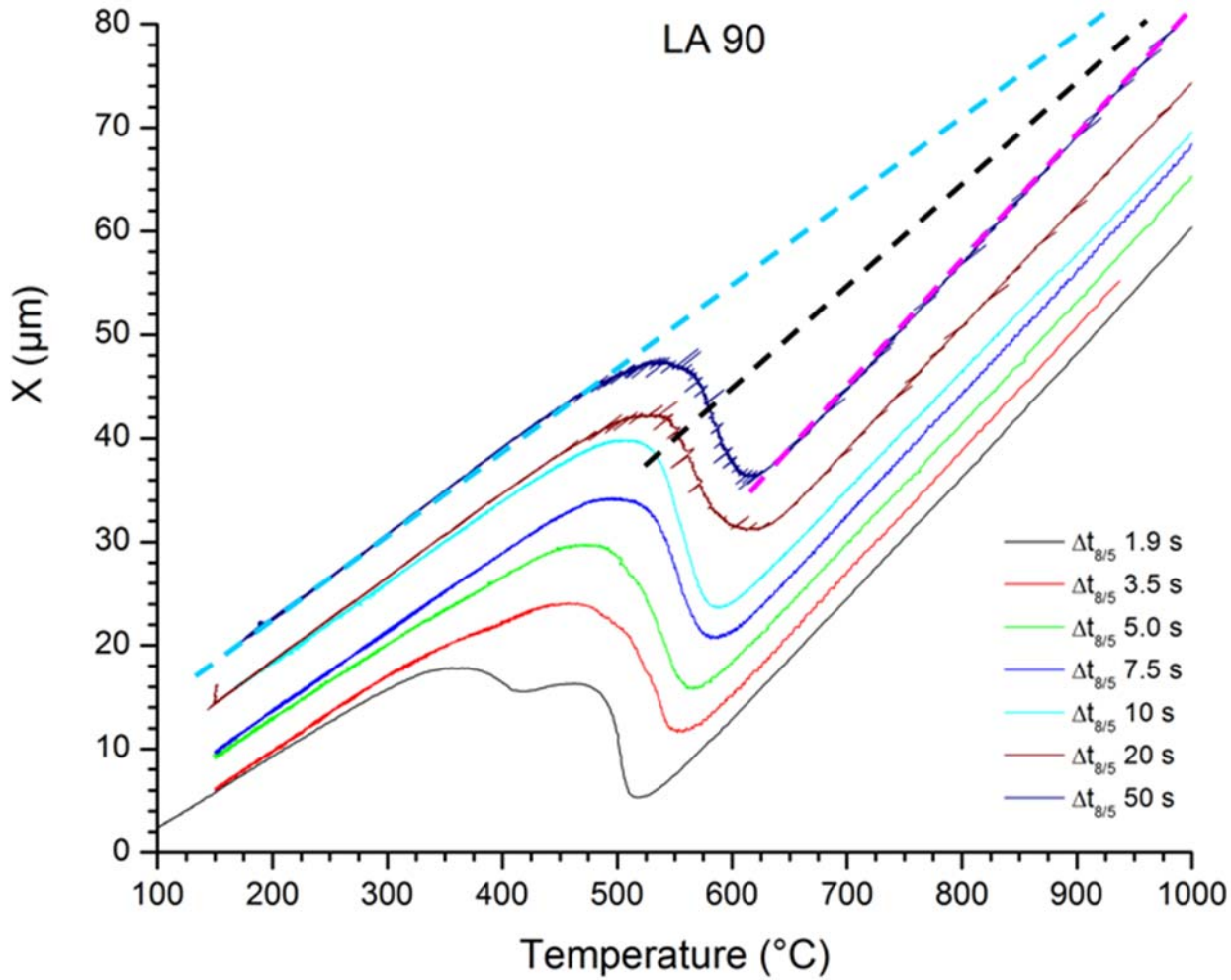

Figure 22. Dialation curves for LA90 WM as a function of cooling times Δt800-500 = 2, 3.5, 5, 7.5, 10, 20 and 50 s. The dashed lines represent the linear contractions (pink for FCC and light blue for BCC) used to establish the transformation temperatures, while the black dashed line represents the fraction transformed.

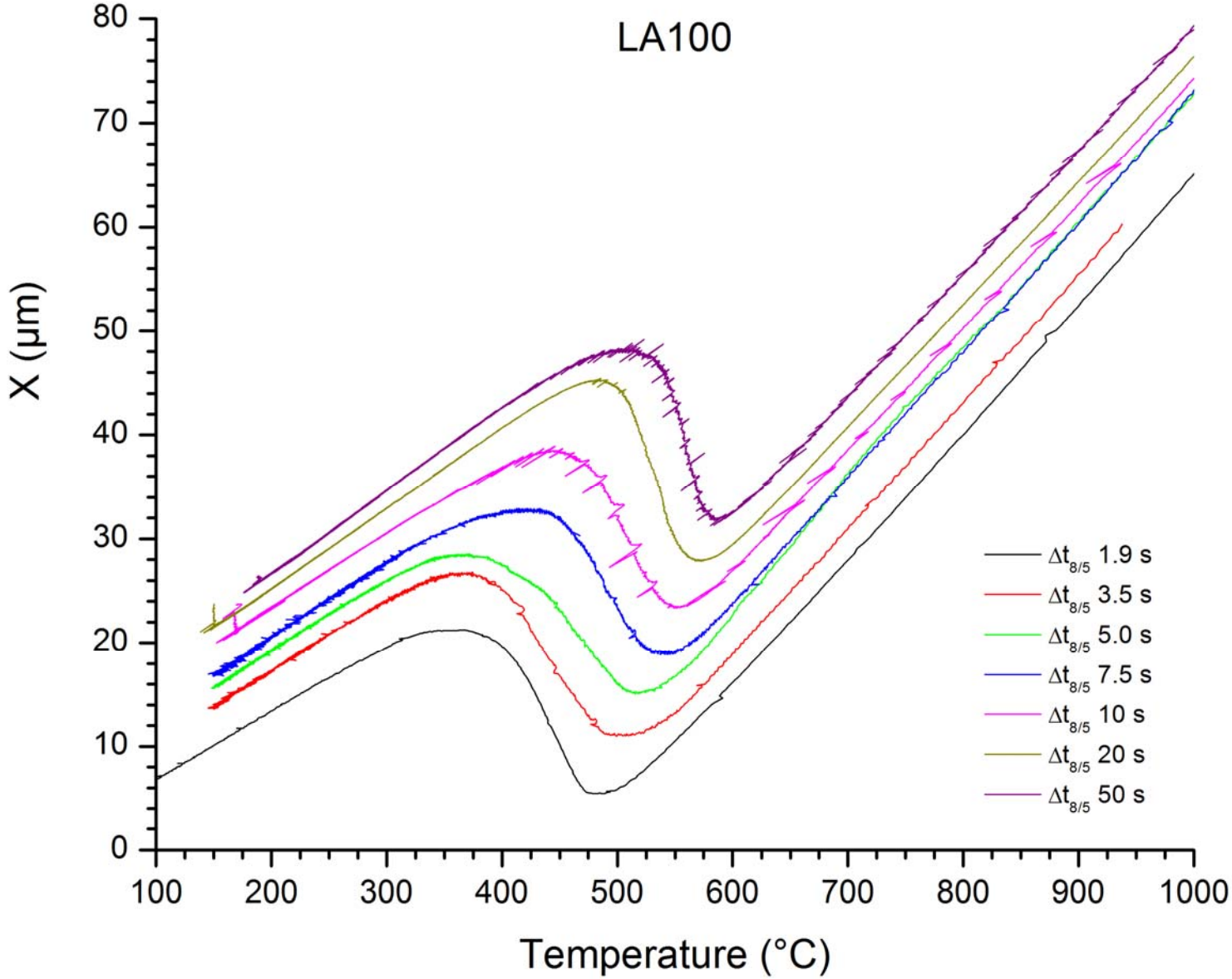

Figure 23. Dilatation curves for LA100 WM as a function of cooling times $\Delta t_{800\text{-}500}$ = 2, 3.5, 5, 7.5, 10, 20 and 50 s.

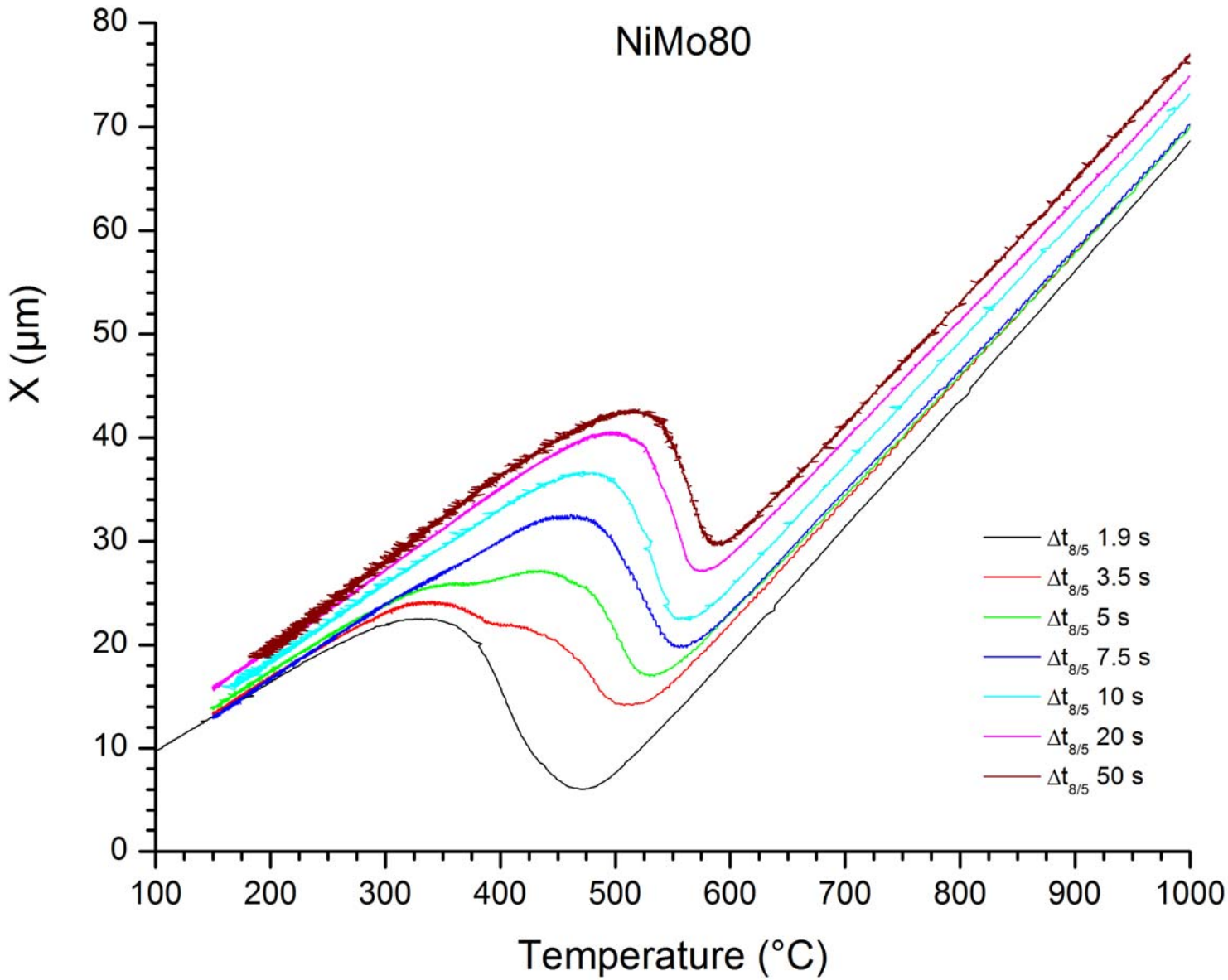

Figure 24. Dilatation curves for NiMo80 WM as a function of cooling times $\Delta t_{800\text{-}500}$ = 2, 3.5, 5, 7.5, 10, 20 and 50 s.

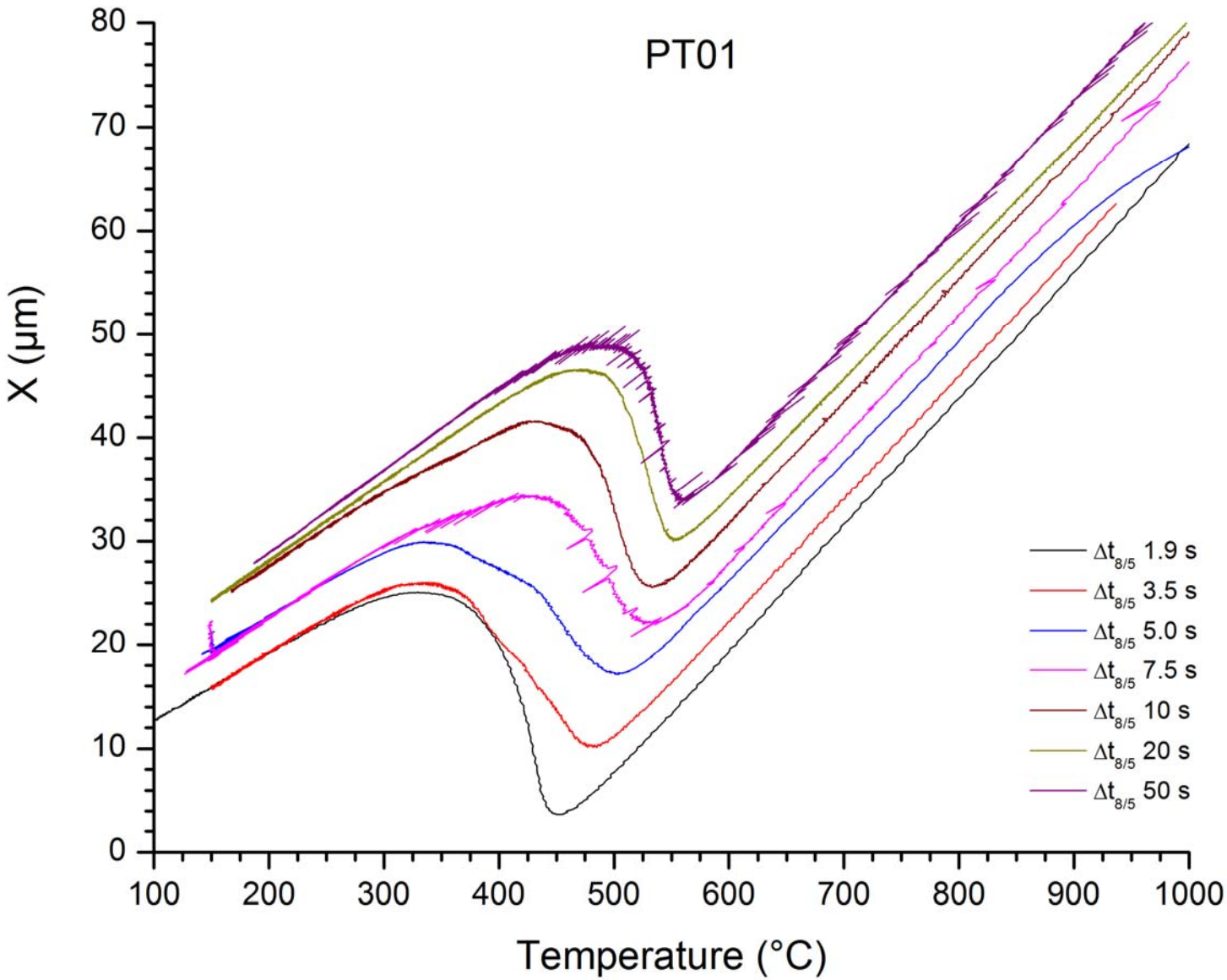

Figure 25. Dilatation curves for PT-01 WM as a function of cooling times $\Delta t_{800\text{-}500}$ = 2, 3.5, 5, 7.5, 10, 20 and 50 s.

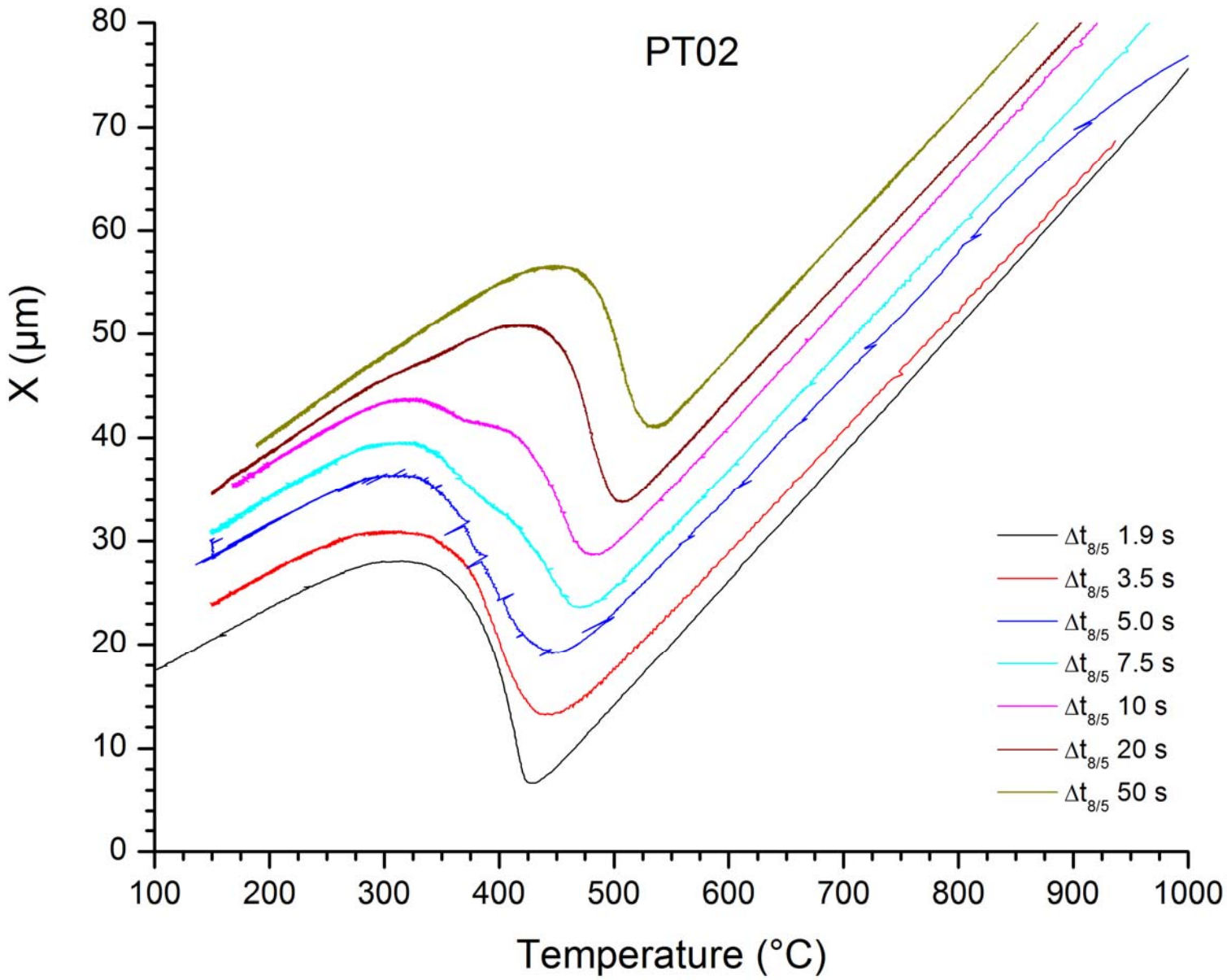

Figure 26. Dilatation curves for PT-02 WM as a function of cooling times $\Delta t_{800\text{-}500}$ = 2, 3.5, 5, 7.5, 10, 20 and 50 s.

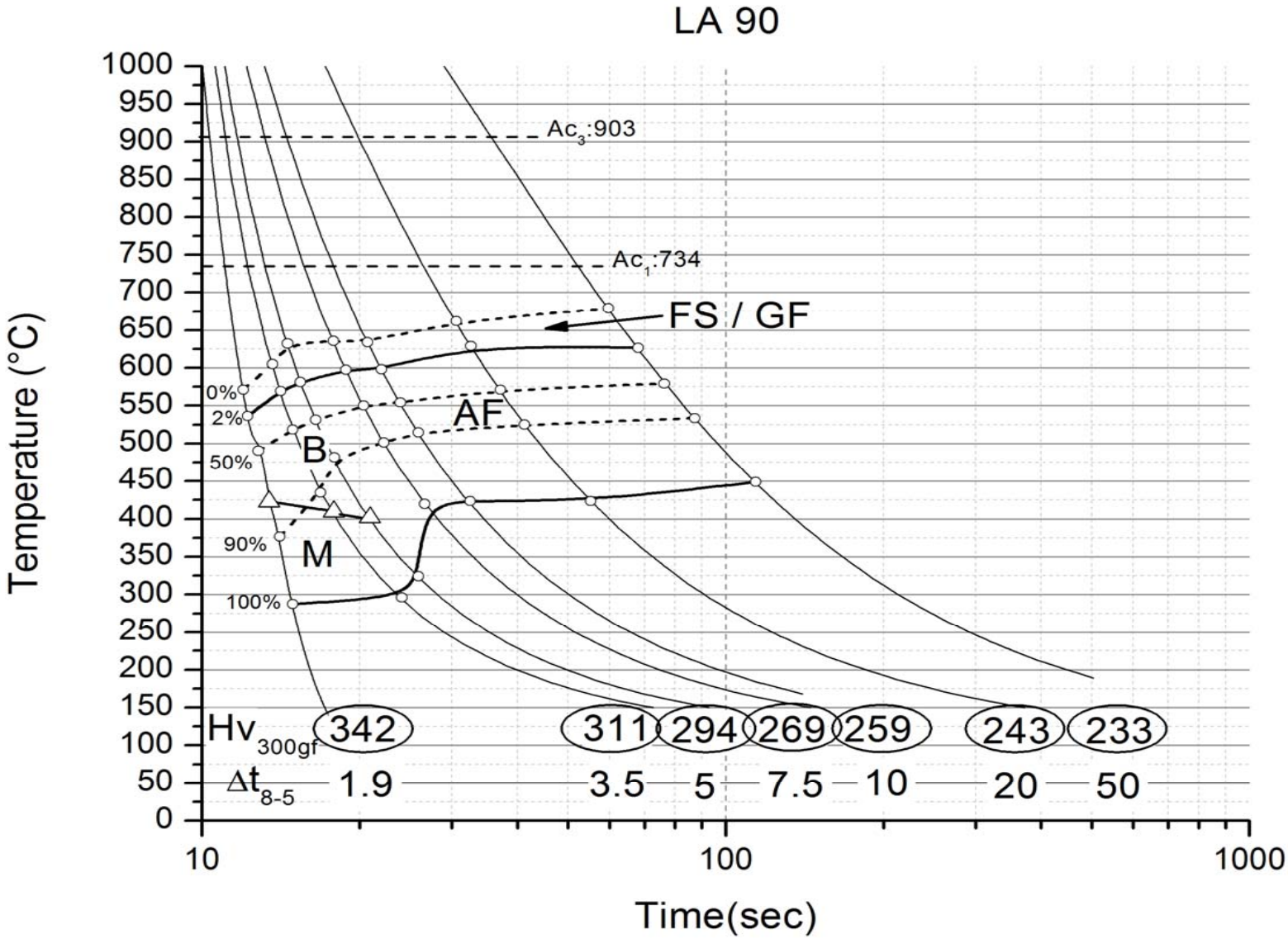

Figure 27. CCT diagram for weld LA 90.

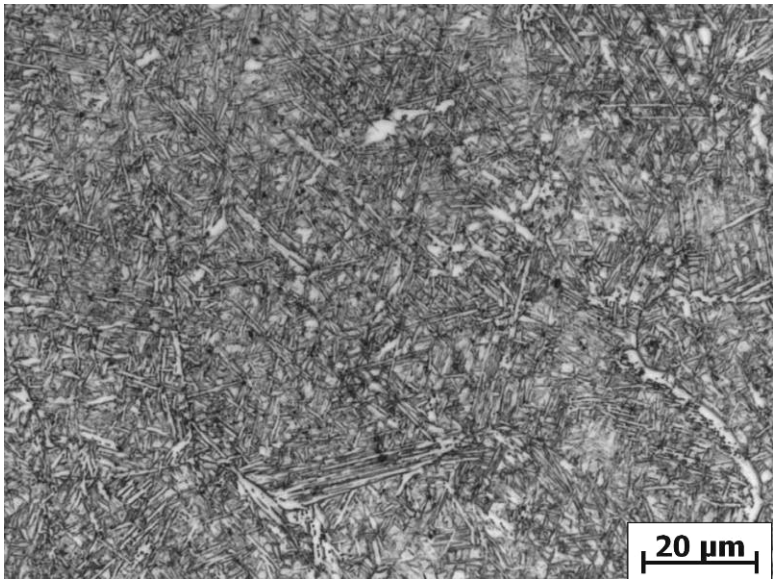

(a) Free cool: $\Delta t_{800\text{-}500}$= 2 s

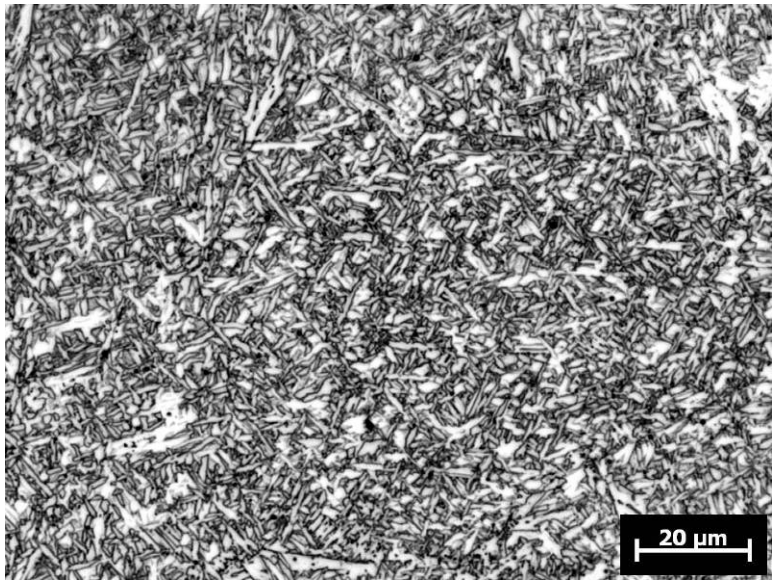

(b) $\Delta t_{800\text{-}500}$= 5 s

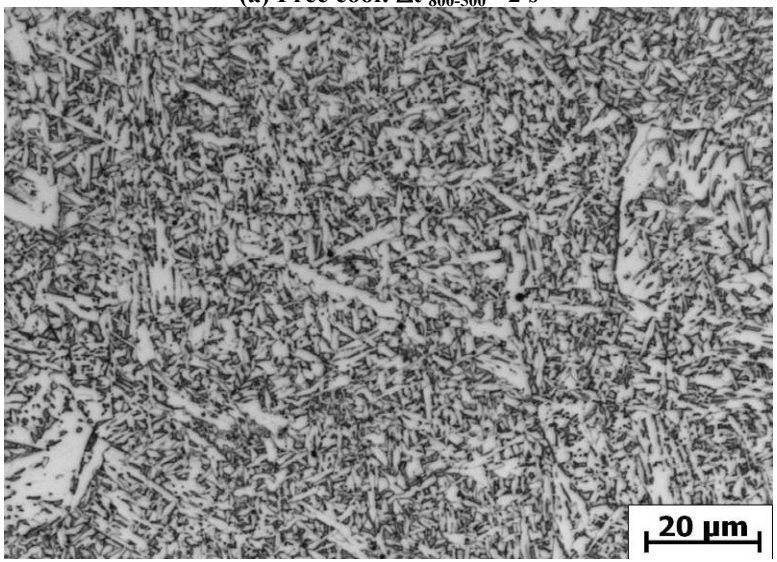

(c) $\Delta t_{800\text{-}500}$= 10 s

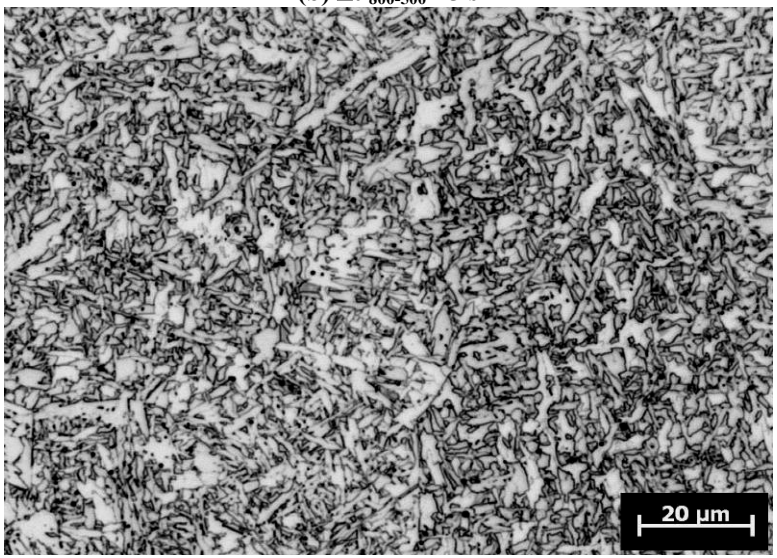

(d) $\Delta t_{800\text{-}500}$= 20 s

Figure 28. WM microstructures of thermally cycled specimens from weld LA 90 as a function of cooling time.

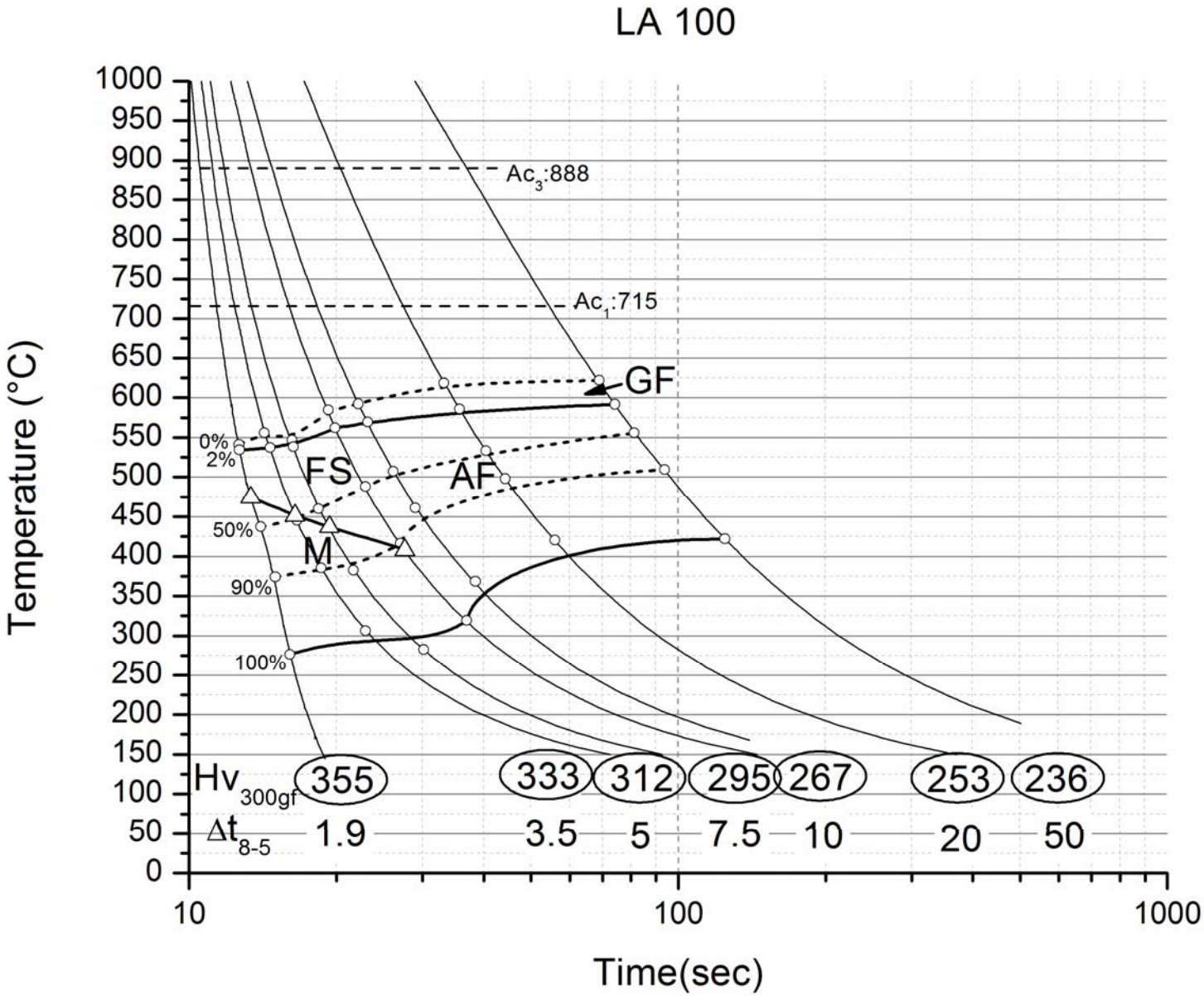

Figure 29. CCT diagram for weld LA 100.

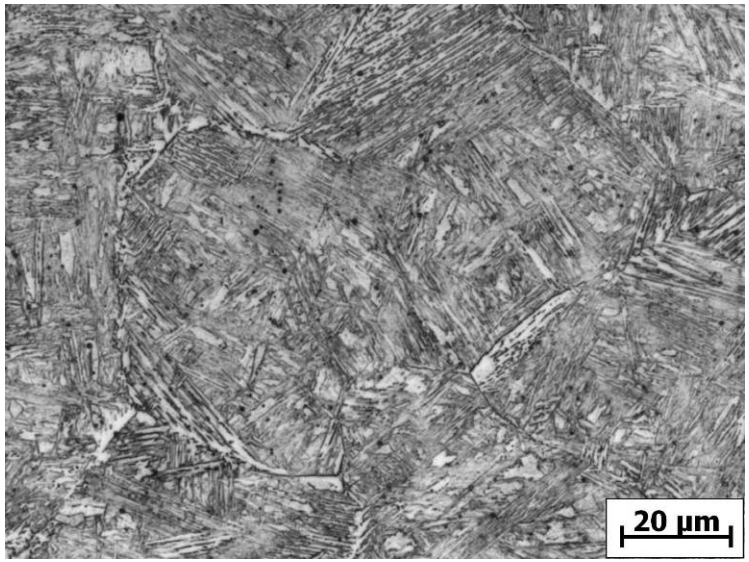

(a) Free cool with $\Delta t_{800\text{-}500}$= 2 s

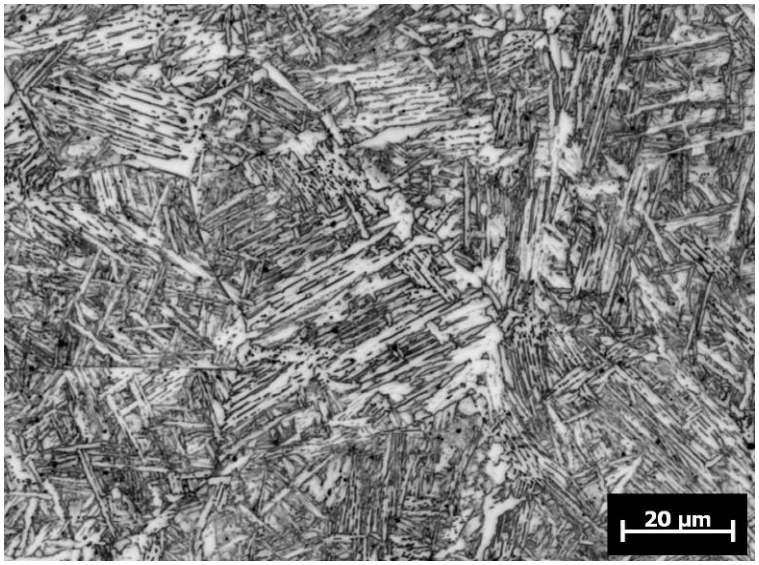

(b) $\Delta t_{800\text{-}500}$= 5 s

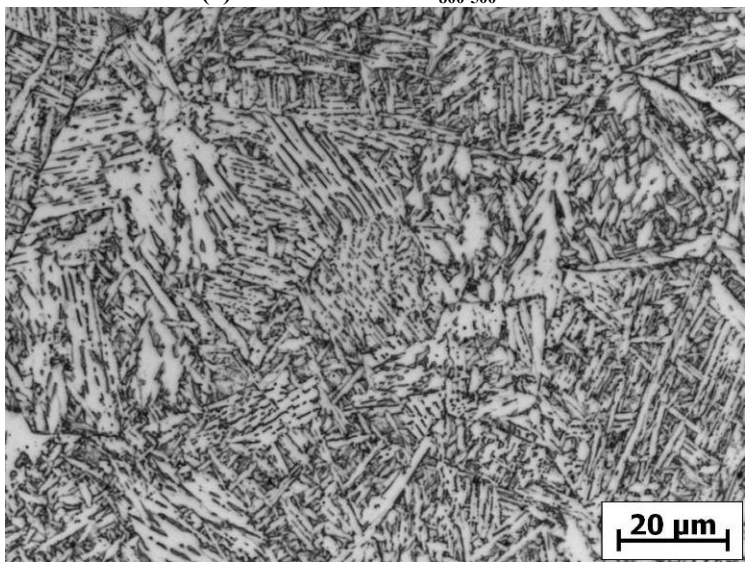

(c) $\Delta t_{800\text{-}500}$= 10 s

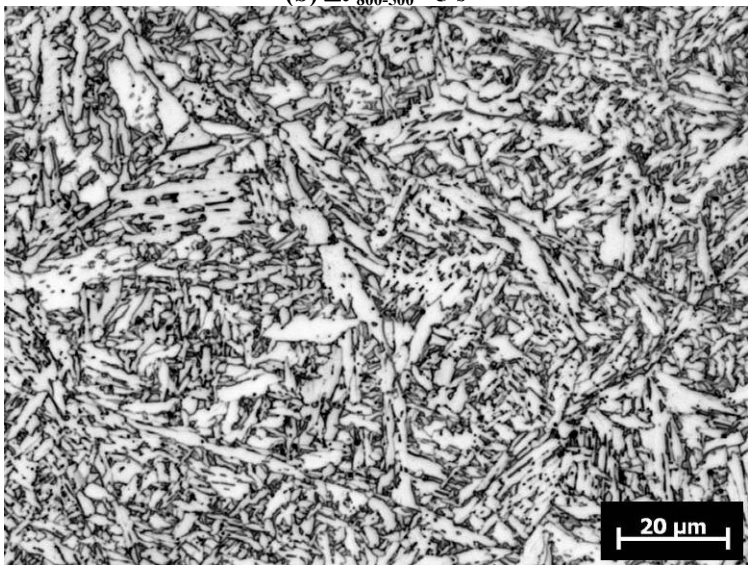

(d) $\Delta t_{800\text{-}500}$= 20 s

Figure 30. WM microstructures of thermally cycled specimens from weld LA 100 as a function of cooling time.

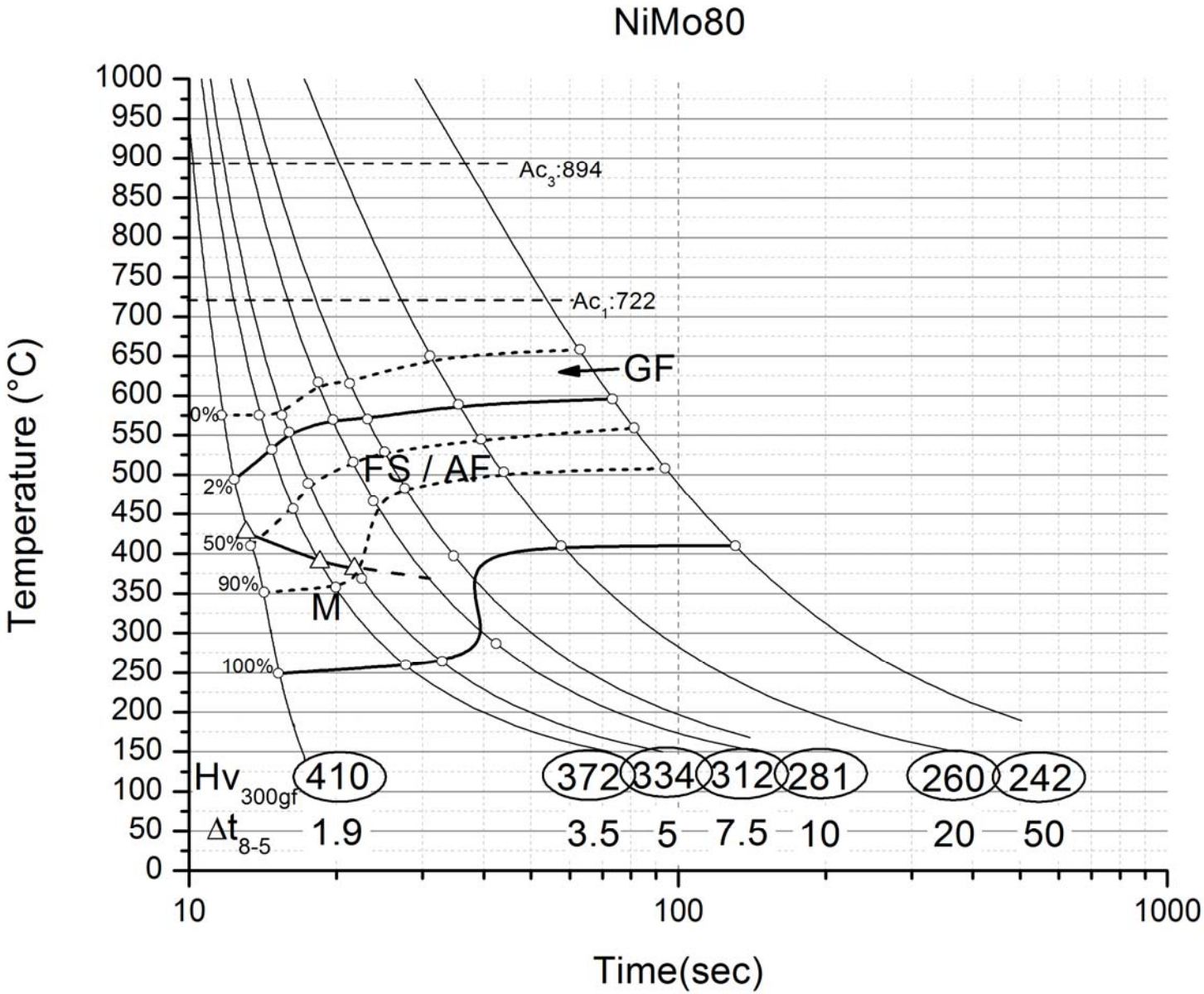

Figure 31. CCT diagram for weld NiMo80.

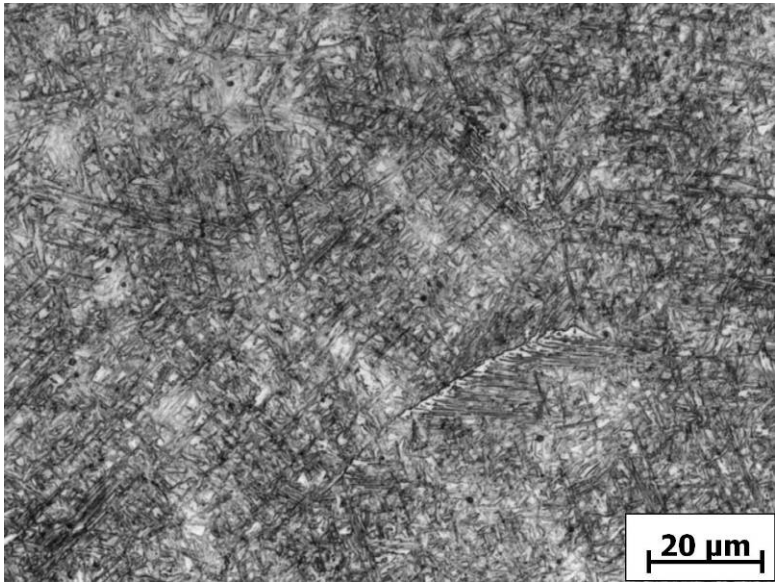

(a) Free cool $\Delta t_{800\text{-}500}$= 2 s

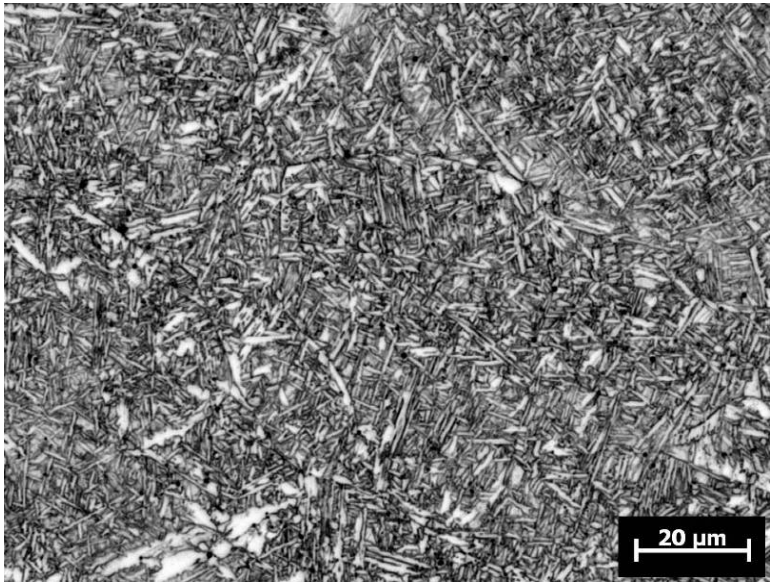

(b) $\Delta t_{800\text{-}500}$= 5 s

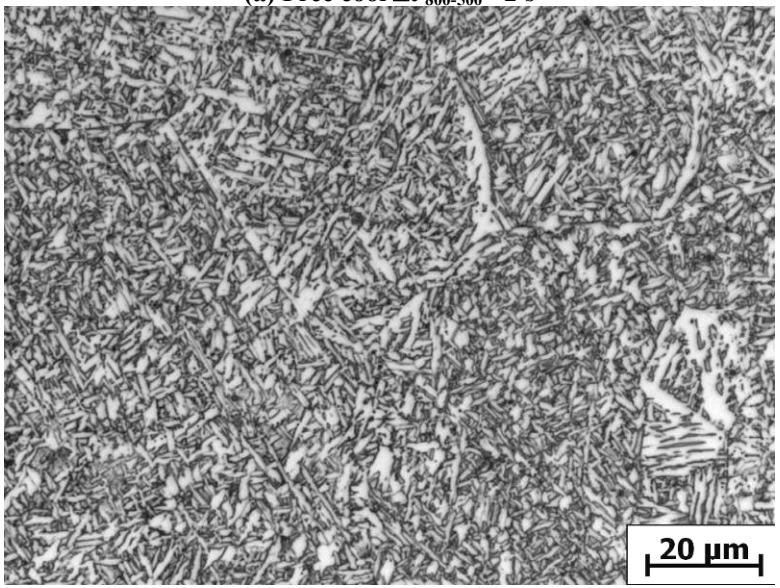

(c) $\Delta t_{800\text{-}500}$= 10 s

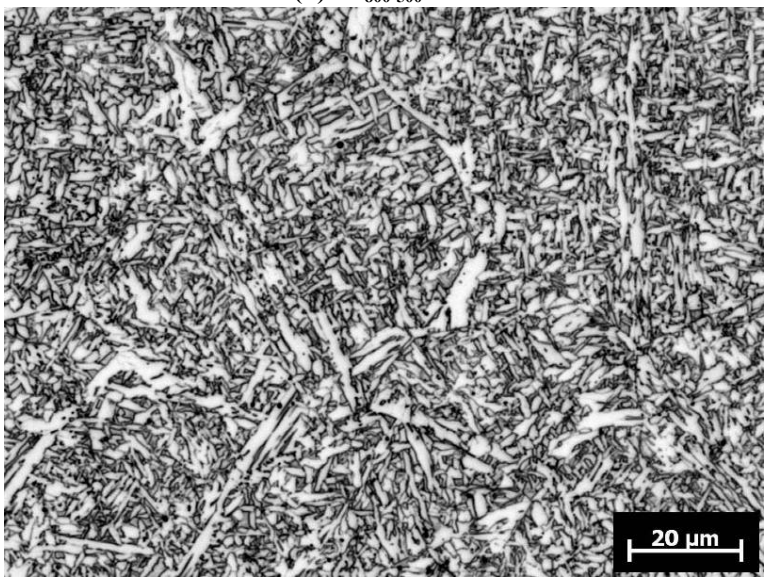

(d) $\Delta t_{800\text{-}500}$= 20 s

Figure 32. WM microstructures of thermally cycled specimens from weld NiMo80 as a function of cooling time.

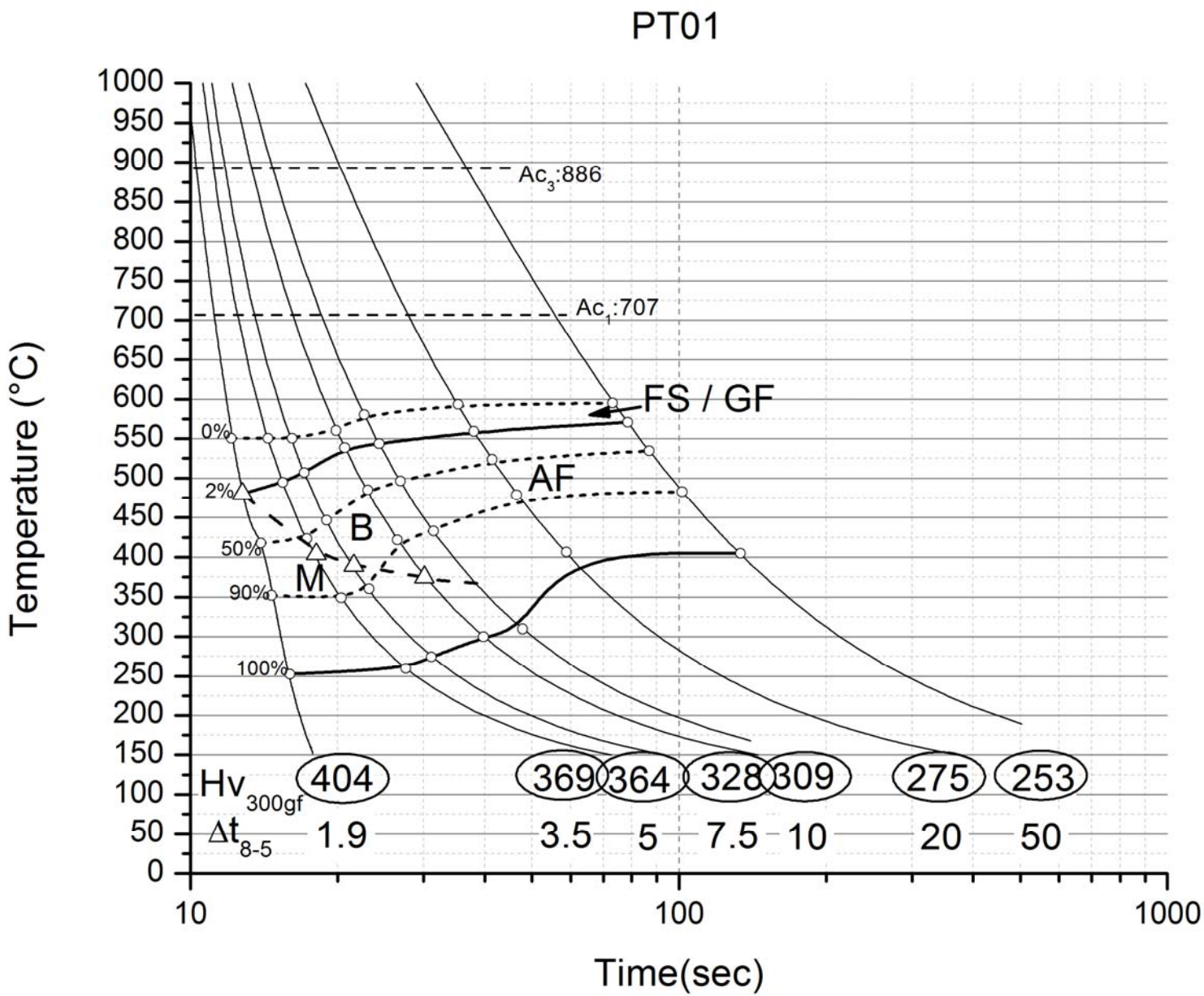

Figure 33. CCT diagram for weld PT-01.

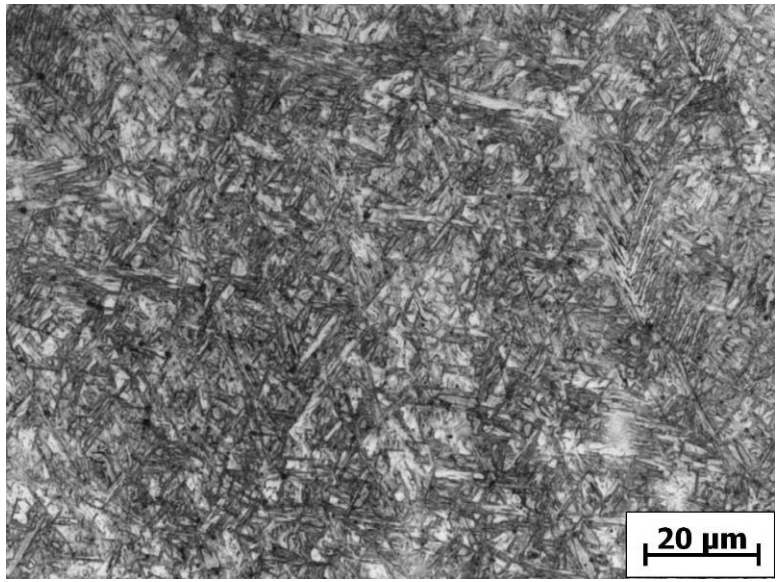

(a) Free cool $\Delta t_{800\text{-}500}$= 2 s

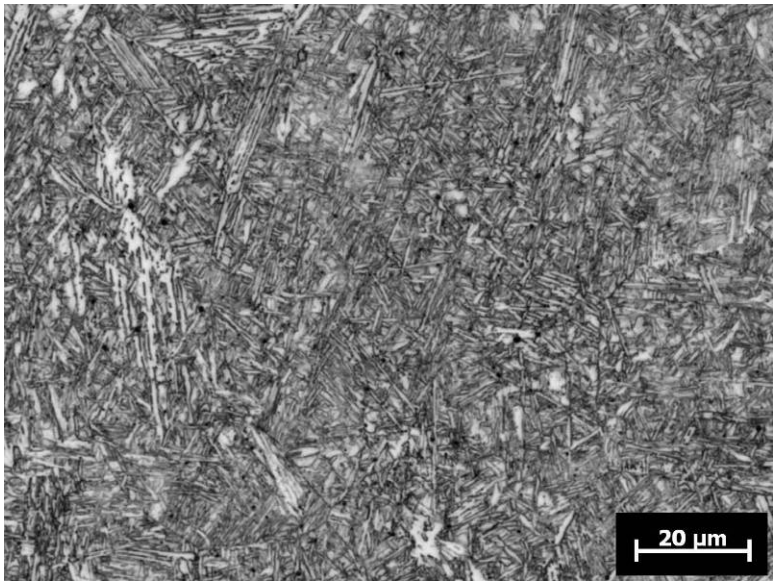

(b) $\Delta t_{800\text{-}500}$= 5 s

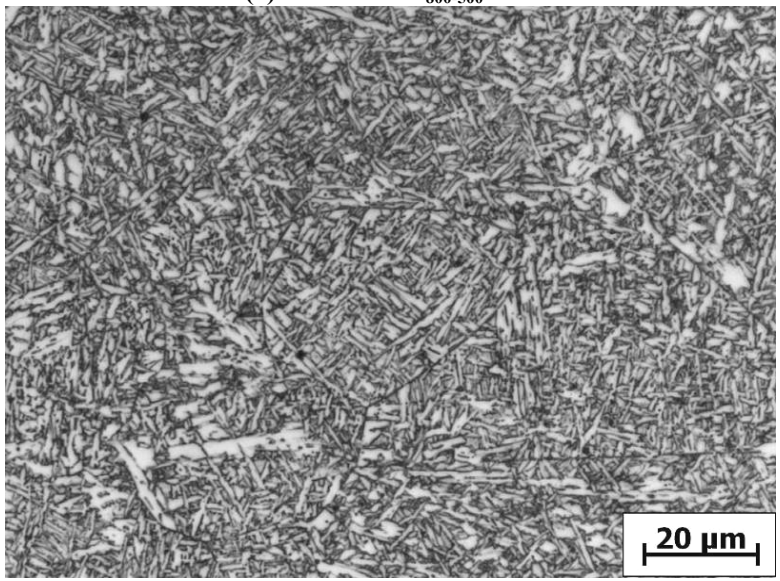

(c) $\Delta t_{800\text{-}500}$= 10 s

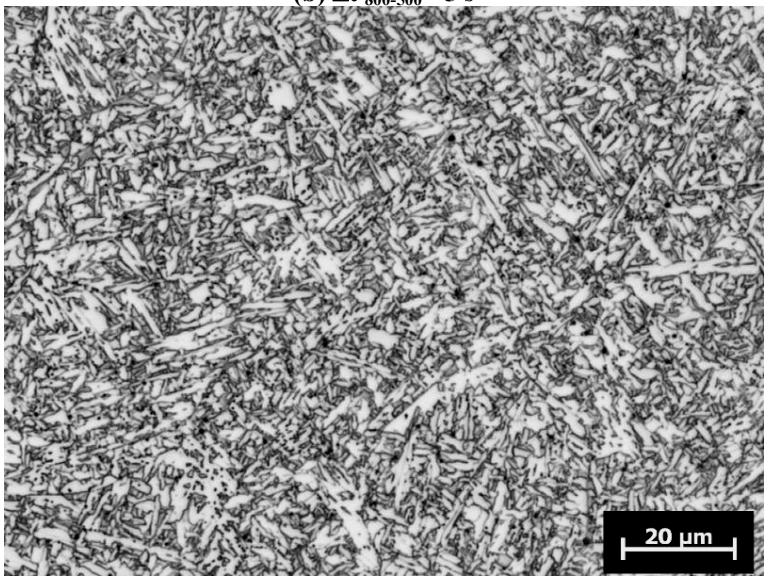

(d) $\Delta t_{800\text{-}500}$= 20 s

Figure 34. WM microstructures of thermally cycled specimens from weld PT-01 as a function of cooling time.

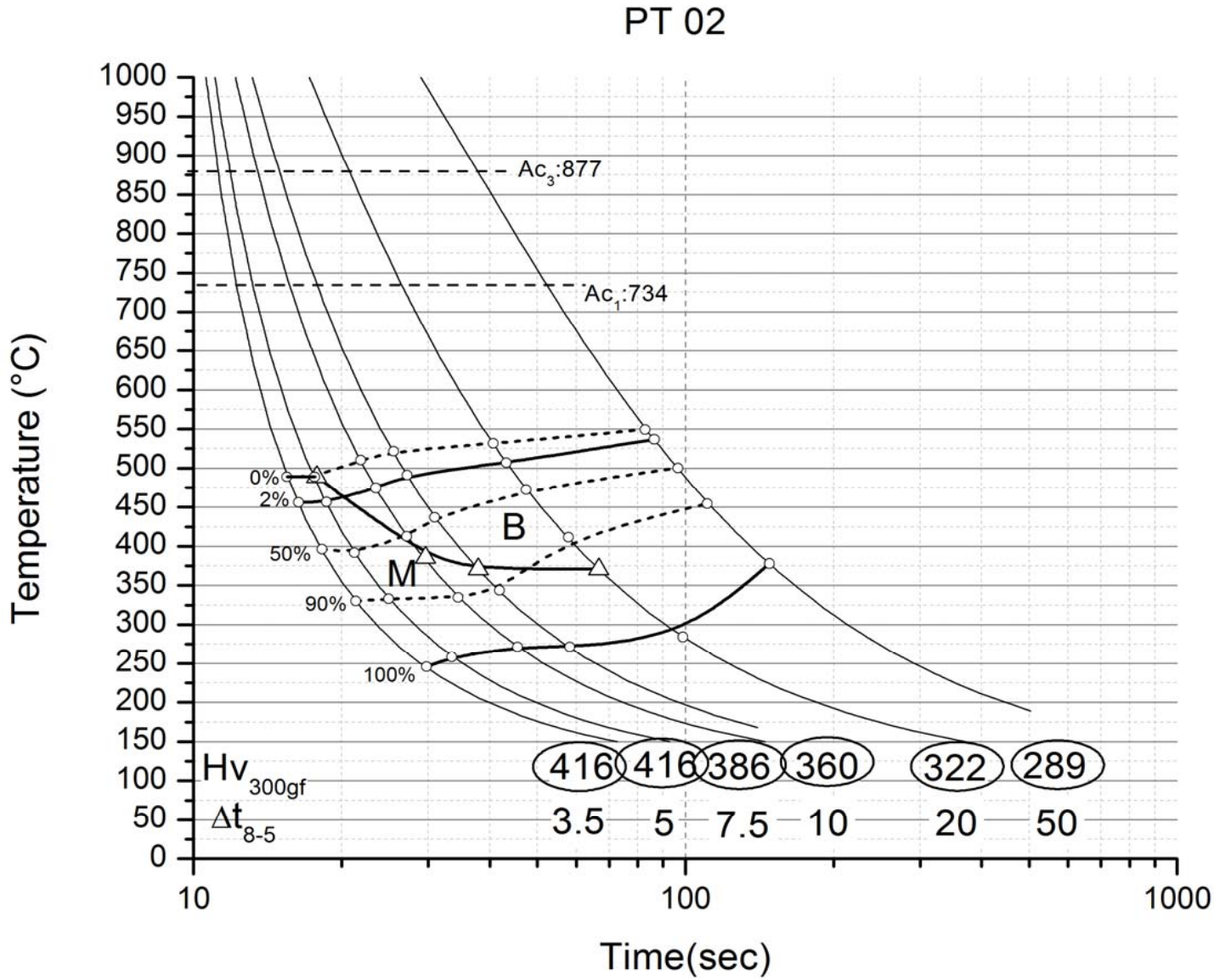

Figure 35. CCT diagram for weld PT-02.

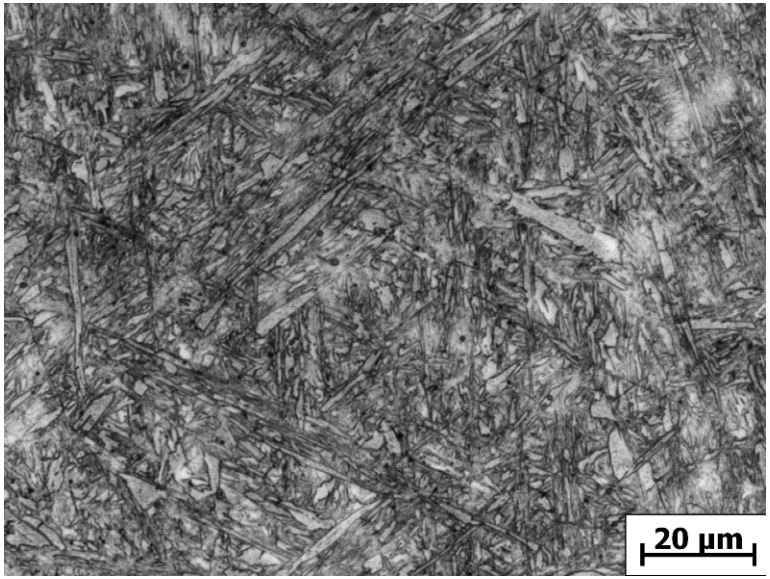

(a) Free cool $\Delta t_{800\text{-}500}$= 2 s

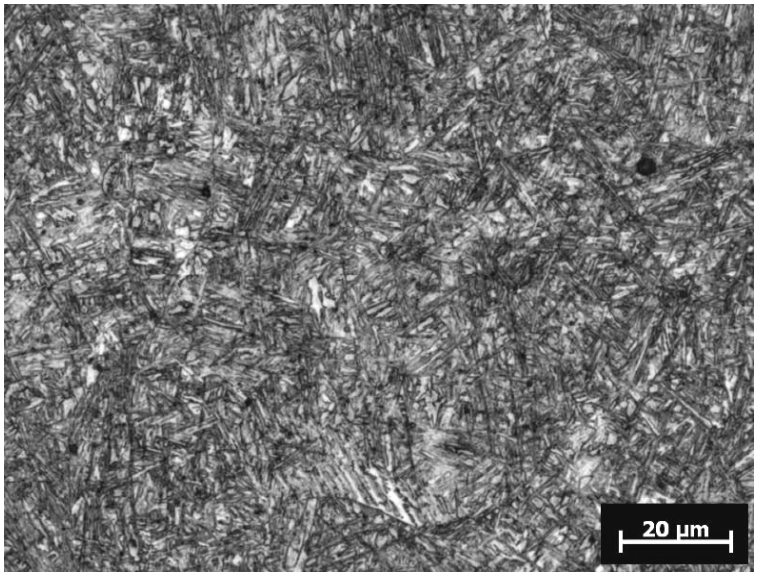

(b) $\Delta t_{800\text{-}500}$= 5 s

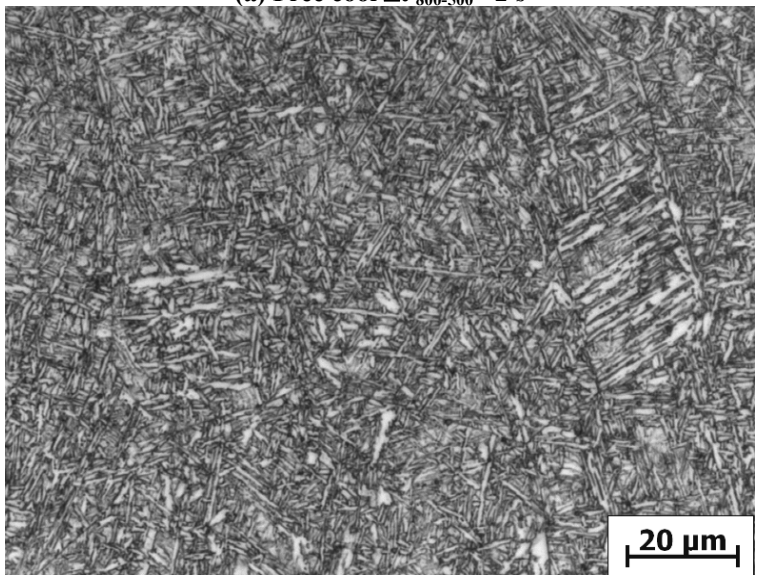

(c) $\Delta t_{800\text{-}500}$= 10 s

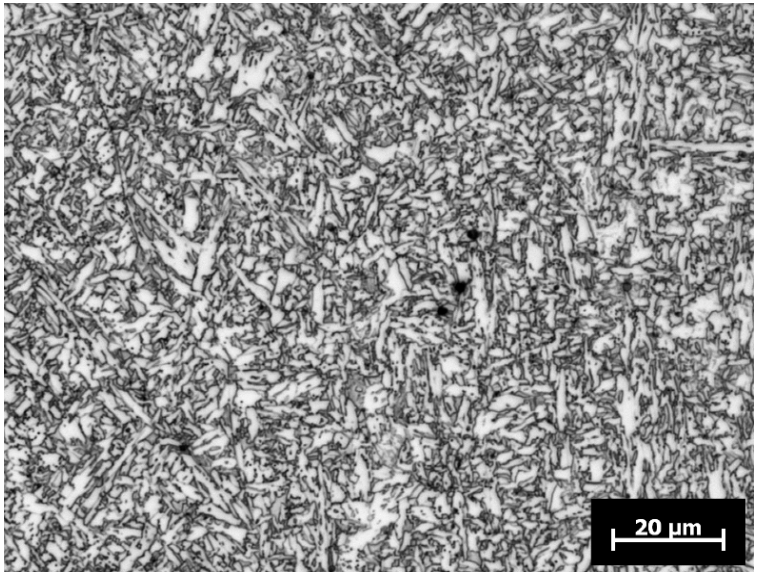

(d) $\Delta t_{800\text{-}500}$= 20 s

Figure 36. WM microstructures of thermally cycled specimens from weld PT-02, as a function of cooling time.

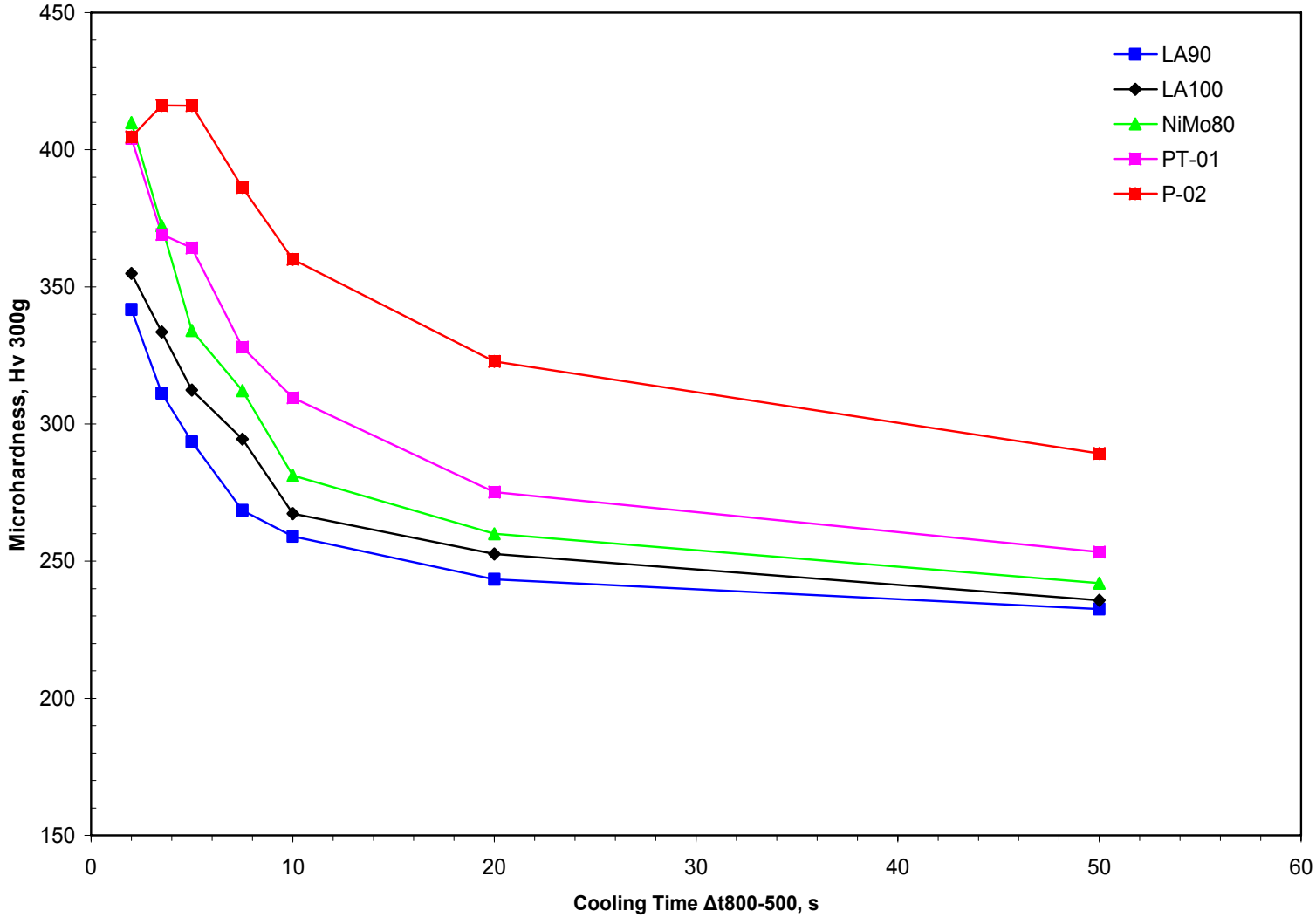

Figure 37. Microhardness of thermally cycled WM specimens as a function of cooling time.

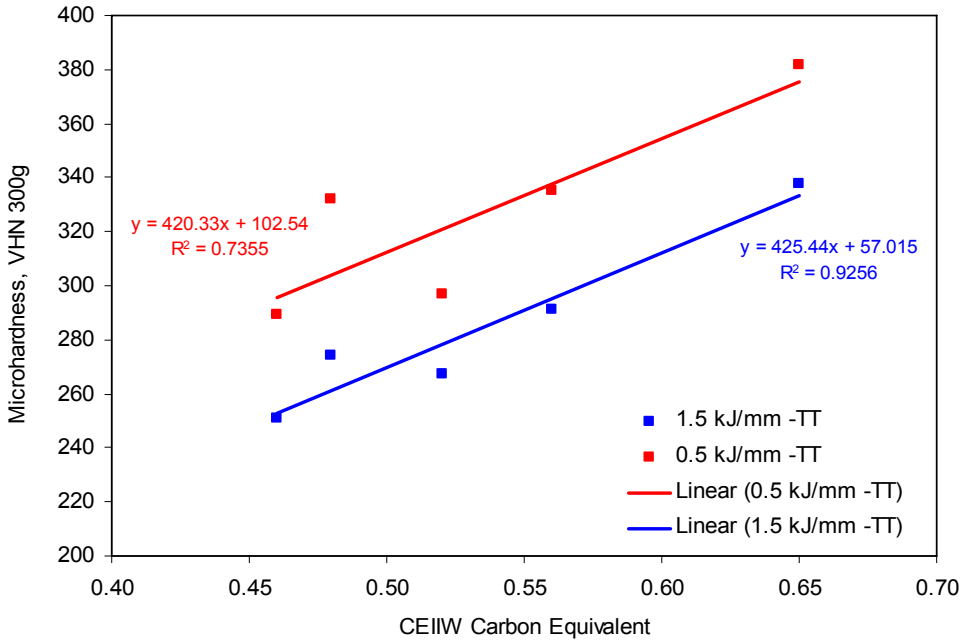

(a)

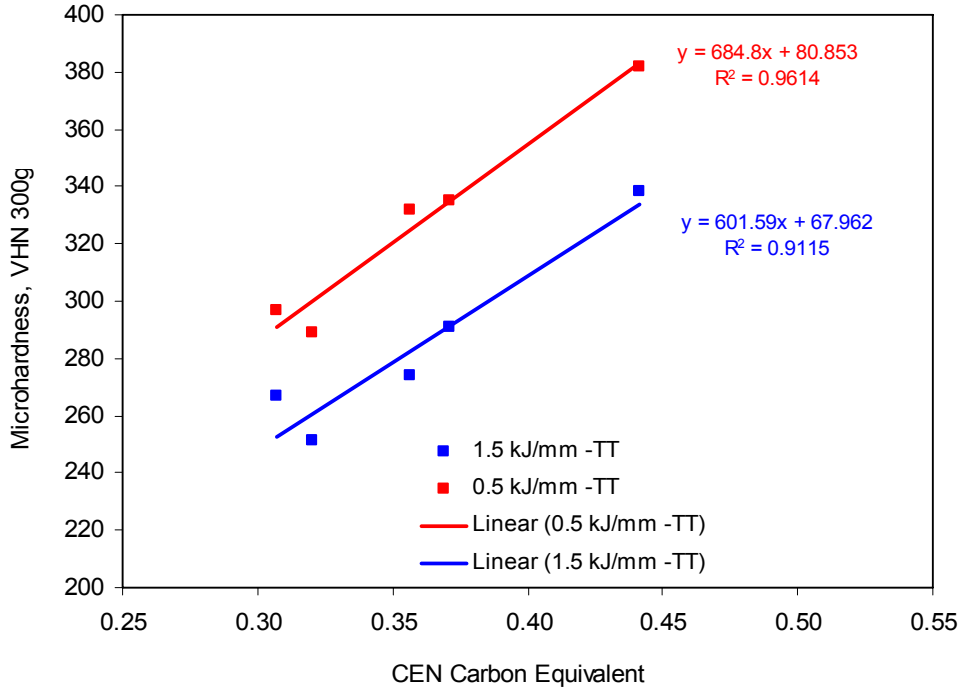

(b)

Figure 38. Correlation between microhardness and carbon equivalent formula (CE_{IIW} and CEN) for WM regions within 1.5 kJ/mm deep-fill pass and underlying 0.5 kJ/mm fill passes. Note microhardness data are based on average of through-thickness weld centerline traverses.

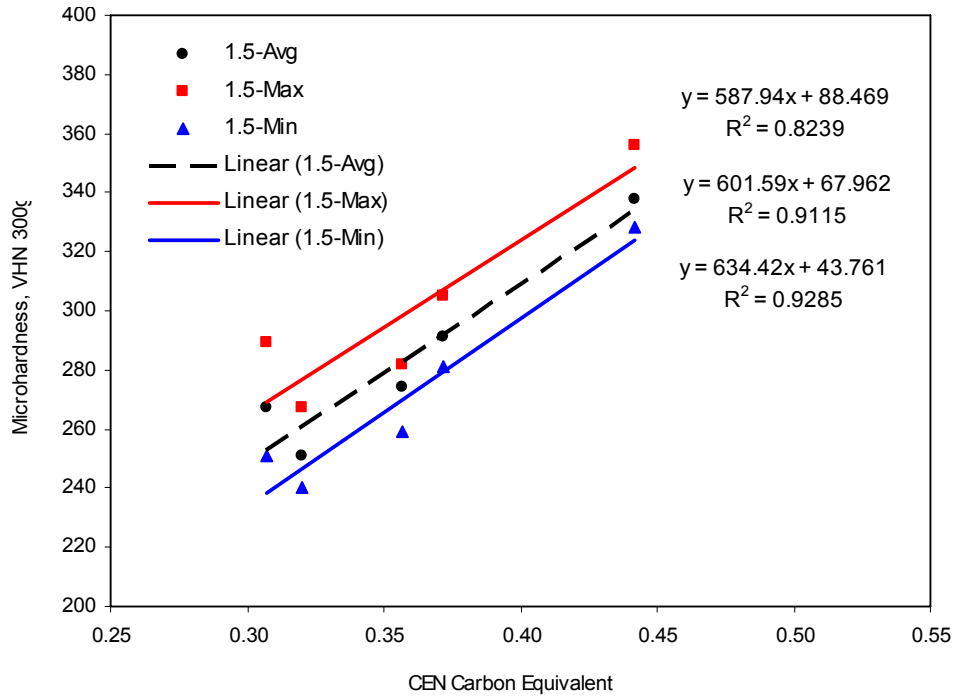

(a)

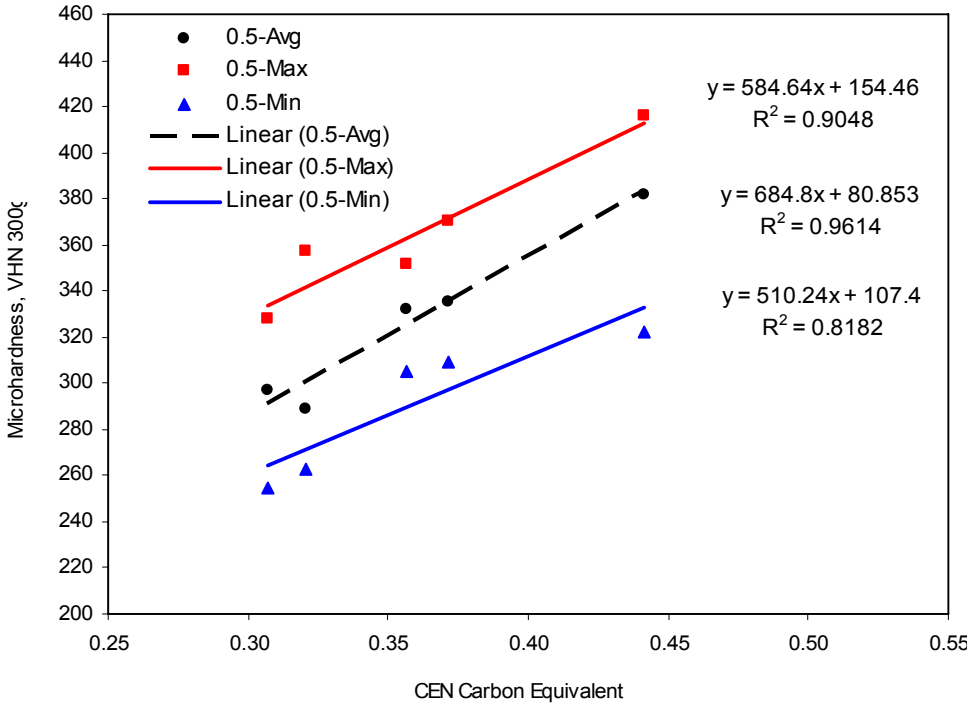

(b)

Figure 39. Correlation between microhardness and carbon equivalent for WM regions within 1.5 kJ/mm deep-fill pass and underlying 0.5 kJ/mm fill passes. Note microhardness data are based on maximum, minimum and average of through-thickness weld centerline traverses.

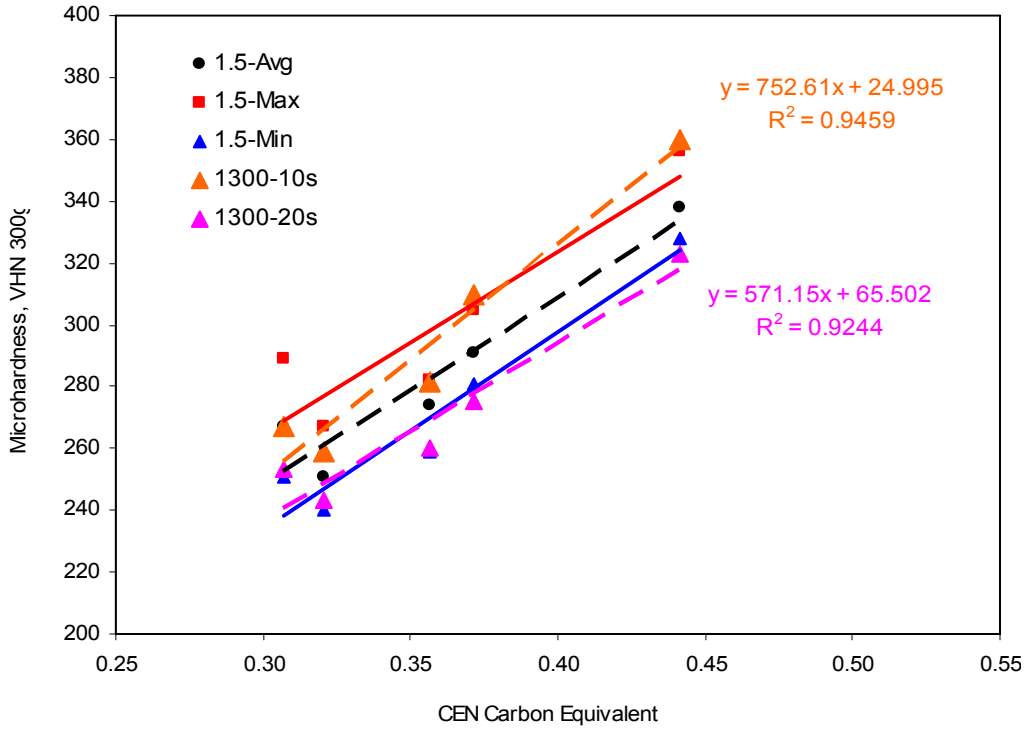

(a)

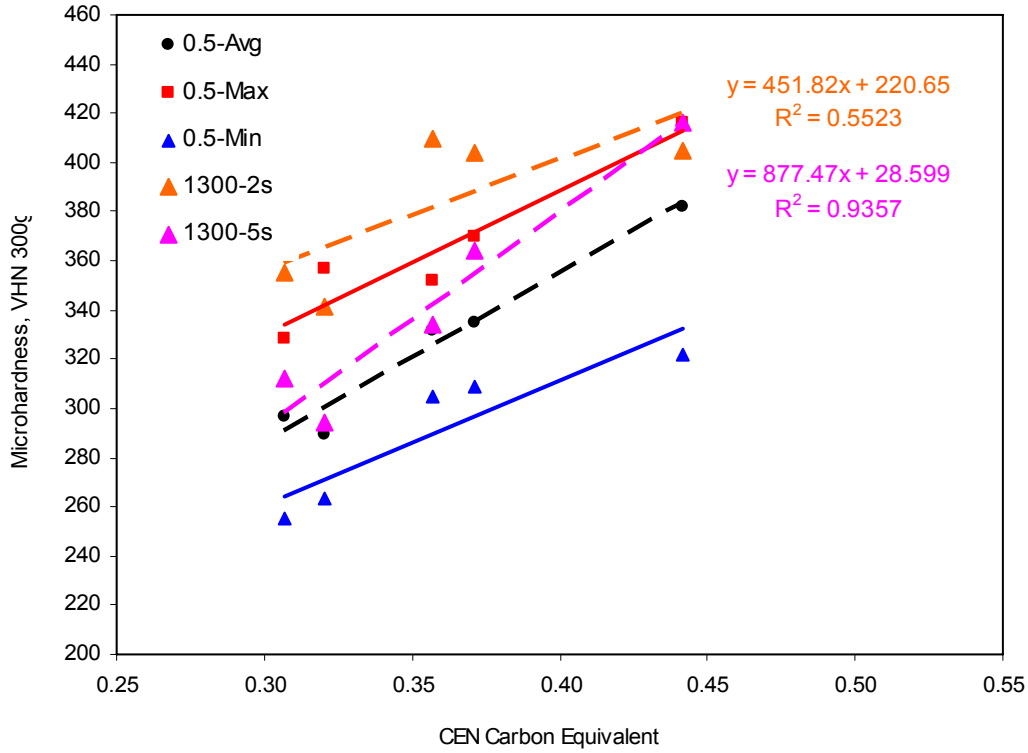

(b)

Figure 40. Correlations between microhardness and carbon equivalent for experimental welds and range of thermally simulated WM with selected cooling times. Note microhardness is based on average of data sets.

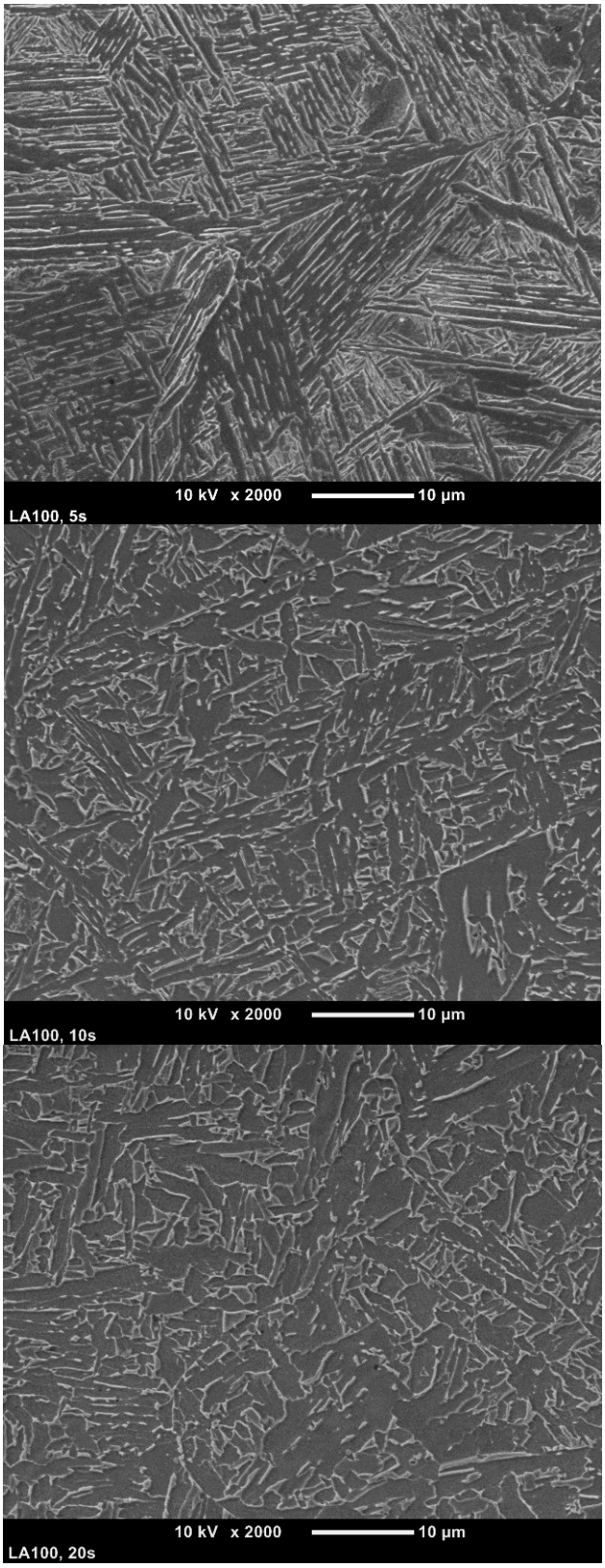

Figure 41. SEM images of thermally cycled LA100 WM for cooling times $\Delta t_{800\text{-}500}$= 5, 10 and 20s.

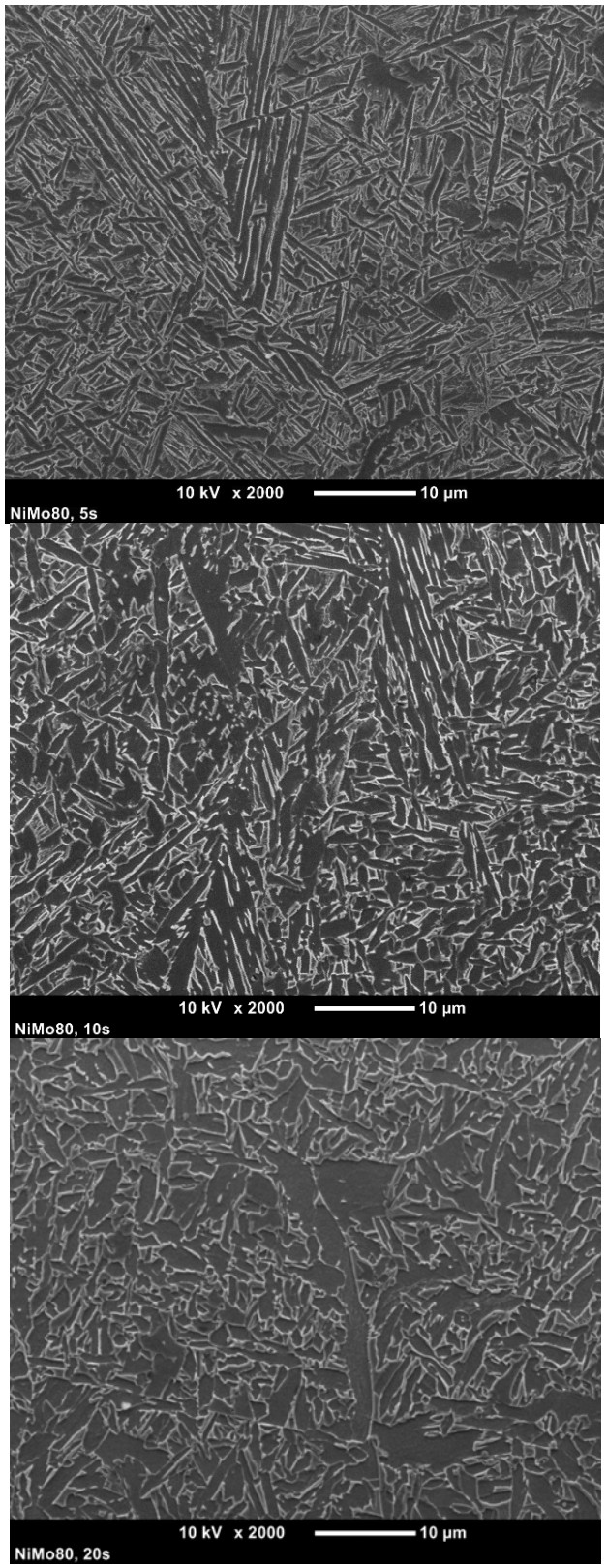

Figure 42. SEM images of thermally cycled NiMo80 for cooling times $\Delta t_{800\text{-}500}$= 5, 10 and 20s.

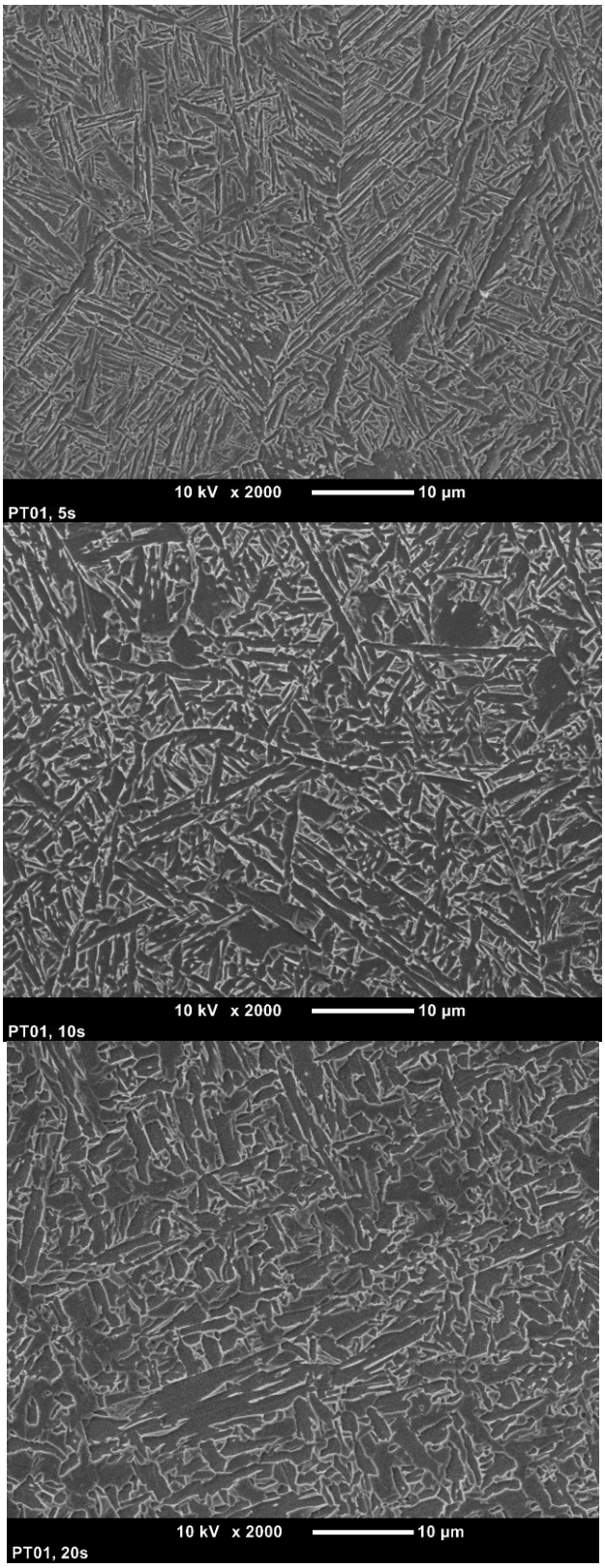

Figure 43. SEM images of thermally cycled PT- 01 for cooling times $\Delta t_{800\text{-}500}$= 5, 10 and 20s.